UNIVERSITÀ DEGLI STUDI DI PALERMO

Dottorato in Scienze Fisiche
Dipartimento di Fisica e Chimica – Emilio Segrè
Settore Astronomia e Astrofisica (FIS/05)

Accretion and ejection in transient black hole binaries: the case of GRS 1716-249

IL DOTTORE
Tiziana Bassi

IL COORDINATORE
Prof. Gioacchino Massimo Palma

IL TUTOR
Dr.ssa Melania Del Santo

IL CO TUTOR
Dr. Julien Malzac

CICLO XXXII
ANNO CONSEGUIMENTO TITOLO - 2020

Université de Toulouse

THÈSE

En vue de l'obtention du

DOCTORAT DE L'UNIVERSITÉ DE TOULOUSE

Délivré par : *l'Université Toulouse 3 Paul Sabatier (UT3 Paul Sabatier)*
Cotutelle internationale *Universitá degli studi di Palermo*

Présentée et soutenue le *19/03/2020* **par :**

Tiziana BASSI

Accrétion et éjection dans les systémes binaires X transitoires á trous noirs: le cas de GRS 1716–249

JURY

Giorgio MATT	Professeur d'Université	Membre du Jury
Sylvain CHATY	Professeur d'Université	Membre du Jury
Peter VON BALLMOOS	Professeur d'Université	Membre du Jury
Gioacchino Massimo PALMA	Professeur d'Université	Membre du Jury
Melania DEL SANTO	Researcher	Directeur
Julien MALZAC	Chargé de Recherche	Co-directeur

École doctorale et spécialité :
SDU2E : Astrophysique, Sciences de l'Espace, Planétologie
Unité de Recherche :
Institut de Recherche en Astrophysique et Planétologie (UMR 5277)
Directeur(s) de Thèse :
Melania DEL SANTO et *Julien MALZAC*
Rapporteurs :
Giorgio MATT et *Sylvain CHATY*

This Thesis work was carried out in:
Istituto di Astrofisica Spaziale e Fisica cosmica - Istituto Nazionale di Astrofisica Palermo (INAF Palermo, Italy);
Institut de Recherche en Astrophysique et Planètologie (IRAP Toulouse, France).

To who makes me smile
To who believes in me even when I can't
To who supports me despite my bad mood
To who gives me courage and helps me to follow my wishes
despite the difficulties
To those who listen to my idiocies and my complaints
To those who share with me a glass of wine
and wonderful unforgettable moments
To those who had shown me the beauty to be part of an international world

Thank you!

Abstract

Black hole transients (BHTs) are among the brightest X-ray sources in the Galaxy. Thanks to their high X-ray flux and short variability time scales they offer a unique opportunity to study the physics of the accretion under extraordinary physical conditions. These sources show episodic outbursts characterised by different X/γ-ray luminosities, spectral shapes and timing properties. The aim of this thesis is the understanding of the geometry, mechanisms and physical processes playing a role in the bright black hole X-ray transient GRS 1716–249.
I present the spectral and timing analysis of X-ray observations performed with the *Neil Gehrels Swift Observatory* on GRS 1716–249 during the 2016-2017 outburst. These data gave me the opportunity to study the evolution of physical parameters and geometry variation of the accreting matter through the spectral transitions during the whole outburst. I found that the accretion disc could have reached the inner stable circular orbit during the hard intermediate state, coherently with the truncated accretion disc scenario in which the disc moves closer to the compact object. Then, the radio monitoring performed during the outburst let me locate the source on the ever more populated radio-quiet branch on the radio/X-ray luminosity plane.
Thereafter, focusing on the soft γ-ray emission of the source, I observed a high energy excess, above 200 keV, in addition to the thermal Comptonisation spectrum. This component could be originate either through inverse Compton of the soft photons by non-thermal electrons in the corona, or from synchrotron emission of energetic electrons in the jet. First, I fitted the broad band X/γ-ray spectrum of GRS 1716–249 with hybrid Comptonisation thermal/non-thermal models: EQPAIR and BELM. Using BELM I obtained an upper limit on the magnetic field intensity in the corona. Finally, I investigated the possible origin of this high energy excess as due to jet emission. To this aim, I computed the Spectral Energy Distribution of GRS 1716–249 with the multi-wavelength observations (from the radio band to γ-rays) performed. I modelled the accretion flow with an irradiated disc plus Comptonisation model and the jet emission with the internal shock emission model (ISHEM). This model assumes that the jet velocity fluctuations are directly driven by the variability of X-ray timing proprieties of the accretion flow. Even though ISHEM reproduces the radio and soft γ-ray data of GRS 1716–249, the results seems to disfavour the jet scenario for the excess above 200 keV, in favour of non-thermal Comptonisation process.

Abstract

I buchi neri transienti (BHT) sono tra le sorgenti con emissione ai raggi X piú luminose della galassia. Grazie all'elevato flusso in banda X e alla loro alta variabilità temporale. queste sorgenti offrono un'opportunitá unica per studiare la fisica dell'accrescimento in straordinareie condizioni fisiche. I BHT mostrano episodici outburst caratterizzati da diverse luminositá in banda X e γ, diverse forme spettrali e proprietá della variabilitá temporale. L'obiettivo di questa tesi é lo studio della geometria, dei meccanismi e dei processi fisici coinvolti nell'emissione del buco nero transiente GRS 1716–249. Di seguito presento l'analisi spettrale e temporale delle osservazioni della GRS 1716–249 ai raggi X effettuate con il satellite *Neil Gehrels Swift Observatory* durante l'outburst verificatosi nel 2016-2017. Questi dati mi hanno permesso di studiare l'evoluzione dei parametri fisici durante tutta la durata dell'outburst e di studiare come varia la geometria della materia in accrescimento attraverso le transizioni spettrali. In particolare, coerentemente con lo scenario del disco di accrescimento troncato in cui il disco si avvicina all'oggetto compatto durante l'evoluzione dell'outburst, ho osservato che il disco di accrescimento della GRS 1716–249 potrebbe aver raggiunto l'ultima orbita stabile mentre la sorgente si trovava nello stato hard intermedio. Grazie al monitoraggio radio effettuato durante l'outburst ho potuto localizzare la sorgente sulla sempre piú popolata correlazione radio/X degli "outliers" (o radio-quieti) nel piano delle luminositá radio/X. Successivamente, mi sono concentrata sull'emissione ai raggi X/γ della sorgente. Questo mi ha permesso di osservare un eccesso nell'emissione alle alte energie, sopra a 200 keV, in aggiunta allo spettro di Comptonizzazione termica, nello spettro della GRS 1716–249. L'origine di questa componente puó essere dovuta a processi di Compton inverso tra i fotoni soft del disco d'accrescimento e una popolazione di elettroni non-termici nella corona, o all'emissione di sincrotrone prodotta dagli elettroni energetici nel getto. Inizialmente ho modellando lo spettro X/γ della sorgente con modelli ibridi di Comptonizzazione termica/non-termica: EQPAIR e BELM. In particolare, utilizzando BELM ho potuto stimare un limite superiore sull'intensitá del campo magnetico nella corona. Infine, ho considerato la possibilitá che l'eccesso di energia alle ate energie sia dovuto all'emissioni del jet. A tale scopo, ho prodotto la distribuzione d'energia spettrale della GRS 1716–249 usando le osservazioni multi-banda (dalla banda radio ai raggi γ) eseguite quando la sorgente era nello stato hard. Il flusso di accrescimento l'ho modellato con un modello di disco irradiato unito ad un modello di Comptonizzazine, mentre l'emissione del getto l'ho modellata con il modello *Internal Schock Emission Model* (ISHEM). Questo modello assume che le fluttuazioni di velocitá del getto siano guidate dalla variabilitá delle proprietá temporali del disco di accrescimento. Sebbene (ISHEM riproduce i dati radio e soft γ della sorgente GRS 1716–249, i risultati favoriscono lo scenario di Comptonizzazione non termica nel flusso di accrescimento rispetto all'emissione di sincrotrone del getto oltre 200 keV.

Résumé

Les transitoires à trou noir (BHT) sont parmi les sources X les plus brillantes de la galaxie. Grace à leur flux X intense et leur variabilité rapide, elles offrent une opportunité unique d'étudier la physique de l'accrétion dans des conditions physiques extrêmes. Ces sources présentent des éruptions épisodiques caractérisées par différents niveaux de luminosité en rayons X et γ , differentes formes spectrales et propriéé de variabilité temporelle. Le but de cette thèse est de mieux comprendre la géométrie, les mécanismes et les processus physiques jouant un role dans la transitoire X à trou noir brillante GRS 1716–249. Je présente l'analyse spectrale et temporelle des observations de GRS 1716–249 en rayons X effectuées avec l'Observatoire Neil Gehrels Swift durant son éruption de 2016-2017. Ces données m'ont permis d'étudier l'évolution des paramètres physique pendant toute la durée de l'éruption ainsi que les changements de géométrie de la matière accrétante durant les transitions spectrales. Je montre que le disque d'accrétion pourrait avoir atteint la dernière orbite circulaire stable pendant l'état dur intermédiaire. Ceci est en accord avec le modèle de disque tronqué dans lequel bord interne du disque se rapproche de l'objet compact. De plus, le suivi de la source en ondes radio, effectué pendant l'éruption, me permet de placer la source sur la branche radio faible de la correlation des luminosités radio et X. Par la suite, je me concentre sur l'émission en rayons γ mous de la source. Un excès à haute énergie est détecté au dessus de 200 keV par rapport au spectre de Comptonization thermique. L'origine de cette composante pourrait être l'émission Compton inverse par des électrons non-thermiques dans la couronne, ou l'émission synchrotron d'electron relativistes dans le jet. Je commence par fitter le spectre large bande X/γ de GRS 1716–249 avec des modèles de Comptonization hybride thermique/non-thermique: EQPAIR et BELM. Les ajustements spectraux avec BELM me donnent une limite supérieure sur l'intensité du champs magnétique dans la couronne. Je considère ensuite la possibilité que l'excès à haute énergie soit d au jet. Dans ce but, j'ai produit une distribution spectrale d'énergie s'étendant de la radio jusqu'au rayons γ. J'ajuste ces données avec un modèle de disque d'accrétion irradié plus Comptonization pour simuler l'émission du flot d'accrétion, et un modèle de shock internes pour l'émission du jet (ISHEM). Ce modèle de jet suppose que les fluctuations de vitesse du jet découlent directement de la variabilité rapide du flot d'accrétion observée en rayons X. Bien que le modèle ISHEM reproduise bien les données radio et γ-mous de GRS 1716–249 , les résultats favorisent le scenario de Comptonization non-thermique dans le flot d'accretion, plutÃt't qu'une émission synchrotron du jet au delà de 200 keV.

Contents

List of Figures

List of Tables

Chapter 1

Introduction

Even though the history of the X-ray astronomy started with the detection of the X-ray emission from the hot corona of the Sun (in 1948), it is only with the discovery of the first X-ray source (Sco X-1, Giacconi et al., 1962) outside our Solar System that the real challenge of the X-ray astronomy started. Since then, the succession of space-based X-ray experiments on board rockets, stratospheric balloons and the variety of instruments on-board satellites with spectral and timing capabilities and large fields of view, have given the opportunity to explore the X-ray Universe.

Black holes and neutron stars are some of the most interesting objects observed because their compact nature and their influence on the surrounding matter. They have been observed both in our Galaxy and in other galaxies, e.g. active galactic nuclei (AGN), X-ray binaries (XRB) and pulsars. In XRB systems hosting a black hole (black hole binary, BHB) of few solar masses, the accretion of material from the companion star leads to appearance of a bright X-ray source. While, the accretion onto supermassive black holes located at the centre of galaxies (SMBH, with masses around $10^{8-9}\,M_{\odot}$) manifests itself in a wide variety of different phenomena, termed AGN.

Studying the radiation produced close to the compact object offers the unique opportunity to probe General Relativity in the strong field regime. Furthermore, despite this huge difference in mass between AGNs and BHBs, since early 80's it was realised that several analogies exist between these two group of systems (White et al., 1984). It was understood that the accretion physic of these extraordinary sources is mostly scale invariant. Due to the non-zero angular momentum of the falling matter, an accretion disc forms around the compact object and significant amount of energy is released due to an efficient mass-energy conversion (see Chapter 2). Studying the emission from UV to X-ray energy bands of these powerful accreting objects provides fundamental information about the physics of the accretion mechanism. In both AGNs and BHBs this emission can be well explained by an optically thick and geometrically thin accretion disc, even though its emission peak, due to the different mass scales of the black hole, is observed at different energies: i.e. in AGNs the peak is observed at UV/optical wavelength, while in BHBs the disc emits mainly in the X-rays.

Close to the black hole, in the central parts of the accretion flow an additional

component arising from a very hot plasma ($T \geq 10^8$ K, the so-called corona) contributes to, and often dominates, the hard X-ray emission of these systems. The physical nature, structure and geometry of the corona are still highly controverted and are the subject of intense investigations.
The radio band emission is due to the ejection of matter through relativistic outflows. The presence of relativistic jets is known to be ubiquitous and tightly connected with the accretion process (see Chapter 3). The big amount of multi-wavelength observation campaigns performed and the comparison between AGNs and BHBs have highlighted the presence of a unified scaling relation which connects these sources. The three-dimensional "fundamental plane of black holes" (Merloni et al., 2003) provided a proof of the existence of a relationship between the black hole mass and the accretion/ejection processes through the X-ray and radio luminosity, respectively. Nevertheless, the inflow/outflow connection, even though it is recognised playing an active and fundamental role in the dynamical and physical structure of these sources, is not completely understood yet.

The BHBs transients (BHTs) are an excellent laboratory to study the physics of the accretion throughout their outburst evolution thanks to their high X-ray flux and the shorter variability time scales (ms up to months) with respect to AGNs. During their outbursts, the mass accretion rate onto the central compact object rises leading to an increase in X-ray emission by several orders of magnitude, before decaying back to the initial value. These events are associated to changes of the X-ray spectral shape which occur on timescales of few days (Zdziarski & Gierliński, 2004; Remillard & McClintock, 2006), and timing properties (variability down to the ms time scale Belloni et al., 2011; Belloni & Motta, 2016). Two main spectral states, namely hard and soft state, are observed. The hard state spectrum is dominated by a hard X-ray component generally interpreted as thermal Comptonization of the soft accretion disc photons by electrons in the hot plasma. While in the soft state the energy spectrum is dominated from the thermal emission of the accretion disc. Nevertheless, there are still a number of unanswered questions about these X-ray accreting systems. A wide debate is open over how the spectral transitions occur, what physical parameters trigger the spectral transition and why some BHTs do not make the transition to the soft states. Furthermore, another key question regards the geometry of the accretion disc, in particular in the hard state. A scenario based on spectral and timing studies suggests that the accretion disc is truncated at large radii from the black hole in the hard states and that the inner part of the accretion flow is then constituted by a hot Comptonising plasma. The truncation disc radius evolves during the outburst extending down to the innermost stable circular orbit in the soft state. However, alternative models (e.g. lamp-post) supported by few observations, suggests a reduction in the spatial extent of the corona, rather than a change in the accretion disc in the hard states (Kara et al., 2019).
In the last decades a further high energy component, above 200 keV, in addition to the thermal Comptonized spectrum of BHBs in hard state has been observed (Del Santo et al., 2008; Bouchet et al., 2009; Droulans et al., 2010). The nature of this component is still debated. It is usually explained as Comptonisation process due to non-thermal electrons (e.g. Poutanen & Coppi, 1998; Coppi, 1999),

while an alternative scenario supported by polarisation measurements invokes synchrotron emission produced in the jet as possible origin (Laurent et al., 2011; Jourdain et al., 2012; Rodriguez et al., 2015).
Another largely investigated topic on the physics of BHTs concerns the connection between the accretion flow and the ejection of matter. The simultaneous observations performed in radio and X-ray bands of these sources demonstrated the existence of a non-linear radio/X-ray flux correlation ($L_{radio} \propto L_X^a$) with an index $a \simeq 0.6 - 0.7$ (Corbel et al., 2000; Gallo et al., 2003). This correlation first appeared to be universal, until it was realised that some sources follow a steeper correlation ($a \sim 1.4$, Coriat et al., 2011). This induced questions about the origin of these two different correlations. These two correlations are intensively investigated in order to understand if they are due to different properties of the accretion and/or ejection or to geometric effects (e.g. the inclination of the jets).
Even though jets have been known for decades, many aspects have not been completely understood yet. For instance: how they are formed and accelerated to mildly-relativistic or relativistic velocities, how they interact with the interstellar medium, how much energy they carry and how it is distributed, how the magnetic field contributes to accelerate and collimate the outflows and how the outflow evolve during the spectral transitions.

The subject of this thesis is the spectral study of a bright X-ray binary system containing a black hole. The main aim is the understanding of the geometry, mechanisms and physical processes playing a role in black hole binaries. In particular with my research I propose to address the following questions:

- How do the accretion disc evolve over the outburst?
- When, during an outburst, does the inner radius of the accretion disc reach the last stable circular orbit?
- What are the parameters triggering or inhibiting the spectral transition to the soft state?
- What is the origin of the two correlations observed in the radio/X-ray luminosity plane?
- What is the origin of the soft γ-ray emission observed in bright hard states?

The source that I studied is the bright black hole transient GRS 1716–249 (also known as GRO J1719–24, Nova Oph 1993). This object was discovered in 1993 September with the *CGRO*/BATSE and *Granat*/SIGMA telescopes (Harmon et al., 1993; Ballet et al., 1993).
The optical counterpart was identified with the spectral type K (or possibly later) star V2293 Oph and a distance of 2.4 ± 0.4 kpc was derived (della Valle et al., 1994). Masetti et al. (1996) estimated a lower limit for the compact object mass of $4.9\,M_\odot$ (confirming the BH nature), an evolved companion star mass of $1.6\,M_\odot$ and an orbital period of 14.7 hr. In 1993 October, the source was also observed in

radio by the Very Large Array (VLA), showing a flat spectrum (della Valle et al., 1993, 1994) interpreted as partially self-absorbed synchrotron emission from electrons ejected from the system.
The source was detected again in outburst on 2016 December 18 by *MAXI* (Monitor of All-sky X-ray Image) after more than twenty years in quiescence (Negoro et al., 2016; Masumitsu et al., 2016). It was intensively monitored during the whole 2016-2017 outburst offering the possibility to investigate the physics of the accretion and ejection during the spectral evolution of the source outburst. In particular, the X-ray spectral analysis of GRS 1716–249 has offered a unique opportunity to constrain physical parameters of the hot accretion flow and to observe how the geometry of the accretion disc evolves through the spectral transitions. Furthermore, adopting a multi-wavelength observational approach combined with the modeling of the radiative processes, gave me the extraordinary possibility to investigate the origin of the high energy emission observed above 200 keV when the source was in the hard state.

1.1 Outline of the thesis

This thesis is divided in the following chapters: the first three chapters are mainly focused on the a general description of the X-ray binaries, with a particular attention to the phenomenology of the black hole transients (**Chapter 1**), the different components of the interacting matter: i.e. the accretion flow (**Chapter 2**) and the outflows (**Chapter 3**), in addition to the main emission processes involved in the different spectral states.
Chapter 4 is an overview on the instruments at different wavelengths used to observe the 2016-2017 outburst of GRS 1716–249. Moreover, in this chapter I will introduce the basic concepts of the X/γ-ray data analysis methods adopted. In **Chapter 5** I show the spectral and timing analysis of X-ray observations performed on that source during the 2016-2017 outburst, and on the physical interpretation of the results. Then, focusing on the X/γ-ray emission of GRS 1716–249, I detected the presence of a spectral component which is in excess to the thermal Comptonisation spectrum. In **Chapter 6** I describe the methods adopted to investigate the origin of this high energy component. This component could originate either by inverse Compton of the soft disc photons from non-thermal electrons in the Corona, or the from synchrotron emission of energetic leptons in the jet. These two possibilities are discussed and tested using different spectral models.

Introduction

Bien que la première détection de l'émission X de la couronne solaire date de 1948, ce n'est qu'avec la découverte de la première source X localisée hors de notre Système Solaire (Sco X-1, Giacconi et al., 1962) que l'astronomie X démarra réellement. Depuis, une succession d'instruments embarqués a bord de fusées, de ballons stratosphériques et de satellites avec des capacités spectrales et temporelles sans précédentes ainsi que de grands champs de vue, ont permis d'explorer l'Univers en rayons X.
Les trous noirs et les étoiles à neutrons sont parmi les objets les plus intéressants que l'on puisse observer. à cause de le leur nature compacte et de leur influence sur la matière environnante. Ils ont étés observés aussi bien dans notre Galaxie que dans d'autres galaxies, e.g. sous forme de pulsars, dans des systèmes binaires X (XRB), ou dans les Noyaux de Galaxies Actives (AGN). Dans les XRB contenant un trou noir de quelques masses solaires (ou binaire à trou noir (BHB)), l'accrétion de la matière de l'étoile compagne conduit à la formation d'une source X brillante. L'accrétion sur les trous noirs super-massifs situés au centre des galaxies (SMBH, ayant des masses de l'ordre de $10^{8-9}\,M_\odot$) se manifeste selon une gamme variée de phénomènes appelés AGN.
L'étude du rayonnement produit près de l'objet compact offre une opportunité unique de tester la relativité générale en champs fort. De plus, malgré cette énorme différence de masse entre AGN et BHBs, depuis le début des années 80, de nombreuses analogies on été observées entres ces deux classes de trous noirs (White et al., 1984). Il a été démontré que la physique de l'accrétion, dans ces sources extraordinaires, est essentiellement invariante d'échelle.
Du fait du moment angulaire non-nul de la matière accrétée, un disque d'accrétion se forme autour de l'objet compact et des quantités importantes d'énergie sont dissipées grâce à une conversion masse énergie efficace (voir Chapitre 2). L'étude des émissions dans les bandes allant de l'UV aux X de ces sources puissantes, fourni des informations fondamentales sur les mécanismes d'accrétion. Dans les AGN et XRB, cette émission peut être expliquée par un disque d'accrétion optiquement épais et géométriquement mince, même si le pic de l'émission est observé à des énergies différentes du fait des différentes masses de trous noirs: dans les AGN le pic est observé aux longueur d'ondes UV/optique, alors que dans les BHB le disque produit surtout des rayons X.
Près du trou noir, dans les parties centrales du flot d'accrétion, une composante supplémentaire provenant d'un plasma très chaud ($T \geq 10^8\,K$, connu sous le nom de 'couronne') contribue et même domine parfois l'émission X-dure de ces systèmes. La nature physique, la structure et la géométrie de la couronne sont encore

le sujet de controverses de haute volée et font l'objet d'intenses recherches.
L'émission radio est causée par l'éjection de matière sous forme de jets relativistes. Ces jets relativistes semblent omniprésents et intimement liés au processus d'accrétion (voir Chapitre 3). Le grand nombre de campagnes d'observation multi-longueurs d'ondes ainsi que les comparaisons entre AGN et BHB on souligné la présence d'une relation d'échelle unifiée qui connecte ces sources. Le "plan fondamental des trous noir" (Merloni et al., 2003) fournit une preuve de l'existence d'une relation entre la masse du trou noir et les processus d'accrétion/éjection à travers les luminosité X et radio respectivement. Cependant la connexion accrétion/éjection n'est pas encore comprise, alors que son rôle actif et fondamental dans la structure physique et la dynamique de ces sources est clairement reconnu.

Les BHB transitoires (BHT) sont un excellent laboratoire pour étudier la physique de l'accrétion en suivant le cours de leur évolution pendant leurs éruptions. Ceci est facilité par leur flux X relativement fort et les échelles de temps de variabilité relativement brèves (de quelques milli-secondes à quelques mois) par rapport aux AGN. Pendant leurs éruptions, le taux d'accrétion de masse sur l'objet central augmente conduisant à une augmentation de plusieurs ordres de grandeur de l'émission X, avant de retourner à sa valeur initiale. Ces évènements éruptifs sont associées à des variations , sur des échelles de temps de quelques jours, du spectre X (Zdziarski & Gierliński, 2004; Remillard & McClintock, 2006), ainsi des propriétés de variabilité temporelle rapide (Belloni et al., 2011; Belloni & Motta, 2016, jusqu'à la milli-seconde).
On distingue deux états spectraux principaux: l'état dur et l'état mou. Le spectre dans l'état dur est dominé par une composantes en rayons X-durs généralement interprétées comme de la comptonization thermique de photons mous émis par le disque par les électrons d'un plasma chaud. Dans l'état mou le spectre est dominé par l'émission thermique du disque d'accrétion. Cependant, il y a toujours un certains nombre de questions sans réponses au sujet de ces systèmes accrétants. Le débat est ouvert sur la façon dont ces transitions spectrales se produisent, les paramètres physiques déclencheurs de la transitions, et pourquoi certaines BHT ne montrent pas de transitions vers les états mous.
Une autre question clef concerne la géométrie du flot d'accrétion, dans l'état dur en particulier. Un scénario basé sur des études spectrales et temporelles suggère que dans les états durs, le disque d'accrétion est tronqué à grande distance du trou noir et les parties internes du flot d'accrétion sont alors constituées d'un plasma de comptonization chaud. Le rayon de troncation du disque change pendant l'éruption et diminue jusqu'à atteindre la dernière orbite stable dans l'état mou. Cependant, des modèles alternatifs (comme le modèle du 'lampadaire') suggèrent une réduction de l'extension de la couronne plutôt que des changements dans le disque d'accrétion, certaines observations favorisent de tels modèles (Kara et al., 2019).

Des observations en rayons X-durs au delà de 200 keV, on montré la présence d'une composante spectrale supplémentaire à haute énergie, qui se rajoute à l'emission thermique du disque et au spectre de Comptonization thermique (Del

Santo et al., 2008; Bouchet et al., 2009; Droulans et al., 2010). La nature de cette composante est débattue. Elle est habituellement attribuée à de l'émission inverse Compton par une population d'électrons non-thermique présents dans la couronne (e.g. Poutanen & Coppi, 1998; Coppi, 1999), un scénario alternatif suggéré par des mesures de polarisation invoque au contraire une émission synchrotron produite dans le jet (Laurent et al., 2011; Jourdain et al., 2012; Rodriguez et al., 2015).
La connexion entre le flot d'accrétion et l'éjection de matière constitue un autre thème de recherche important. Les observations simultanées en radio et rayons X ont démontré l'existence d'une corrélation entre les signatures d'accrétion et d'éjection. Les observations simultanées en rayons X et en radio ont démontré l'existence d'une correlation non-linéaire entre les flux X et radio ($L_{radio} \propto L_X^a$) dont l'indice $a \simeq 0.6-0.7$ (Corbel et al., 2000; Gallo et al., 2003). Cette correlation apparu tout d'abord universelle, jusqu'à ce que l'on se rende compte que certaines sources suivent une corrélation radio/X ayant un indice plus pentu ($a \sim 1.4$, Coriat et al., 2011). Ceci souleva un certain nombre de questions sur l'origine de ces deux corrélation différentes. Elles sont toujours fortement étudiées afin de comprendre si elles sont dues à des propriétés de l'accrétion et/ou de l'éjection différentes dans les sources suivant l'une ou l'autre des deux corrélations, ou bien si elle sont simplement la conséquence d'effets géométriques comme l'inclinaison de l'angle la ligne de visée par rapport au système.
Bien que les jets soient connus depuis des décennies, nombre de leurs aspects ne sont toujours pas tout à fait compris: par exemple la façon dont ils sont formés et accélérés à des vitesses relativistes, leur interaction possible avec le milieu interstellaire, la quantité d'énergie qu'ils emportent, le role des champs magnétiques dans la formation et la collimation des jets, ainsi que leur évolution pendant les transitions d'états spectraux.

Le sujet de cette thèse est l'étude spectrale d'une binaire X brillante contenant un trou noir. L'objectif principal est de comprendre la géométrie ainsi que les mécanismes physiques jouant un rôle dans les binaires à trou noir. En particulier ma recherche s'intéresse aux questions suivantes:

- Comment le disque d'accrétion évolue-t-il pendant les éruptions?
- Quand, durant une éruption, le bord interne du disque d'accrétion atteint-il la dernière orbite circulaire stable?
- Quels sont les paramètres permettant ou empêchant la transition vers l'état mou?
- Quelle est l'origine des deux corrélations observées dans le plan des luminosités X et radio?
- Quelle est l'origine de l'émission en rayon gamma mous observée dans les états dur brillants?

La source que j'ai étudiée est la transitoire à trou noir brillante GRS 1716–249 (connue aussi sous le nom de GRO J1719–24, Nova Oph 1993). Cette

source fut découverte en Septembre 1993 grâce aux télescopes *CGRO*/BATSE et *Granat*/SIGMA (Harmon et al., 1993; Ballet et al., 1993).
La contrepartie optique fut identifiée avec l'étoile V2293 Oph de type spectral K (ou possiblement plus tardif) à une distance de 2.4 ± 0.4 kpc (della Valle et al., 1994). Masetti et al. (1996) estimèrent une limite basse pour la masse de l'objet compact de de 4.9 $M_\odot$ (ce qui confirme la présence d'un trou noir), un étoile compagne évoluée de masse 1.6 $M_\odot$ et une période orbitale de de 14.7 hr. En octobre 1993, la source fut aussi observée en radio avec le Very Large Array (VLA), montrant un spectre plat (della Valle et al., 1993, 1994) interprété comme de l'émission synchrotron auto-absorbée d'électrons énergétiques accélérés dans un jet.
La source fut détectée à nouveau en éruption le 18 Décembre 2016 par *MAXI* ('Monitor of All-sky X-ray Image') après plus de vingt années d'inactivité (Negoro et al., 2016; Masumitsu et al., 2016). Elle fut alors l'objet d'un suivi intensif tout au long de l'eruption 2016-2017, offrant la possibilité d'étudier la physique de l'accrétion et de l'éjection au cours de l'évolution spectrale. En particulier, l'analyse spectrale en rayons X de GRS 1716–249 offre une opportunité unique de contraindre les paramètres physiques du flot d'accrétion chaud et d'observer comment la géométrie du disque d'accrétion évolue pendant les transitions spectrales. De plus, l'adoption d'une approche observationnelle à plusieurs longueurs d'onde, combinée à la modélisation des processus radiatifs m'a donné l'extraordinaire possibilité d'étudier l'origine de l'émission de haute énergie observée au-dessus de 200 keV lorsque la source était à l'état dur.

Structure de la thèse

Cette thèse est divisée selon les chapitres suivants: les trois premiers chapitres sont principalement axés sur la description générale des binaires X, avec une attention particulière à la phénoménologie des transitoires à trou noir (**Chapitre 1**), les différentes composantes de la matière en interaction: le flot d'accrétion (**Chapitre 2**) et les flots d'éjection (**Chapitre 3**), en plus des principaux processus d'émission impliqués dans les différents états spectraux. Le **Chapitre 4** constitue un aperçu des instruments à différentes longueurs d'onde utilisés pour observer l'éruption de 2016-2017 de GRS 1716–249. De plus, dans ce chapitre, je présente les concepts de base des méthodes d'analyse de données X et gamma que j'ai utilisées. Dans le **Chapitre 5**, je détaille l'analyse spectrale et temporelle des observations X effectuées sur cette source lors de l'éruption de 2016-2017, ainsi que l'interprétation physique des résultats. Puis, en me concentrant sur l'émission X et gamma de GRS 1716–249, j'ai détecté la présence d'une composante spectrale en excès du spectre de comptonisation thermique au delà de 200 keV. Dans le **Chapitre 6**, je décris les méthodes adoptées pour étudier l'origine de cette composante à haute énergie. Cette composante pourrait provenir soit de Compton inverse sur les photons mou émis par le disque diffusés par des électrons non thermiques de la couronne, soit de l'émission synchrotron de leptons énergétiques dans le jet. Ces deux possibilités sont discutées et testées à l'aide de différents modèles spectraux.

Chapter 2

Galactic black hole binaries

Thanks to the always more sensitive X-ray telescopes, the number of known binary systems containing a black hole (called black hole binaries, BHBs) continues to increase with time. At present, more than 60 BHB candidates are known (for recent catalogues I refer to Tetarenko et al. (2016) and `http://www.astro.puc.cl/BlackCAT/index.php`).
Based on their X-ray flux variability it is possible to classify these systems in *persistent* and *transient*. The BHBs belonging to the first group show a steady X-ray emission (L$\sim 10^{36-39}$ erg s^{-1}), while *transient* BHBs (Black Hole Transient, BHT) alternate quiescent periods characterised by X-ray luminosities $L_X \sim 10^{30-33}$ erg s^{-1} and episodic outbursts during which the source can reach $L_X \sim 10^{36-39}$ erg s^{-1}. Typically, the HMXBs hosting a BH have been observed in a persistent state (as Cyg X–1, LMC X-3 and M33 X-7; Remillard & McClintock, 2006) due to a long-term mass transfer driven by a stellar wind. While, most black hole transients are LMXBs.
The outbursts are thought to be due to thermal and viscous instability in the accretion disc (Meyer & Meyer-Hofmeister, 1981; Lasota, 2001). They are responsible for the growth of the mass transfer onto the BH and lead to bright X-ray emission. When the BHT decays back to quiescence, the accretion disc cools and enters into a neutral state. In this phase it is possible to detect the UV/optical emission from the companion star and to use it to determine the orbital parameters of the system to infer the compact object mass (see Section 2.1). During these outburst the X-ray light curve of a BHT, which represents the flux measured in a defined energy range as a function of time, can show high flux variability on time scales of ms up to months. The light curves of BHTs have similar shapes: a fast rise followed by an exponential decay (see Figure 2.1), although a variety of features (e.g. plateaus, multiple peaks) have been observed (Chen et al., 1997).
A number of different X-ray spectral states, characterized by different luminosities (low or high), spectral shapes (hard or soft; Remillard & McClintock, 2006; Done et al., 2007) and timing properties (Belloni & Motta, 2016) are observed during the outbursts. They are usually described in terms of changes in the geometry of the accretion flow (see Section 2.4.4). A detailed description of the different spectral states and their evolution is given in Section 2.4. The main processes

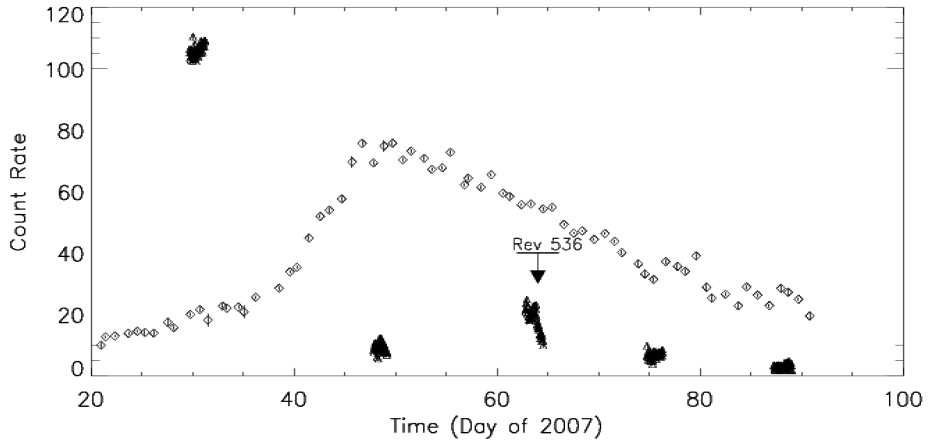

Figure 2.1: X-ray light curves in the 2–12 keV and 20–40 keV energy ranges of the black hole transient GX 339-4 taken from Del Santo et al. (2009).

responsible for the emission observed in UV and X-rays energy bands are the thermal emission from a geometrically thin, optically thick accretion disc and the Comptonized emission of soft disc photons by geometrically thick, optically thin hot plasma (see Sections 2.2 and 2.3 for more details).

2.1 X-ray binary systems

Thanks to the efficient conversion of the accreting matter into radiative energy, X-ray binaries are the most powerful X-ray emitters in our Galaxy. These systems consist of two interacting objects: a compact object, which can be a BH or a neutron star (NS), and a non-degenerate secondary star (companion star). Owing to gravity, the matter accreted from the companion star falls onto the compact object reaching X-ray energies. At some stages of their evolution, depending on the physical parameters of the binary system, XRBs can transfer matter through two main processes (Frank et al., 1987):

- *stellar wind.* During a particular evolutionary phase of the system the companion star ejects part of its mass in the form of a stellar wind. A fraction of this outflow is captured gravitationally by the compact object;
- *Roche lobes outflow.* This can occur both if the star evolves and increase its radius and if the system reduces its dimension. In both cases the system reaches a point where the gravitational attraction of the compact object removes the outer layers of the companion star (see Section 2.2.1).

It is known that the mechanism which leads the matter to leave the companion star and to be accreted onto the compact object is determined by the mass of the companion star (see figure 2.2). Based on this parameter, the X-ray binaries are classified as low-mass or high-mass X-ray binaries (LMXBs and HMXBs, respectively).

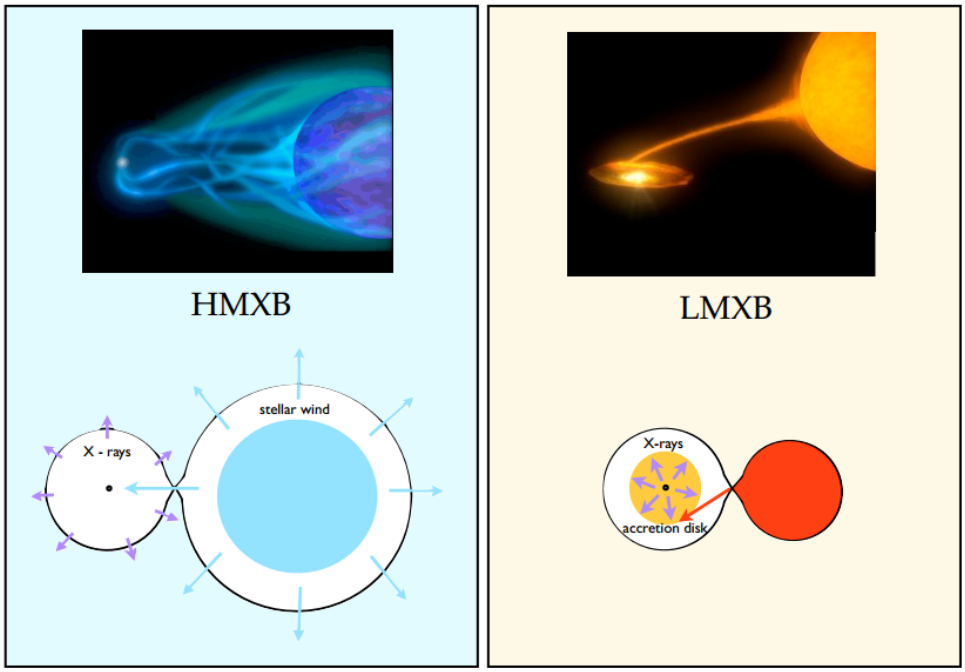

Figure 2.2: Artist's view (top) and a schematic view (bottom) of high mass and low mass X-ray binaries. Each panel shows the accretion modes in the different binary system, respectively by stellar wind and by Roche lobe overflow via an accretion disc. Credit: Egron (2013).

In HMXBs, the companion star is a young massive star (M$\gg 5M_{\odot}$) of spectral type O-B. These systems are relatively young objects ($\sim 10^7$ years) and they are mostly distributed near the Galactic plane. The accretion onto the compact object occurs through a strong stellar wind, which may be driven by absorption of UV photons from the companion or X-ray heating. LMXBs, instead, are old systems ($\sim 10^{8-9}$ years) mostly concentrated in the Galactic central region and in globular clusters, in which the donor is a low mass star (M$\leq 1\,M_{\odot}$). In this case the matter is transferred only through Roche lobe overflow and accreted through an accretion disc (see Section 2.2.1).

In some cases the emission observed can provide information on the nature of the compact object. Direct and strong evidence of the presence of a NS in the accreting binary systems is the detection of coherent pulsations and/or of type-I X-ray bursts. Unlike neutron stars, black holes do not have a surface and, therefore, are not expected to show these phenomena. Through the observable orbital parameters of the binary system (e.g. the orbital period, P_{orb}, and the radial velocity) and the identification of the companion star, it is possible to infer a lower-limit on the mass of the compact object:

$$f(M) = \frac{K_c^3 P_{orb}}{2\pi G} = \frac{M \sin^3 i}{(1+q)^2} \tag{2.1}$$

where K_c is the half-amplitude of the velocity curve of the secondary star, i is the

inclination angle of the system and the ratio between the mass of the companion star and that of the compact object is given by $q = M_c/M$. The average mass of a neutron star is estimated to be about $1.4\,M_\odot$, while sources with $M > 3\,M_\odot$ are classified as black holes (Ruffini, 1974).

BHs can be described by three parameters: the mass M_{BH}, the angular momentum J, and the electric charge Q (a charged BH would quickly neutralise by attracting charge of the opposite sign, therefore astrophysical BHs are expected to have $Q = 0$). Any other information is lost during their formation. Usually the angular momentum is expressed in terms of specific angular momentum (or spin)

$$a = \frac{J}{cM}. \tag{2.2}$$

For convention, we refer to the dimensionless spin parameter $a_* = a/R_g$ (where $R_g = GM/c^2$ is the gravitational radius), which lies between 0 and 1 for a non-rotating and a maximally rotating BH, respectively.
Black holes are delimited by an immaterial spherical surface called *event horizon* and its radius is:

$$R_H = R_g[1 + (1 - a^2)^{\frac{1}{2}}] \tag{2.3}$$

From 2.3 it is evident that the radius of the event horizon changes according to the BH spin. In a non-rotating BH the event horizon is the Schwarzschild radius: $R_H = R_S = 2GM/c^2$. Close to the BH there are no stable orbits and the accreted material plunges into the BH. The accretion disc terminates at the so called *innermost stable circular orbit* (ISCO) which, for a non-rotating black hole, is located at $R_{ISCO} = 3R_S$, while in Kerr BHs the accretion disc can extend down to the event horizon $R_H = R_{ISCO} = R_g$.

2.2 Accretion onto a black hole

A natural and powerful mechanism to produce X-ray radiation is the accretion of matter onto a compact object. During the free falling of matter with a rate $\dot{M} = \frac{dM}{dt}$ the gravitational potential energy is converted in kinetic energy. Assuming that all the kinetic energy of the accreting matter is given up to radiation at the object surface of mass M and radius R, the accretion luminosity can be expressed as:

$$L_{acc} = \frac{GM\dot{M}}{R} \tag{2.4}$$

where G is the gravitation constant[1]. However for a black hole, not all the accretion energy is radiated, this uncertainty is related to the efficiency of the conversion of the accreted matter into luminosity, which depends on the compactness of the accreting object η (the gravitational radius of the compact object over its radius). Thus, the accretion luminosity (Eq. 2.4) can be expressed as:

$$L_{acc} = \eta\dot{M}c^2 \tag{2.5}$$

[1] G=$6.674 \times 10^8 cm^3 g^{-1} s^{-2}$

where c is the light speed. However, a black hole does not have a solid surface. In this case the efficiency parameter is given by the difference of the energy per unit mass of a particle at rest at infinity and that of a particle on the last stable circular orbit: the energy dissipated to reach last stable orbit of the BH. Such energy, in units of mc^2, is about 0.06 for a Schwarzschild BH and about 0.42 for a maximally rotating black hole ($a_* = 1$) BH (Longair, 2011).
If the rate at which the matter is being accreted becomes too high, the radiation pressure may contrast the gravitational forces. Therefore, the processes of scattering and absorption of source photons from the infalling matter reduce the rate at which it is accreted. This results in an upper limit onto the luminosity of the system, called Eddington Luminosity. Assuming Thompons scattering as the only interaction process between matter and radiation, the Eddington luminosity depends by the mass of the black hole:

$$L_{\mathrm{Edd}} = \frac{4\pi G M m_p c}{\sigma_{\mathrm{T}}} \simeq 1.3 \times 10^{38} (\frac{M}{M_\odot})\, erg\, s^{-1} \tag{2.6}$$

where m_p is the proton mass and σ_{T} is the Thompson cross section[2]. Above this value, the radiation pressure exceeds the gravitational attraction and the matter cannot be accreted any longer.

2.2.1 Roche lobe overflow

The transfer of mass in low mass X-ray binary systems occurs through Roche lobe overflow (see Section 2.1).
The teardrop-shaped space defining the region in which material is gravitationally bound to the star is called *Roche lobe*. In a binary system where two stars orbit each other under the mutual gravitational attraction, considering the orbit of a test particle in the gravitational potential of the binary system, we can assume:

- the two stars are so massive that a test particle would not perturb their orbits;
- the two stars follow Keplerian orbits around each other. This assumption is generally correct because the tidal effects tend to circularise their orbits in shorter time than the time required to the matter to be transferred;
- we can consider the stars involved in the system as point masses.

The Roche's potential to which is subjected the test mass located at a distance r from the mass centre of the system can be expressed as:

$$\Phi(r) = -\frac{GM_1}{r_1} - \frac{GM_2}{r_2} - \frac{(\Omega r)^2}{2} \tag{2.7}$$

where r_1 and r_2 are the distances to the centre of the stars of masses M_1 and M_2 and Ω is the orbital angular velocity (Longair, 2011). The Roche's potential takes into account the gravitational attraction of each of the two stars as well as

[2] $\sigma_{\mathrm{T}} = 6.7 \times 10^{-25}\,\mathrm{cm}^{-2}$

the centrifugal force. Figure 2.3 shows some sections of the equipotential surfaces and the surface representing the Roche potential for a binary system. The shape of the equipotential surfaces and the dimension are determined by the masses ratio q= $\frac{M_2}{M_1}$ and the binary separation a (Frank et al., 2002).

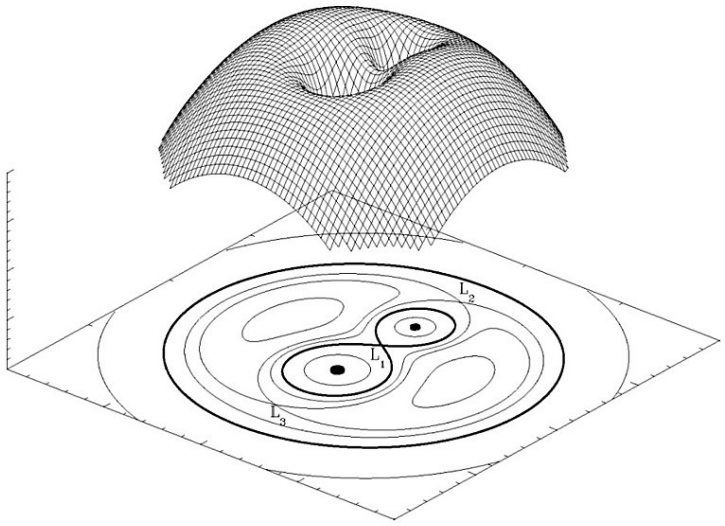

Figure 2.3: Sections of the equipotential surfaces and of the Roche lobes.

The matter moves inside these surfaces driven by the gravitational force of the nearest star. The largest closed equipotential surface surrounding each star is the Roche lobe. The points where the gravitational and centrifugal forces balance each other out, are called *Lagrangian points* (L). The point at which the Roche lobes touch each other is the *inner Lagrangian point* L_1.
During the system evolution one of the two stars may increase in radius (hereafter donor star) up to the point where the gravitational pull of the companion can remove the outer layers of its envelope (Frank et al., 2002). Assuming that one of the two stars has evolved so that its surface has filled its Roche lobe, the pressure gradient or any perturbation push the gas through L_1 into the Roche lobe of the second star just causing the accretion process. Then, the mass transfer continues as long as the donor star fills the Roche lobe. We refer to this kind of mass transfer as *Roche lobe overflow*.

2.2.2 Standard model of thin accretion disc

In the framework of the mass transfer through Roche lobe outflow (see Section 2.2.1), the material cannot accrete straight onto the compact object due to the high specific angular momentum. The stream of matter follows an orbit close to that of a free particle released at L_1 and falls down in the gravitational field of the compact object with a certain angular momentum. This spiralisation results in dissipative processes such as collisions of gas elements, shocks and viscous dissipation. These processes convert a fraction of the orbital energy of the accreting matter into internal energy which can be partly radiated. To reduce the angular

momentum, the falling matter tends to follow the minimum energy orbit with the specific angular momentum. Since the energy is dissipated through radiative cooling on faster time scales than the timescale on which the spiralising matter redistributes its angular momentum, the formation of an accretion disc is possible. In absence of external torques, the excess of angular momentum is transported towards the outer part of the disc. The standard disc model (Shakura & Sunyaev, 1973) provides the description of a geometrically thin and optically thick accretion disc, which is radiatively efficient and dominated by the gas pressure. Requesting that the disc is geometrically thin or Keplerian is equivalent to assuming that the disc is efficiently cooled (Shakura & Sunyaev, 1973).
The general equations of the accretion flow are obtained from the hydrodynamics equations, taking into account the viscosity $\nu = \alpha c_s H$ (c_s is the sound speed and H is the scale height of the disc) that is parametrised by the adimensional parameter α, the state equation of the gas and the radiative processes.
The dissipation rate per surface unit can be written as (for details I refer to Frank et al., 2002):

$$D(R) = \frac{3GM\dot{M}}{8\pi R^3}\left[1 - \left(\frac{R_*}{R}\right)^{\frac{1}{2}}\right] \tag{2.8}$$

where R_* is the inner radius of the disc. Taking into account both sides of the disc, the luminosity radiated between R_1 and R_2 is

$$L(R_1, R_2) = 2\int_{R_1}^{R_2} D(R) 2\pi R dR \tag{2.9}$$

Integrating Equation 2.9 from R to $R_{max} \to \infty$ we obtain the total disc luminosity

$$L_{\rm disc} = \frac{GM\dot{M}}{2R} = \frac{1}{2}L_{\rm acc} \tag{2.10}$$

2.2.2.1 The emitted spectrum

The assumption that the disc is optically thick to the radiation implies that photons will be scattered several times before escaping the disc, in addition to be absorbed and emitted, which entails a continuous exchange of kinetic energy between particles and photons. This allows us to approximate the emission of the disc surface at each radius as a blackbody with temperature T(R). Setting the dissipation rate (see Eq. 2.8) equal to the local blackbody emission

$$\sigma T^4(R) = D(R), \tag{2.11}$$

where σ is the Stefan-Boltzmann constant[3], we obtain:

$$T(\mathrm{R}) = \left(\frac{3\mathrm{GM}\dot{\mathrm{M}}}{8\pi \mathrm{R}^3\sigma}\left[1 - \left(\frac{\mathrm{R}_*}{\mathrm{R}}\right)^{\frac{1}{2}}\right]\right)^{\frac{1}{4}} \tag{2.12}$$

[3] $\sigma = 5.67 \times 10^{-5}\,\mathrm{erg\,cm^{-2}\,s^{-1}\,K^{-4}}$

For R>>R$_*$ the temperature of each annulus of the disc increases toward the innermost part of disc as

$$T(R) \propto R^{-\frac{3}{4}} \tag{2.13}$$

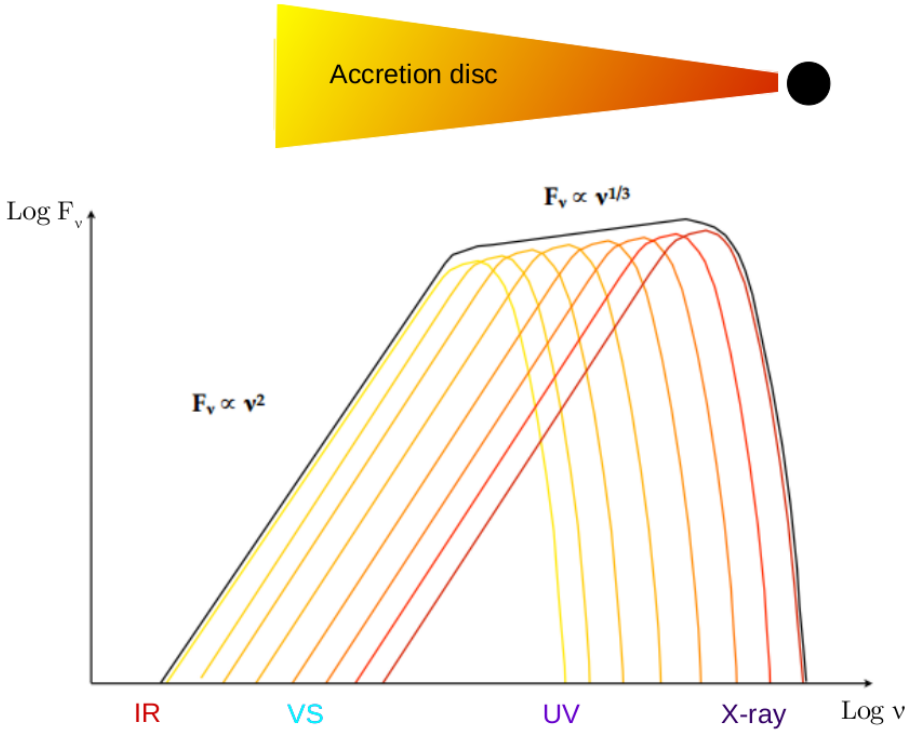

Figure 2.4: Schematic representation of the spectrum resulting from the superposition of blackbody components originating from individual rings in the optically-thick accretion disc.

The total emission of the disc results by the overlap of several blackbody spectra (see Figure 2.4).
The flux at frequency ν, for an observer at a distance D, whose line of sight makes an angle i with the disc plane is:

$$F_\nu = \frac{2\pi \cos i}{D^2} \int_{R_*}^{R_{max}} I(\nu) r dr \tag{2.14}$$

where the specific intensity emitted by each element of the surface is the Plank function:

$$I(\nu) = \frac{2h\nu^3}{c^2 \left(e^{\frac{h\nu}{kT(R)}} - 1 \right)} \tag{2.15}$$

The final spectrum is shown in Figure 2.4. The shape of the spectrum depends on the frequency (Rybicki & Lightman, 1979; Longair, 2011):

- at low frequencies $\nu << \frac{kT}{h}$, the intensity I(ν) becomes very close to the Reyleigh-Jeans form ($I(\nu) = \frac{2kT\nu^2}{c^2}$) with the flux proportional to the square of the frequency ($F_\nu \propto \nu^2$);

- at high frequencies ($\nu >> \frac{kT}{h}$), the Planck spectrum is in the Wien regime ($I(\nu) = \frac{2h\nu^3}{c^2 e^{-\frac{h\nu}{kT}}}$). Therefore, the spectrum is dominated by the hottest part of the disc and it falls with an exponential tail.

- Then, at intermediate frequencies $F_\nu \propto \nu^{\frac{1}{3}}$.

This multi-colour black body model is implemented into XSPEC as DISKBB (in XSPEC, Mitsuda et al., 1984) and allows us to fit the observed spectra of accretion discs. The model takes into account the temperature at the inner disc radius (kT_{in}) expressed in keV and the normalisation:

$$k = \left(\frac{R_{in}}{D_{10}}\right)^2 \cos\theta \tag{2.16}$$

where R_{in} is the apparent inner disc radius in km, D_{10} is the distance to the source in units of 10 kpc, and θ the inclination angle of the disc. It is worth noticing that the model does not include the correction factors: i.e. the torque-free boundary condition term (Kubota et al., 1998) necessary to evaluate the relativistic effect in the multi-colour disc approximation and the hardening factor (Shimura & Takahara, 1995) which evaluates the ratio between the colour and the effective temperature.

2.2.3 Irradiated disc

An important effect which we should evaluate when studying the emitted accretion disc spectrum, is the self-irradiation. The outer part of the accretion disc can be heated by the radiation emitted by the inner regions.

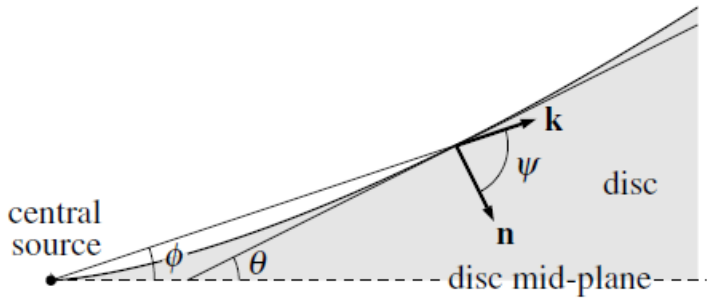

Figure 2.5: Irradiated disc geometry. The unit vector **k** and **n** indicate the direction of propagation of the radiation incident on the disc and the local inward-directed normal vector, respectively. Figure from Frank et al. (2002).

The total radiative flux at disc radius R can be expressed as a function of the irradiating luminosity (L_{irr}) as:

$$F = \frac{L_{irr}}{4\pi R^2} \tag{2.17}$$

if the central source is considered as point (Frank et al., 2002). The flux crossing the disc surface therefore is:

$$Q_{irr} = \frac{L_{irr}}{4\pi R^2}(1-\beta)\cos\psi \tag{2.18}$$

where $\psi = \frac{\pi}{2} - \vartheta + \phi$ is the angle between the local inward-directed disc normal and the direction of the incident radiation (see Figure 2.5) and β expresses the fraction of incident radiation scattered from the surface without absorption.
The heating rate due to irradiation can be written as (Sanbuichi et al., 1993):

$$Q_{irr} = (1-\beta)\frac{L_{irr}}{4\pi R^2}\left(\frac{dH}{dR} - \frac{H}{R}\right) \tag{2.19}$$

where H is the local scale height and both $\tan\vartheta = dH/dR$ and $\tan\phi = H/R$ are lower than 1 in a thin accretion disc.
At this point it is possible to obtain the structure and spectrum of the irradiated accretion disc taking into account also the viscous heating inside the disc. We assume a steady, geometrically thin (all physical quantities are integrated along the vertical direction) and axisymmetric disc where the self-gravity of the matter can be ignored. In addition, the disc is optically thick and heated by the X-ray source. These conditions lead to the same continuity equation, angular momentum conservation, hydrostatic equilibrium equation, and the equation of state governing the standard discs, except for the energy equation. In this case, the energy balance equation is:

$$2\sigma T^4 = \frac{3GM\dot{M}}{4\pi R^3} + Q_{irr} \tag{2.20}$$

where Q_{irr} is Equation 2.19.

2.2.3.1 Spectrum of Irradiated discs

The self-irradiation leads to spectral variation in the low energy part of the disc spectrum. Therefore, it is important to evaluate its effects in the study of the accretion disc in XRBs.
Knowing how varies the temperature as a function of radius, it is possible to compute the spectrum of a self-irradiated disc around a Schwarzschild black hole. It is worth noticing that the irradiated disc is divided in two parts by the standard theory: i.e. an inner disc where the viscous heating is dominant and an outer disc dominated by the self-irradiation. Since the self-irradiation involves mainly the outer part of the disc, the spectrum has been calculated under the Newtonian approximation (see Sanbuichi et al., 1993).
From Equation 2.20, it is possible to show that the surface temperature of the inner and outer disc is (Sanbuichi et al., 1993):

$$T(R) \propto \begin{cases} M^{\frac{1}{4}}\dot{M}^{\frac{1}{4}}R^{-\frac{3}{4}} & R_{in} \leq R \leq R_B \\ (1-\beta)^{\frac{2}{7}}b^{\frac{2}{7}}M^{-\frac{1}{7}}\dot{M}^{\frac{2}{7}}R^{-\frac{3}{7}} & R_B \leq R \leq R_{out} \end{cases} \tag{2.21}$$

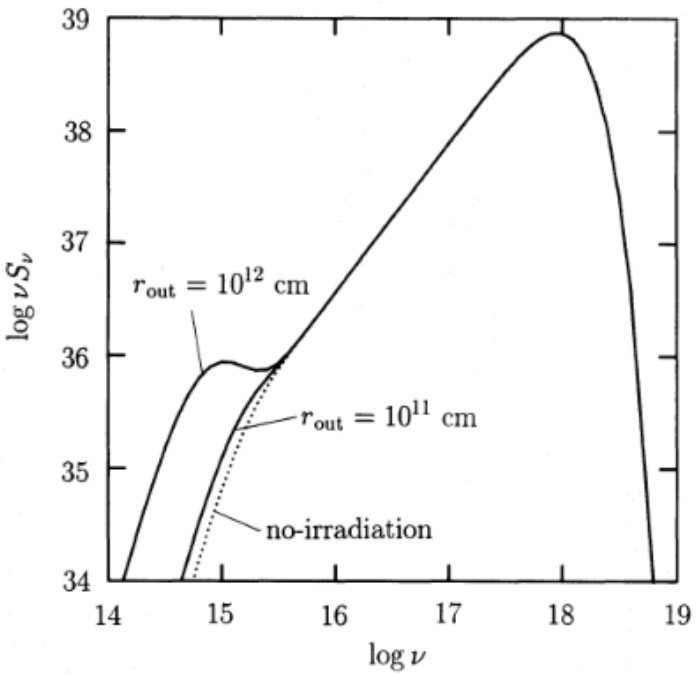

Figure 2.6: Spectrum of the self-irradiated disc around a Schwarzschild black hole. The low-fequency part of the spectrum is modified by the presence of self-irradiation if the disc is sufficient large. Figure from Sanbuichi et al. (1993).

where b is the ratio between the irradiated luminosity and the total disc luminosity, R_{in} and R_{out} are the inner and outer radius of the disc and R_B is the radius of the annulus at which self-irradiation is assumed to change regime.
Assuming that the surface of the disc radiates as a blackbody (see Eq. 2.14) and integrating the specific intensity (I_ν) of the disc over its surface, we obtain the observed flux F_ν. Using the surface temperatures 2.21, the emergent spectrum results as characterised by two peaks (see Figure 2.6). At high energies the radiation from the inner viscous disc is dominant and the flux varies as $F(\nu) \propto \nu^{\frac{1}{3}}$. While at low energies (optical and UV bands in the case of the accretion disc of LMXB) we observe the outer part of the disc, which is dominated by the self-irradiation and the flux varies as $F(\nu) \propto \nu^{-\frac{5}{3}}$ (Sanbuichi et al., 1993).

In Chapter 6, to fit the accretion disc which emission taking into account the effects of the irradiation, I adopted the XPSEC model DISKIR (Gierliński et al., 2008, 2009).
The model evaluates the effects due to the disc is irradiated by the Compton tail. This may occur in the hard state of BHTs leading to variations in the inner disc temperature structure from that expected from an unilluminated disc. The irradiated inner disc and Compton tail can illuminate the rest of the disc, and a fraction f_{out} of the bolometric flux is thermalised to the local blackbody temperature at each radius. This reprocessed flux generally dominates the optical/UV band.

The parameters of the model are the innermost temperature of the not illuminated disc (kT_{disc}), the ratio of luminosity in the Compton tail to that of the not illuminated disc (L_c/L_d), the fraction of luminosity in the Compton tail which is thermalised in the inner disc (f_{in}) and the fraction of bolometric flux which is thermalised in the outer part (f_{out}). Further parameters are the radius of the Compton illuminated disc in terms of the inner disc radius (r_{irr}), the logarithm of the outer disc radius in terms of the inner disc radius ($\log r_{out}$) and the Comptonising parameters: i.e. the electron temperature ($\mathrm{kT_e}$) and the power law photon index (Γ).

2.3 Hot accretion flow

It is generally assumed that a hot, optically thin cloud, called *corona* surrounds the compact object and can also envelope part of the inner regions of the accretion disc. Even though several analytical solutions and models of this hot accretion flow have been developed, its nature and geometry are still not fully understand. This component was initially explained with the hot (close to the virial temperature), gas pressure dominated, optically thin *accretion-dominated accretion flow* solution (ADAF, Ichimaru, 1977; Narayan et al., 1994; Abramowicz & Lasota, 1995; Narayan & McClintock, 2008). The main consequence of the high pressure condition is that the accretion flow becomes geometrically thick. However, this flow results extremely optically thin ($\tau << 1$) and it was shown that it can exist only at very low luminosity ($\mathrm{L} \leq 0.01\,\mathrm{L_{Edd}}$ Esin et al., 1997). Further and more complex analytic solutions based on ADAF were proposed taking into account extra factors: e.g. Yuan (2001) extended luminosity range of validity of the ADAF solution up to $\mathrm{L} \leq 0.1\,\mathrm{L_{Edd}}$ (LHAF). Nevertheless, none of the ADAF-based solution can account for the observed bright hard state: i.e. high luminosities ($\mathrm{L} > 0.1\,\mathrm{L_{Edd}}$), low energy electron temperature ($\mathrm{kT_e} \sim 40\,\mathrm{keV}$) and the high optical depth ($\tau > 1$).
A crucial factor to take into account in the accretion process is the presence of magnetic field. Indeed, the magnetic pressure due to the strong magnetic field can support efficiently the hot flow (Oda et al., 2010, 2012), allowing for solutions with large τ. The spectral studies performed on the corona of Cyg X–1 are consistent with this hot accretion flow solution (Malzac & Belmont, 2009; Del Santo et al., 2013).
Recently, a multi-flow configuration Jet Emitting Disc model was proposed and elaborated by Ferreira et al. (2006) and Marcel et al. (2018a,b, 2019). The JED model provides a physical understanding of what is the corona and how it can produce jets. According to the model, accretion disks are made of two radial extended regions an outer optically thick Standard Accretion Disk (SAD) and an inner, optically thin Jet Emitting Disk (JED), separated by a transition radius. Varying independently the disc accretion rate and the disc magnetisation, the location of this radius changes and subsequently the contribution of the two different discs. Thus providing an explanation for the different spectral states and the jet properties observed.

2.3.1 Radiation processes in hot accretion flows

In this section I review the process of Comptonisation which plays a fundamental role in X-ray emission of compact objects. For an extensive description of the radiation process I refer to Rybicki & Lightman (1979); Longair (2011).
Moreover, I briefly describe the main XSPEC spectral models I adopted in my research to describe the Comptonised emission of GRS 1716–249 (the analysis are reported in Chapters 5.3 and 6).

2.3.1.1 Thermal Comptonisation

The scattering between photons and electrons is one of the main causes of the non-thermal X-ray component observed in BHBs spectra.
If the energy of the photons is smaller than the electrons rest mass energy ($h\nu << m_e c^2$), we refer to *Thomson scattering*. The interaction results in an elastic collision where the photons change their direction of propagation. When the photons have an energy comparable to the electron rest energy ($h\nu \sim m_e c^2$) the collision becomes inelastic and the photon-electron interaction results in a loss of energy to the photon.
Considering a collision between a moving electron with initial energy $E = \gamma m_e c^2$ and arbitrary photon with initial energy $\epsilon = h\nu$, and the conservation of momentum and energy, the general formula for the exchange of energy for the photons is:

$$\frac{\nu'}{\nu} = \frac{1 - \beta \cos\vartheta}{1 - \beta \cos\vartheta' + \frac{h\nu}{\gamma m_e c^2}(1 - \cos\alpha)} \tag{2.22}$$

where ν is the photon frequency, ϑ the angle between the photon and the electron and α is the scattering angle. The parameters after the collision are indicated with an apex.
Considering high energy astrophysics frameworks, the electrons can move at relativistic speeds ($v \sim c$). The change in photon energy results as a Doppler effect due to the change of the reference frame. In the electron rest frame, the frequency of the incident photon is:

$$\nu_0 = \gamma\nu(1 - \beta \cos\vartheta) \tag{2.23}$$

If $h\nu_0 << m_e c^2$, we are in the Thompson scattering condition and in this frame the change of the photon energy is negligible ($\nu_0' = \nu_0$). Going back to the lab frame

$$\nu' = \frac{\nu_0'}{\gamma(1 - \beta \cos\vartheta')} = \frac{\nu_0}{\gamma(1 - \beta \cos\vartheta')} = \nu \frac{\gamma(1 - \beta \cos\vartheta)}{\gamma(1 - \beta \cos\vartheta')} \tag{2.24}$$

The amount of energy transferred from the electron to the photon is significantly high (and it reaches the maximum values in case of frontal collision with the back scattering of the photon), therefore a soft photon will be up-scattered up to the X/γ-rays energies. In this case we talk of *Inverse Compton* (IC). If the process is considered from the frame in which the electron is at rest ($v << c$) and the recoil of the photon is small, it can be neglected (*Thomson regime*). While in the case of photons energies larger than the electrons energies ($h\nu >> m_e c^2$), we cannot neglect the recoil any more (*Klein-Nishina regime*) and the quantum

effects which leads to a modification of the electron cross section, have to be taken into account.
In the the Thomson regime, assuming a distribution of photons with energy ϵ and density $n(\epsilon)$, the rate of scattering can be expressed as:

$$\frac{dN}{dt} = \int \sigma_T c(1 - \beta cos\vartheta) n(\epsilon) d\epsilon \tag{2.25}$$

where the relative velocity between the electron and the photons is $v_{rel} = c(1-\beta cos\vartheta)$. Given the rate of scattering (Eq. 2.25) and the energy of the scattered photon seen from the electron frame (Eq. 2.23), it is possible to obtain the power produced by the scattered radiation:

$$\frac{dE}{dt} = \epsilon' \frac{dN}{dt} = \sigma_T c \int \frac{(1 - \beta \cos\vartheta)^2}{1 - \beta \cos\vartheta'} \epsilon n(\epsilon) d\epsilon \tag{2.26}$$

If the incoming photons are isotropically distributed, averaging on the solid angle leads to $(1-\beta cos\vartheta)^2 = 1+\frac{\beta^2}{3}$ (Lightman & Zdziarski, 1987), therefore the powered produced is:

$$\frac{dE}{dt} = \sigma_T c \gamma^2 \left(1 + \frac{\beta^2}{3}\right) U_{IC} \tag{2.27}$$

where

$$U_{IC} = \int \epsilon n(\epsilon) d\epsilon \tag{2.28}$$

is the energy density of the radiation before the scattering (Ghisellini, 2013). Consequently, the rate at which the electron loses energy is the difference between the initial power and the scattered radiation:

$$P(\gamma) = \frac{4}{3} \sigma_T c \gamma^2 \beta^2 U_{IC} \tag{2.29}$$

It is worth noticing that the radiated power does not depend on the actual energy of the photon which could not be mono-energetic.

Thermal Comptonisation spectrum

Considering the collision of the photons distribution with a power-law electron distribution $N(\gamma) = N_0 \gamma^{-p}$ $(\gamma_{min} < \gamma < \gamma_{max})$, the resulting average photon frequency is:

$$\nu_{\rm av} = \frac{4}{3} \gamma^2 \nu_0 \tag{2.30}$$

and the emitted spectrum from a single scattering is

$$j(\nu) \sim \frac{2}{3} \sigma_T c U_{IC} \frac{N_0}{\nu_0} \left(\frac{3\nu}{4\nu_0}\right)^{-\alpha} \tag{2.31}$$

where $\alpha = \frac{p-1}{2}$.
In a real astrophysics environment the photons will do a random walk before

before escaping the medium, therefore they may be scattered zero, one ore several times. The numbers of scatters decreases exponentially with the distance:

$$N = N_0 e^{-\int \sigma_T n_e dx} \tag{2.32}$$

where n_e is the electron density, N_0 is the number density of photons per unit volume and the optical depth of the medium is defined as $\tau_T = \int \sigma_T n_e dx$. Therefore, the total number of scattering which may occur in the plasma $N = max[\tau_T, \tau_T^2]$ depends by the Thomson scattering optical depth τ_T. At low optical depth ($\tau_T << 1$) the photons escape by the source after at least one scatter, while at high optical depth ($\tau_T >> 1$) the photons make τ_T^2 scatters on average before to leave the source (Lightman & Zdziarski, 1987).
In the case of multiple Compton scattering (which imply high optical depth), if the density of the emitting region is large, the particles will be thermilised. We can talk of a thermal electrons distribution (Maxwellianan) or quasi-thermal if the distribution is not a perfect Maxwellianan. The resulting photon spectrum is said to be thermally Comptonised. The photons will continue to gain energy as long as their energy ($h\nu$) remains smaller than the electrons one (kT_e). The average gain of energy per number of scatters is defined as the *Compton parameter*:

$$y = 4N \frac{kT_e}{m_e c^2} \tag{2.33}$$

The photons with an initial energy E_0, after multiple scatters are emitted with an average energy (Lightman & Zdziarski, 1987)

$$E = E_0 e^{4y} \tag{2.34}$$

For $y << 1$ the Compton process does not have significant effect of the spectrum, while for $y >> 1$ the variations of the spectrum are not negligible and depend mainly by the electron temperature. The Compton processes saturates and photons enter in equilibrium with the electrons. This will result in a Wien spectrum. The most interesting case is the unsaturated Comptonisation ($y \sim 1$). The final spectrum is the the sum of the single spectra due to the different scatters. The final spectrum depends on both the optical depth and the electron temperature. At $\tau_T \geq 1$ the spectrum leads to a power law with a high energy cut-off defined by the electron temperature (usually at 50–100 keV, see Section 2.4). Harder spectra (with slope $\Gamma < 2$) are produced for higher τ_T and kT_e.
Modelling the observed Comptonised spectra allows one to infer these parameters.

The simplest model I adopted to describe the continuum from thermal Comptonisation in the corona of GRS 1716–249 is NTHCOMP (in XSPEC, Zdziarski et al., 1996; Życki et al., 1999). The parameters are the electron temperature of the corona (kT_e), the photon index of the asymptotic power law (Γ) and the seed photon temperature (kT_{bb}). The seed photons population is inserted through the parameter *input type*, which can assume a blackbody (*input type*=0) or a disc-blackbody (*input type*=1) shape.

2.3.1.2 Hybrid Comptonisation

There are cases in which a purely thermal electron distribution is not enough to explain the observed emission. Some observative findings in BHBs as:

- the absence of a cut-off energy in the high energy tail observed in SS spectra (Section 2.4);
- the excess observed in HS spectra in addition to thermal Comptonisation component (see Section 2.4.1)

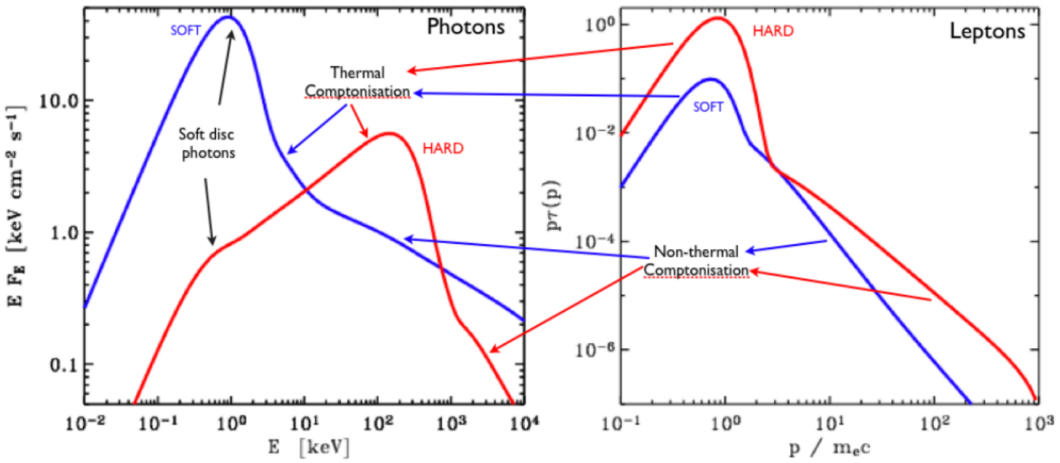

Figure 2.7: The distributions for Cyg X–1 HS (red line) and SS (blue line) spectra. In the left panel is shown the photon distribution in the corona. In the right panel is displayed the energy distribution of the Comptonising electrons. The Figure is from Malzac (2012).

suggested that some electrons may be accelerated by non-thermal mechanisms (e.g. in shocks or magnetic reconnection) forming a non-thermal electron distribution. This led to the development of the thermal/non-thermal (hybrid) Comptonisation models. Poutanen & Coppi (1998) showed that the hybrid thermal/non-thermal model well reproduce the hard X-ray emission in all spectral states.
These models assume a Maxwellian electron distribution at low energies with electron temperature kT_e. While, at high energies the electrons are characterised by a non-thermal distribution (power-law like, see Figure 2.7). The optical depth and electron temperature derived in HS are higher than the values obtained for the SS. Thus, the thermal electron contribution dominates the hard state spectrum. While in the soft state the thermal electrons contribution is weak and the hard X-ray emission is dominated by the contribution due to the non-thermal electrons.

In the following I introduce the models implemented in XSPEC. The data analysis results are reported in Chapter 6.

EQPAIR model

The hybrid thermal/non-thermal model EQPAIR (Coppi, 1992, 1999; Gierliński et al., 1999) assumes that the emission of the disc/corona system arises from a spherical, homogeneous, isotropic, hot ionised plasma cloud with continuous injection of relativistic electrons illuminated by soft photons emitted by the accretion disc. The model takes into consideration Compton scattering, $e^{\pm}$ pair production and annihilation, Coulomb interactions and bremsstrahlung processes. The soft seed photons for thermal and non-thermal Compton scattering in the corona are assumed to be uniformly emitted by an accretion disc with a blackbody spectrum at temperature kT_{bb}.
For a detailed description of the model parameters I refer to Coppi (1992).
The properties of the plasma can be expressed in terms of the non-dimensional compactness parameter:

$$l = \frac{\sigma_T}{m_e c^3} \frac{L}{R} \tag{2.35}$$

where σ_T is the Thomson cross-section, m_e the electron mass, c the speed of light, R the radius of the emitting region. In the analysis I fixed this parameter at $R \sim 20\,R_g$.
Then, L is the total power of the source supplied to soft seed photons and electrons. The luminosity of the seed photons entering the Comptonising region is parametrised by the compactness parameter l_s, which is proportional to the luminosity of the thermal disc radiation entering the corona. Further two compactness parameters, l_{th} and l_{nth}, are introduced to quantify the heating rate of the thermal electrons, respectively. It is worth noticing that in this model, the predicted spectral shape is not sensitive to l_s but depends mostly on the compactness ratios:

- l_h/l_s, where l_h is proportional to the total power provided to the electrons of the plasma,

- l_{nth}/l_h, the power in non-thermal electrons acceleration over the total power supplied to the plasma, (i.e. including also the thermal heating of the electrons l_{th}, l_h=l_{nth}+l_{th}).

The non-thermal electrons are injected with a mono-energetic spectrum assumed to be a power law

$$N_{inj}(\gamma) \propto \gamma^{-\Gamma_{inj}} \tag{2.36}$$

extending in the Lorentz factor range $\gamma = 1.3 - 1000$. For $\Gamma_{inj} > 2$ most of the power is injected close to γ_{min}, therefore the effects produced by the variations of γ_{max} are negligible for $\gamma_{max} >> \gamma_{min}$ (Gierliński et al., 1999).
As shown in the previous Sections, another important parameter to take into account is the optical depth. The total optical depth of the thermal component τ_T is the sum of the optical depth due to the $e^{\pm}$ pairs (τ_p) and the Thompson optical depth τ_i due to the scattering on the ionised electrons in the plasma. EQPAIR model provides the values of τ_T and τ_p.
In EQPAIR is also included the reflection model (i.e. the spectral feature arising

from the Comptonised emission illuminating the disc and being scattered in the direction of the observer as a function of the solid angle subtended by the reflector, R=$\Omega/2\pi$).

BELM model

The BELM model (Belmont et al., 2008), in addition to the physical processes considered in EQPAIR, takes also into account the magnetic field located in the corona (B) and the self-absorbed synchrotron emission resulting by the interaction of the leptons with B. The effects of magnetic field is quantified through the magnetic compactness parameter:

$$l_B = \frac{\sigma_{\rm T}}{m_e c^2} \frac{RB^2}{8\pi} \tag{2.37}$$

Malzac & Belmont (2009) showed that particles accelerated trough non-thermal mechanisms can be thermalised efficiently on times scales shorter than the light crossing time of the corona under the effects of the synchrotron boiler (Haardt et al., 1994; Ghisellini et al., 1988) as well as Coulomb collisions. The synchrotron radiation produced by the interaction of the energetic non-thermal electrons with the magnetic field is efficiently absorbed by the low energy electrons. It was verified that this process transfers the non-thermal electrons energy into heating at the low energy electrons (Malzac & Belmont, 2009). Therefore, unlike EQPAIR where the electron distribution at low energies is assumed to be Maxwellian, in BELM the thermalisation process is treated self-consistently.
The model considers the emission from a sphere with radius R of a ionised proton-electron magnetised plasma in steady state taking into account three channels to inject energy in the system (Malzac & Belmont, 2009):

1) Non-thermal electron acceleration (l_{nth}) where the electrons are injected with a power law distribution (Eq. 2.36) of index Γ_{inj};

2) Coulomb heating (l_c) due to the Coulomb collision between electrons and a distribution of thermal protons. The electrons gain energy when the protons temperature is higher than that of the electrons;

3) External photons with temperature kT_{bb} coming from the accretion disc (l_s).

The total compactness therefore is the sum of all the injected power that constitutes the radiation: l=l_{nth}+l_c+l_s.
In particular in this thesis I focus on the pure Synchrotron Self Compton (SSC) case, where the protons are cold (l_c=0) and the external photons are negligible (l_s=0). Therefore, the total compactness coincides with the non-thermal compactness (l =l_{nth}). In this limit, the spectral shape depends mostly on the ratio l_B/l_{nth} and is relatively insensitive to the value of the non-thermal compactness l_{nth} or that of l_B. If we fix l_{nth}=10, the soft self-absorbed synchrotron emission produced by the interaction between the non-thermal electrons and the magnetic field (B) peaks around few eVs. This is Compton up-scattered by the

hybrid thermal/non-thermal electron distribution, extending the spectrum up to the X/γ-ray energies.

2.4 Spectral states in Black Hole Transients

As introduced in Section 2.1, the X-ray emission of BHTs during the outburst is characterised by a large phenomenology.
It is known that the different energy spectra related to spectral states show a combination of thermal and non-thermal components. The simplest classification consists of two main spectral states: the hard state (HS) and the soft state (SS), in which X-ray spectra are dominated by the hard X-ray emission and soft X-ray emission, respectively.

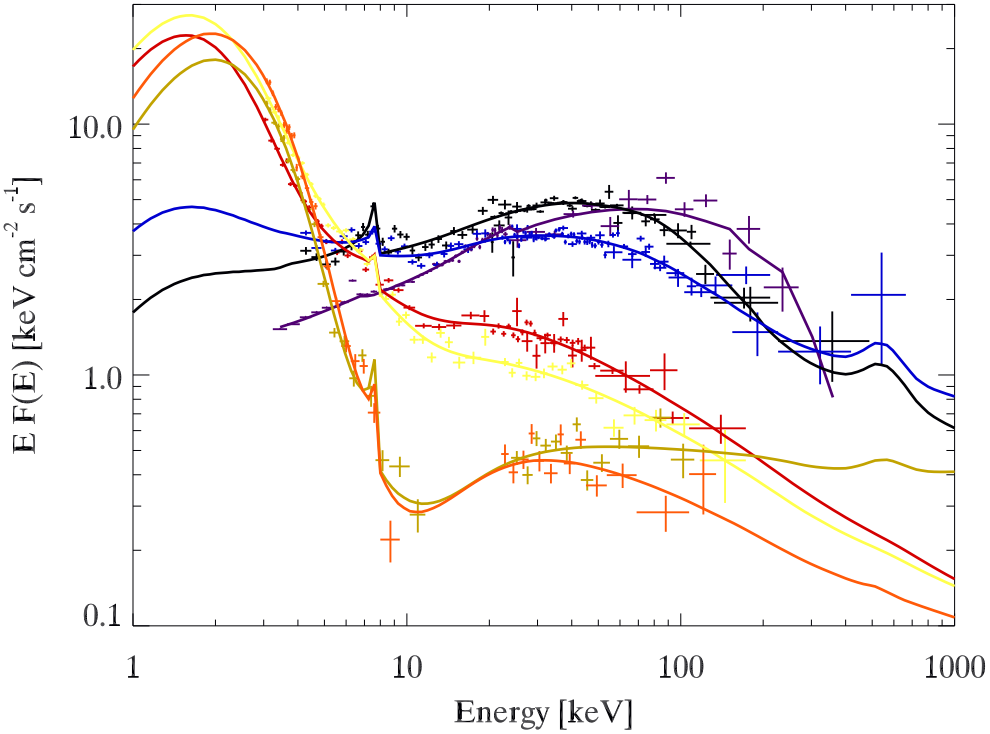

Figure 2.8: Joint JEM-X, IBIS and SPI unfolded energy spectra of GX 339–4 averaged during different spectral states in 2004 reported in Del Santo et al. (2008). Black, blue, red and yellow are intermediate state spectra. The green and orange spectra are SS. A pure HS spectrum in violet.

The HS is characterised by a dominant hard X-ray component (violet spectrum in Figure 2.8). This component is well described by a power law with typical photon index in the range $\Gamma = 1.4-2$ and a high energy cut-off at $\sim 50-100$ keV. This is physically interpreted as thermal Comptonisation due to Compton up-scattering of soft photons by hot electron plasma with electron temperature $kT_e \sim 100$ keV and Thomson optical depth $\tau \sim 1-3$. The disc blackbody emission results in a weak or absent soft X-ray thermal component in the spectrum with temperature

of $\sim 0.1 - 0.2$ keV. Then, a component above ~ 200 keV, in excess to the high energy cut-off is detected in bright sources. This emission is generally interpreted as non-thermal Comptonisation due to non-thermal electrons in the corona. However, the origin of this component is still debated (an in-depth study presented in Section 2.4.1).
The second main spectral state that can be observed during the BHTs outburst is the SS. The spectrum shows a strong soft thermal component with a disc blackbody peak temperature at $\sim$1 keV (green and orange spectra in Figure 2.8). For this reason the SS is also called "thermal dominant" (Remillard & McClintock, 2006). The thermal Comptonised emission is weak and with typical parameters $\tau \sim 0.1 - 0.2$ and $kT_e \sim 10 - 40$ keV. The SS spectrum also exhibits a spectral bump around $10 - 30$ keV and the relativistically broadened florescence iron line at $6 - 7$ keV due to Compton reflection (Done et al., 2007). In addition, a steep power-law tail with $\Gamma > 2.5$, which often extends up to the high energies ($\geq$500 keV), is observed. This high energy tail it is likely originated by an electron population with non-thermal distribution that up-scatters the disc seed photons. Further intermediate spectral states (IMS) are defined during the transition between the HS and SS. They are characterised by parameters in between the HS and the SS (black, blue, red and yellow spectra in Figure 2.8).

2.4.1 High energy tail in hard state

The first evidence of an additional high energy excess above 200–300 keV in Cyg X–1 (McConnell et al., 1994, 2002) and GX 339–4 (Wardziński et al., 2002) HS has been provided by OSSE and COPTEL telescopes. Then, the advent of *INTEGRAL* satellite allowed to observe this component both in HS and hard intermediate state spectra in a number of BHBs (Del Santo et al., 2008; Droulans et al., 2010; Del Santo et al., 2013). Usually, this component is explained as Comptonisation process due to a non-thermal electron populations in the corona (Poutanen & Coppi, 1998; Coppi, 1999; Gierliński et al., 1999; Malzac & Belmont, 2009), possibly responsible also for the tail observed in SS. An alternative scenario put jets at the origin of this hard X-ray emission produced via synchrotron radiation. The strong polarisation measurements of the hard X-ray emission above ~ 300 keV reported for Cyg X–1 support this hypothesis (Laurent et al., 2011; Jourdain et al., 2012; Rodriguez et al., 2015). Studies performed on the high energy tail of Cyg X–1, observed when the source was in HS, have shown that the emission at γ-ray energies can be explained in terms of synchrotron self-compton (SSC) processes (Zdziarski et al., 2017). However, this component is well reproduced by jet models assuming continuous particles acceleration, only when the electron distribution is harder (electron index $p \sim 1.5$) than that expected by the shock acceleration mechanism (Zdziarski et al., 2014b).

2.4.2 Hardness-Intensity Diagram

The spectral evolution of BHTs is usually described in terms of the Hardness-Intensity Diagram (HID, Homan & Belloni, 2005). This diagram is based on X-ray measurements and displays the total count rate of the source as a function of function of the hardness ratio defined as the ratio of hard to soft count rates (see Figure 2.9).

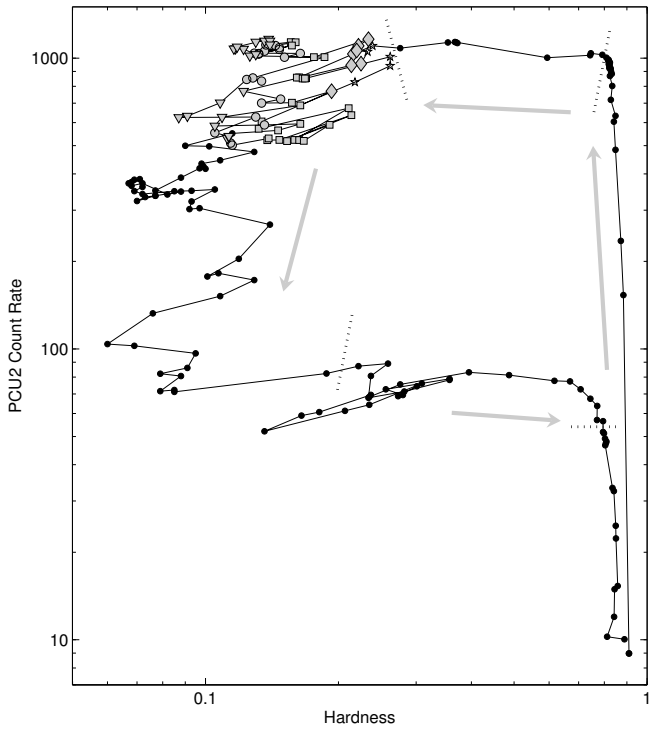

Figure 2.9: Hardness-Intensity diagram of the BHT GX 399. The grey arrows indicate the time evolution along the outburst. The Figure is taken from (Belloni et al., 2005).

The diagram assumes a typical q-shaped track travelled in counterclockwise, where the spectral states are positioned on its different regions depending on their flux. The source outburst starts faint and hard. It increases in flux and its spectrum remains hard. At some point the spectrum softens nearly constant count rate. The spectrum remains soft as the source decays, until the spectrum becomes hard again as at the start of the outburst.
The HS corresponds to the right-hand branch of the HID, while the SS is located on the left-hand side at lower hardness ratio. Further intermediate spectral states (IMS) are located on the horizontal-branches of the HID.
An important feature that characterise the HID is the *Hysteresis* (Zdziarski & Gierliński, 2004; Homan & Belloni, 2005): the transition from the hard state to soft state and from soft state to hard state occur at different luminosities, moreover there is a range of luminosities in which both the hard and soft states can be observed.

Although most of the BHT outbursts follow the q-track pattern, it was observed a number of unusual outbursts do not involve any complete state transition to softer states. Different types of these so called "failed state transition" outbursts have been observed. A recent study performed on all-sky database galactic BHTs[4] showed that almost 40% of sources are "hard only": i.e. during the outburst the source never leave the HS (HS-HIMS only, Tetarenko et al., 2016). The "failed state transition" outburst of some of these sources were observed to evolve up to the intermediate state, turning back to the hard state and finish in quiescence: e.g. H1743-322 (Capitanio et al., 2009), MAXI J1836-194 (Ferrigno et al., 2012), Swift J1753.5-0127 (Soleri et al., 2013) and Swift J174510.8-262411 (Del Santo et al., 2016). The reasons why these sources fail to make transition to the soft state is still debated. Tetarenko et al. (2016) pointed out that the mass transfer rate ($\dot{M}$) over the entire outburst could be insufficient to allow to the source to perform the transition to the soft states. Indeed, they found that all "hard only" sources show outburst peak luminosities lower than 0.11 L_{Edd}.

2.4.3 X-ray timing

The fast time variability of the X-ray emission in BHTs is characterised by a complex and of difficult interpretation phenomenology. Study the amplitude and the variations of this fast variability according to the time scales on which it occurs can provide fundamental information on the physics of these accreting systems. Through the Power Density Spectra (PDS), which represent the square of the Fourier amplitude as a function of Fourier frequency, it is possible to study the fast periodic and aperiodic variability of these sources.
PDS presents broad components which extend in the frequency range 0.1–10 Hz with transient relatively narrow peaks called Quasi-Periodic Oscillations (QPOs). These are usually identify in the frequency range 0.01–450 Hz (see Figure 6.1). The observations of different PDS showed that these features change the peak frequency during the outburst in correspondence of the different spectral states. A break around 10 Hz has been observed when the source goes towards the soft state. That is indicative of a limit to the variability: i.e. it cannot be faster than a certain timescale (Done et al., 2007). It is thought that these features are straightly associated to the changes in the geometry of accretion flow. A correspondence between the maximum value of this break and the viscous timescale for the accretion flow at its last stable orbit was found, suggesting that the break frequency may be produced at the ISCO (Ingram et al., 2009; Ingram & Done, 2012).
Even though the phenomenology of QPOs is extensively studied, their origin and physical nature are still not completely understood. The origin and the evolution of QPOs have been explained by several models. Actually, the most plausible model suggests that the mechanism leads to the origin of QPOs is based on the geometrical effects (as the orbital inclination, see e.g. Motta et al., 2015). During

[4] http://astro.physics.ualberta.ca/WATCHDOG/

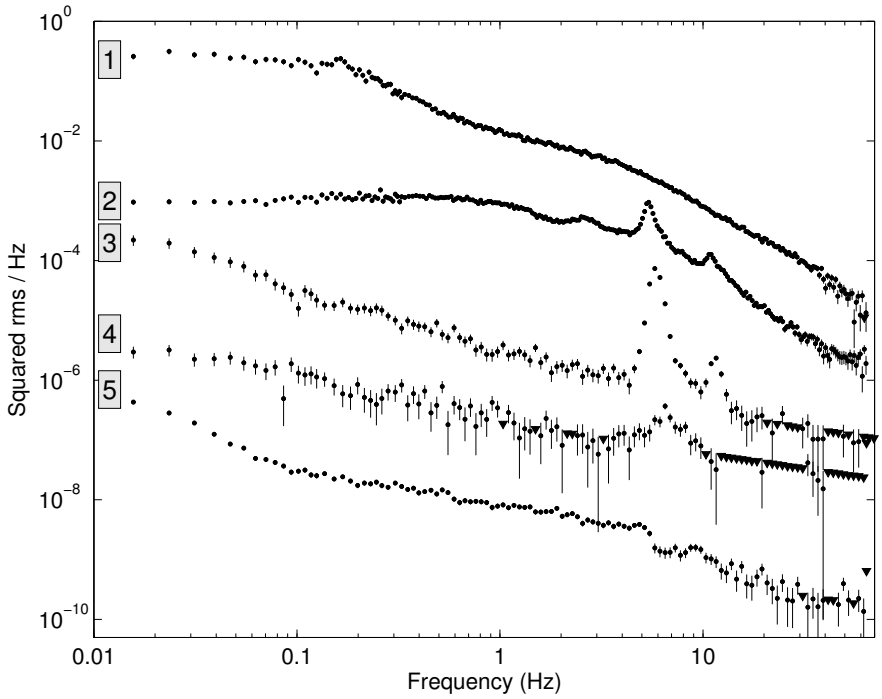

Figure 2.10: Five types of PDS observed during 2002-2003 outburst of GX 339–4. Credits Belloni (2010).

the spectral evolution of BHTs different kinds of QPOs are recognised: Type A,B and C (Casella et al., 2004). While the Type A and B QPOs are mainly observed during the transition between soft and hard state, Type C QPOs are observed during the hard and intermediate state and can largely varies in frequency (Belloni & Motta, 2016). Moreover, there are evidence that Type B QPOs are connected to relativistic ejections (Fender et al., 2009).
Through the proprieties of the fast timing variability, it is possible to define the thresholds of fractional root mean squared (*rms*) that determines the passage between spectral states. A very large variability with typical fractional *rms* that can be as high as 30% (see, e.g., Belloni & Motta 2016) has been observed in HS, while the SS is characterised by low variability levels ($rms < 5\%$) in addition to occasional weak and broad type-A QPOs detected at low frequencies (6–8 Hz).
Based on the fractional *rms* and the different QPOs it is possible to clearly distinguish the IMS located on the HID horizontal-branches in two spectral states: hard intermediate and soft intermediate states (HIMS and SIMS, respectively; Belloni & Motta, 2016). During the HIMS, the fractional *rms* is observed to decrease from ∼30% to 10% and correlates with the hardness (Muñoz-Darias et al., 2011). Furthermore, type-C QPOs with a strong ($rms>20\%$), narrow and variable peak at 0.1–15 Hz are observed(Belloni & Motta, 2016).
The most dramatic changes in the power density spectra occur at the transition between the HIMS and the SIMS (Belloni & Motta, 2016). This timing transition is extremely fast, as opposed to the smooth spectral changes usually observed across the HIMS to SIMS transition (Del Santo et al., 2009; Motta et al., 2009).

The fractional *rms* in the SIMS is estimated to be between 7 and 10 per cent (Muñoz-Darias et al., 2011). Then, Type-B QPOs, characterised by *rms* ∼4% and narrow peaks, are identified in a narrow range of frequencies (∼6 Hz or 1–3 Hz; Belloni & Motta, 2016).

2.4.4 Truncated disc model

One of the main open question on BHTs concerns the nature of the spectral transitions observed over the outbursts (see Section 2.4). Esin et al. (1997) proposed one of the first model to explain the various X-ray behaviour of BHBs based on the transit from an inner hot flow or ADAF to a standard accretion disc (Shakura & Sunyaev, 1973). In addition to the inadequacy of the ADAF solution to explain the parameters observed in the hard state (see Section 2.3), the model was not able to explain the observed hysteresis phenomena (see Section 2.4.2).

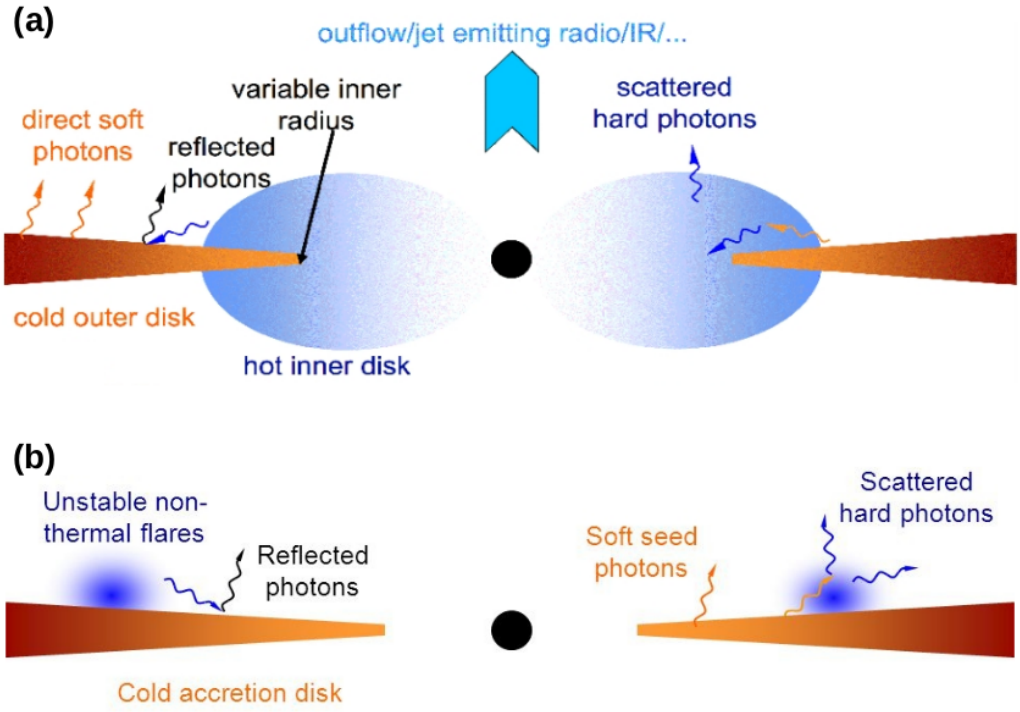

Figure 2.11: A schematic representation of the BHB geometry in the main spectral states taken from Zdziarski & Gierliński (2004). The picture (a) shows a BHB in HS. It consists of a hot inner accretion flow surrounded by optically-thick accretion disc. The disc is truncated far away from the ISCO. (b) The geometry in the SS consists in an optically-thick accretion disk extending close to the BH. The corona region (non-thermal electrons) is located above the accretion disk.

Actually, the most accredited model is the *Truncated disc model*. It explains the different spectral states in terms of changes in the geometry of the accretion flow onto the central object (Zdziarski, 2000; Done et al., 2007).
In this framework, the disc in the HS is truncated at large radii (roughly 100 R_g)

from the BH (Done et al., 2007), therefore the blackbody emission is weaker than in the SS. A hot flow surrounds the BH and overlaps the inner part of the accretion disc. The hot flow Comptonises the soft disc photons, producing the dominant hard X-ray component observed in the HS spectra. However, if the disc is truncated at large distance form the BH, only a small fraction of the photon flux from the outer disc is received in the central parts of the hot flow. Then, the synchrotron photons internally generated in the hot flow may become the dominant source of seed photons for the Comptonisation process (Malzac & Belmont, 2009). In this configuration the outer region of the disc is only partially illuminated by the hot flow and the reflection component and the reprocessing features are weak in this spectral state (see top Figure 2.11, Done et al., 2007; Zdziarski & Gierliński, 2004; Malzac, 2016).
The soft X-ray emission observed is likely associated to the Shakura-Sunyaev disc. The location transition radius between the standard disc and the hot flow evolves during the outburst. It is located at the ISCO in the soft state (bottom Figure 2.11). The spectral fits of the disc component of several BHTs in SS showed that their luminosity vary as $L \propto T^4$ (Done et al., 2007) consistently with the blackbody emission from a constant surface. Furthermore, since the ISCO radius and the BH spin are strictly connected, measurements of the ISCO may offer the opportunity to constrain the BH spin even though knowledge on the source distance and inclination, in addition to an appropriate treatment of the relativistic effects have to be taken into account (Malzac, 2016). The second component observed in SS, the weak high energy tail, is usually interpreted as due to non-thermal Comptonisation in magnetically powered active coronal regions above and below the accretion disc, although its origin is still debated (Poutanen & Coppi, 1998; Laurent & Titarchuk, 1999; Niedźwiecki & Zdziarski, 2006).

Chapter 3

Jet physics

The research performed in the last decades on the jets of BHTs has shown that, even though their radiative emission is weak, these collimated outflows represent an important energy output of the system. In some cases, the jet could carry away a large fraction of the accretion power (see e.g. Fender et al., 2006). This is also important for the impact of the accreting black holes on their environment. Nevertheless, the processes leading to jet formation (acceleration and collimation) and launching mechanism are still not completely understood.
This chapter aims to introduce the physical processes responsible for the jet emission. In the following Sections I provide an overview on our actual knowledge of the jet/accretion coupling and the radio/X-ray connection. Then, I introduce the internal shock emission model (ISHEM) that I have used in the analysis as described in Chapter 6 to model the jet emission of GRS 1716–249.

3.1 Accretion/ejection coupling

One of the current research areas on X-ray binaries focuses on the relation between accretion flow and jets. In addition to the X/γ-ray phenomenology (see Section 2.4), the BHTs spectral states are also characterised by the production of different outflows (Mirabel, 1994; Fender et al., 2006). The observation of non-thermal emission in the radio band is the primary signature of the presence of jets. These are collimated outflows of matter whose emission can extend over the whole electromagnetic spectrum: from radio to γ-ray energy bands. Since the discovery of the superluminal ejecta (Mirabel, 1994) it has become clear that collimated outflows can be produced in stellar environments when an accretion disc is present. Further proof about the accretion/ejection coupling were reported by Mirabel et al. (1998). Indeed, the authors observed simultaneous infrared and radio flares associated to dips in the X-ray spectrum of GRS 1915+105. This contributed to initiate the multi-wavelength studies of XRBs with the aim to understand the accretion/ejection connection.

The unification scheme introduced by Fender et al. (2004) provides a useful way to characterise the phenomenology of the X-ray spectral states and radio jets. This can be easily illustrated through an HID (see Figure 3.1). As explained in

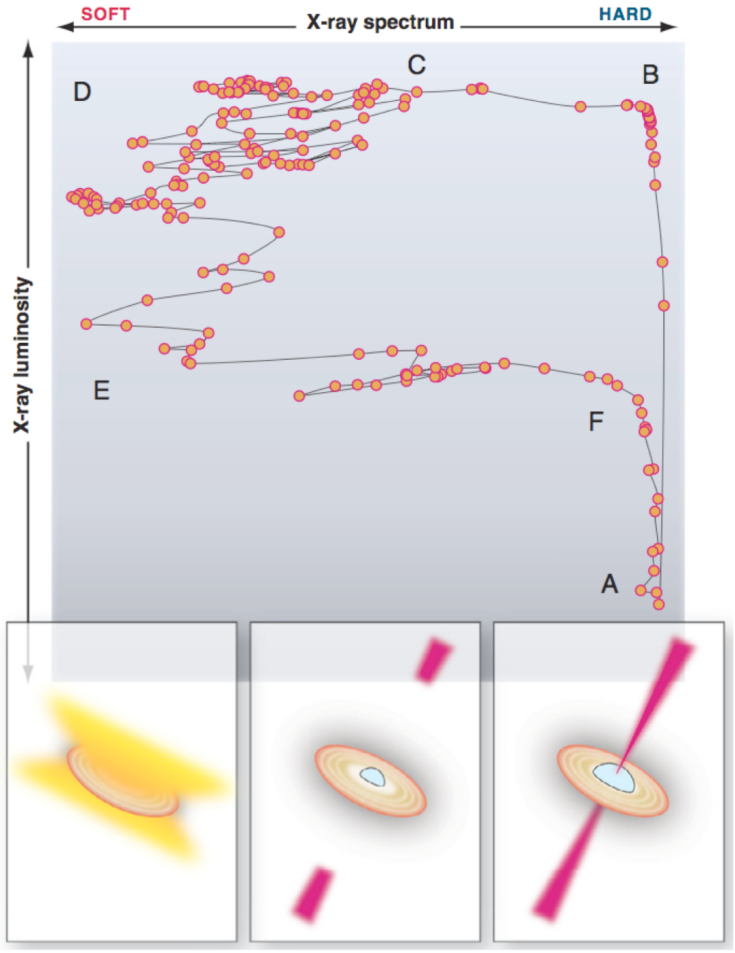

Figure 3.1: A schematic qualitative representation of the jet-disc coupling in BHTs. The figure is taken from Fender & Gallo (2014).

Section 2.4.2, such diagram shows the evolution of the source's X-ray luminosity as a function of the hardness ratio during the outburst. The X-ray emission of BHTs in hard state is generally associated with radio *compact* jets. These are characterised by a flat (spectral index $\alpha \sim 0$, where $\alpha = \frac{d \log S_\nu}{d \log \nu}$ and S_ν is the flux density at a frequency ν) or slightly-inverted ($\alpha \geq 0$) radio spectrum (e.g Fender et al. 2001; Corbel & Fender 2002; Fender et al. 2004). This is interpreted as self-absorbed synchrotron emission from steady jets (Blandford & Königl, 1979, see Section 3.2).
This scenario was initially speculated owing to the analogy with the observations of low-luminosity AGNs and then confirmed by the observation of the resolved jets of Cyg X–1 (Stirling et al., 2001) and GRS 1915+105 (Mirabel, 1994, see Figure 3.2). These steady jets persist along the IMS branch despite the softening of the X-ray spectrum (from point B to point C in Figure 3.1). Bright radio flares are observed and radio knots - which move from the site where the BH is located - are spatially resolved when the transition from HIMS to SIMS occurs (a few percent of L_{Edd}). The radio flares are believed to be associated with the inner disc radius moving closer to the BH (Fender et al., 2004). It was suggested that before

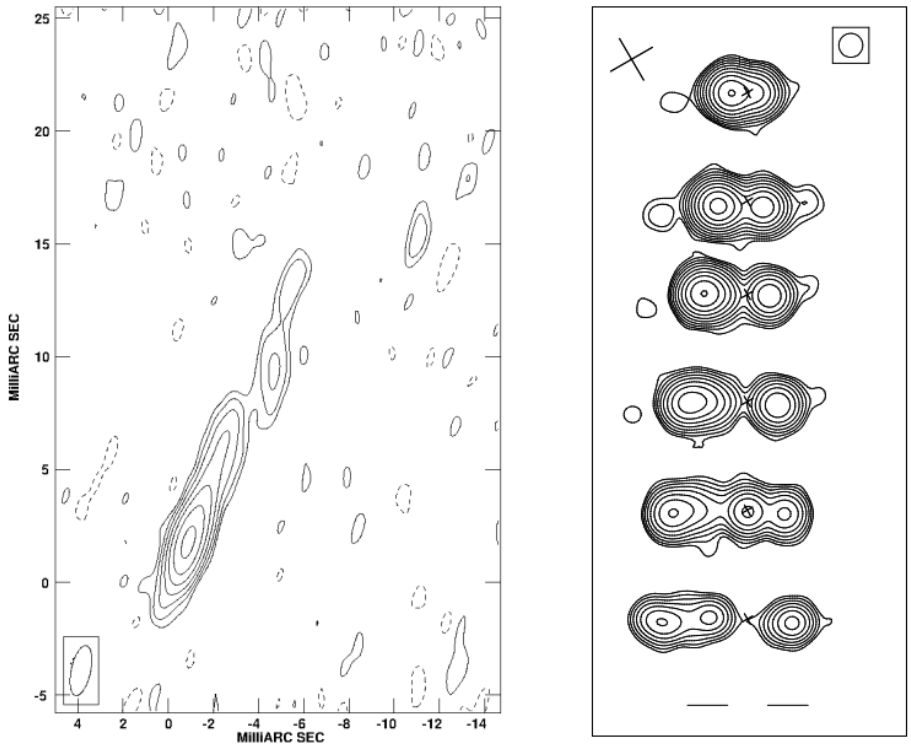

Figure 3.2: *Left:* High resolution VLBA image at 8.4 GHz of Cyg X–1 radio jet (Stirling et al., 2001). *Right:* tansient, arcsec-scale radio jets (VLA at λ3.5-cm) from GRS 1915+105 (Mirabel, 1994).

the jet is suppressed in the soft state, as the X-ray spectrum begins to soften and the inner disc radius supposedly moves inward, the jet velocity increases sharply. This rapid increase of Γ results in powerful, optically thin, internal shocks that propagate along the outflow and possibly disrupt it (Fender et al., 2004, 2009). Nevertheless, what drives the variation in the radio properties after the hard X-ray peak is still an open question. In GX 339–4, XTE J1550–564 and GRS 1915+105 it has been observed that the radio spectral index changes from flat to inverted to optically thin during the spectral transition. This suggests that there are some physical changes in the jet connected with the softening of the X-ray spectrum (Gallo, 2010).
After the hard to soft transition, the emission from radio to near-IR drops (D to E in Figure 3.1), although radio emitting plasma with relativistic speed is often observed to move hundreds of A.U. (Gallo, 2010). Finally, jets are not detected in soft states: the drop of the radio emission is usually ascribable to the quenching of the jets (Fender et al., 1999; Corbel et al., 2000), but it has also been suggested that the drop of the radio/IR emission may be related to the low X-ray variability in the soft spectral states (Drappeau et al., 2017).

3.1.1 The connection between radio and X-ray emission

A strong and tight radio/X-ray correlation has been first observed in hard state of GX 339–4 (Corbel et al., 2000, 2003) and subsequently in a number of HS BHTs (see Figure 3.3). It takes the form of a non-linear flux correlation, i.e.

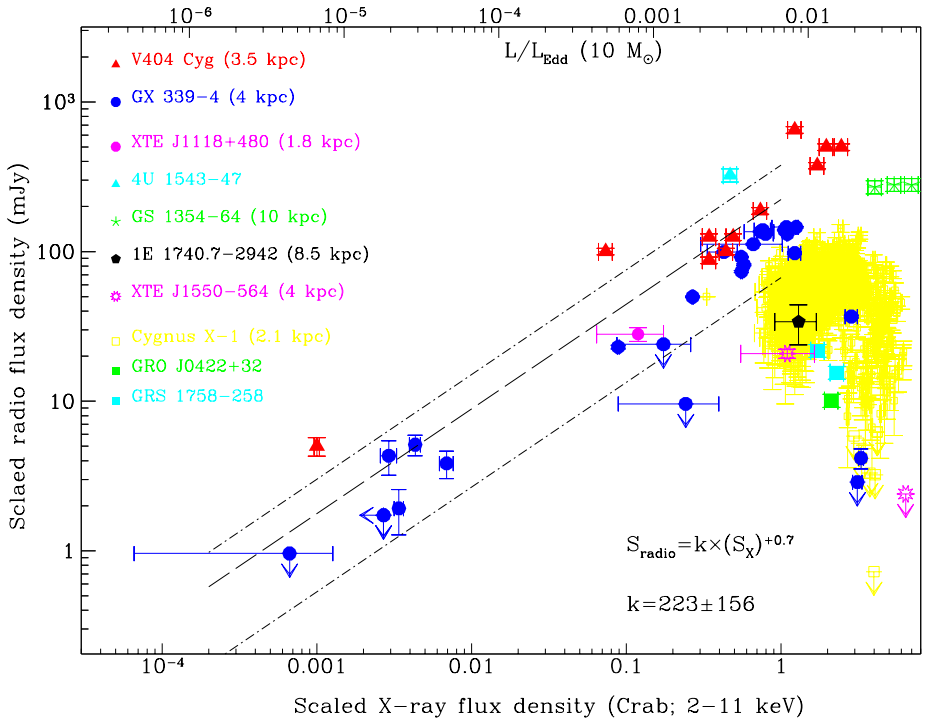

Figure 3.3: Radio flux density (mJy) versus the X-ray flux density (Crab) for a sample of ten hard state BHs (Gallo et al., 2003).

$F_R \propto F_X^a$, where a ∼0.5-0.7, and F_R and F_X are the radio and X-ray fluxes, respectively (Gallo et al., 2003). The correlation extends over more than three orders of magnitude in L_x and breaks down around 2% L_{Edd} (even though GX 339–4 was observed in hard state with correlated X-ray and radio flux up to 30% L_{Edd}). Then, the sources enter the SS and the radio emission is no longer detectable (Gallo et al., 2003; Gallo, 2010).
In recent years, several BHTs have been observed to be underluminous in the radio band with respect to the standard radio/X-ray correlation. Indeed, these sources follow a different correlation with a steeper index, i.e. ∼1.4 on the radio/X-ray luminosity plane (Coriat et al., 2011; Corbel et al., 2013). The sources on this branch are called "outliers", although their increasing number could turn out to be the norm (Coriat et al., 2011; Motta et al., 2018). We also refer to them as radio-quiet since their radio emission can be 1-2 magnitudes lower around L_X ∼10^{36-37} erg s^{-1}.
Although several hypotheses have been proposed to explain the origin of such correlations, no unique theory is able to explain their origin yet. The different indexes of the correlations ($a \sim 0.7$ and $a \sim 1.4$ for radio loud and radio-quiet

BHTs, respectively) could be due to a different radiative efficiency of the accretion flow. Indeed, Coriat et al. (2011) suggested that the radio/X-ray correlation of the "outliers" ($L_R \propto L_X^{1.4}$) is produced by a radiatively efficient accretion flow $L_X \propto \dot{M}$. While, the radio-loud branch ($L_R \propto L_X^{0.6}$) would result from inefficient accretion where $L_X \propto \dot{M}^{2-3}$.
Recently, this picture has been challenged by the finding that radio-quiet BHTs tend to have a negative spectral index α ($S_\nu \propto \nu^\alpha$) while for the radio-loud sources a positive α is observed. This suggests different jet core properties (rather than accretion flow) for the two classes of sources (Espinasse & Fender, 2018).

3.1.2 Jet emission in Infrared

Similarly to the radio, the infrared emission correlates with the X-ray emission with a slope of about 0.6 (Russell et al., 2006). This emission is suppressed in SS as well (Russell et al., 2006). The spectral break corresponding to the transition from partially absorbed optically thick (at low frequencies) to optically thin (at higher frequencies) synchrotron emission from jets, as predicted by the Blandford & Koenigl model (see Section 3.2), was first derived by Fender et al. (2001); Corbel & Fender (2002). Then, in 2011 this break was directly observed in the mid-IR by Gandhi et al. (2011).
Identifying the spectral break (as well as the cooling break) may place useful constraints on the total power of the jet and mark the position along the jet where the particles are accelerated. However, due to the dominant IR emission from the accretion disc and/or companion star, the spectral break has been identified only in a few sources (see e.g. Rahoui et al., 2011; Russell et al., 2013a). During the HIMS-to-HS transition of MAXI J1836–194 occurred before the source quiescence, it was observed that the spectral break shifted towards higher frequencies simultaneously with a source hardening (Russell et al., 2013b, 2014; Péault et al., 2019).

3.2 Standard model

As mentioned earlier, jets are collimated outflows of matter which can move at relativistic velocities. Their geometry depends on the behaviour of the internal and external pressure due to the interstellar medium, in addition to plasma characteristics at launch.
The standard model for steady jet introduced by Blandford & Königl (1979), assumes that this relativistic outflow is launched perpendicularly to the plane of the accretion disc and starts to be visible at a distance z_0 from the black hole. Beyond this point, the flow is confined to a truncated cone of constant opening half-angle ϕ and the jet axis makes an angle ϑ with the line of sight of the observer. Besides, this outflow has an assumed uniform velocity $\beta_j = v/c$, corresponding to a Lorentz factor $\Gamma_j = (1 - \beta_j)^{-1/2}$.
If we consider a freely expanding conical jet, the radius grows as:

$$r(z) = r_0 \left(\frac{z}{z_0} \right) \tag{3.1}$$

The standard model, then, assumes that the magnetic field is oriented perpendicularly to the jet axis and frozen into the plasma. If the magnetic field originated in the accretion disc drives the outflow, we expect that the magnetic field decreases as the jet expand. In fact, the magnetic field conservation implies

$$B \propto r^{-1} \Longrightarrow B(z) = B_0 \left(\frac{z_0}{z}\right) \tag{3.2}$$

where B_0 is the magnetic field intensity at the base of the jet.

3.2.1 Spectrum emission

The presence of synchrotron emission is an important feature of astrophysical observations as it implies the presence of acceleration processes in the sources. The basic ingredients to produce this emission are energetic electrons and a magnetic field.
It is generally recognised that the main emission mechanism responsible for the emission observed from radio to IR frequencies in the jets is synchrotron radiation (Inverse Compton radiation dominates at γ-rays energies). Nevertheless, there are still uncertainties in our knowledge about the location of the dominant energy dissipation, where the particles are accelerated and the particle acceleration mechanism. This has led to formulating various jet models which consider different factors such as the injection of relativistic particles, the origin of the magnetic field, the properties of the region where the radiation is produced, how to treat the transport of particles, the physical interactions involved in the production of the radiation, the acceleration process.
The most accepted mechanism to accelerate the electrons is shock acceleration, although alternative models have been considered, e.g., magnetic reconnection where the topology of the magnetic field lines changes and the magnetic energy is converted to kinetic energy which is used to accelerate the electrons (see e.g Lyubarsky, 2010).
It is possible to show that the relativistic electrons accelerated through shocks (see e.g. Longair, 2011) have their energies distributed as a power law with index p:

$$N(\gamma) = k\gamma^{-p} = N(E)\frac{dE}{d\gamma} \tag{3.3}$$

where k is the distribution normalisation and $E = \gamma m_e c^2$ is the energy of the electrons. The Lorentz factor γ is associated with the movement of the electrons. The distribution 3.3 extends from the minimum (γ_{min}) to the maximum (γ_{max}) energies of the electron population. Outside these bounds, it is assumed that the distribution drops exponentially. The value of p depends on the acceleration mechanism considered. In the case of particles accelerated through shocks, the theory shows that the index can assume values $p \sim$2-2.5 (Jones & Ellison, 1991).
As for all the emission processes, the synchrotron radiation is also accompanied by absorption. The specific intensity is expressed as:

$$I_\nu = \frac{J_\nu}{4\pi\mu_\nu}[1 - e^{-\mu_\nu r(z)}] \tag{3.4}$$

where J_ν is the emission profile given the assumed power-law energy distribution of electrons, and μ_ν is the absorption coefficient (Lightman & Zdziarski, 1987; Longair, 2011). The flux density is proportional to I_ν for a source subtending a

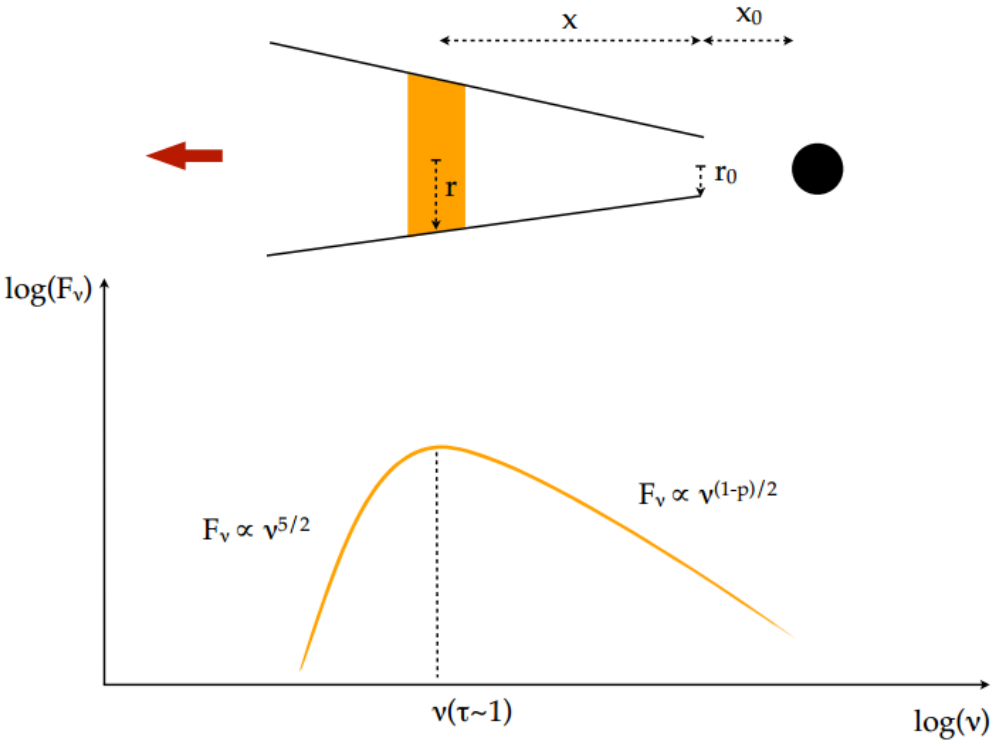

Figure 3.4: Spectrum of a compact jet segment.

given solid angle. Therefore, the synchrotron flux of a jet segment at an observed frequency ν is (Longair, 2011):

$$F_\nu \propto \frac{J_\nu}{\mu_\nu}[1 - e^{-\tau(\nu)}] \tag{3.5}$$

where $\tau(\nu) = \mu_\nu r(z)$ is the optical depth.
It is possible to recognise two regimes in the spectrum: absorbed/optically thick and optically thin. The peak is at a specific frequency ν_t corresponding to $\tau = 1$ (see Figure 3.4). Below ν_t the plasma is optically thick ($\tau >> 1$) and a significant fraction of the synchrotron photons is absorbed by interactions with the same emitting electrons (Synchrotron Self-Absorption, SSA). At low frequencies the flux drops as $F_\nu \propto B^{-\frac{1}{2}}\nu^{\frac{5}{2}}$. While, above ν_b the spectrum follows the optically thin case: $F_\nu \propto B^{\frac{p+1}{2}}\nu^{\frac{1-p}{2}}$. It is worth noticing that the spectrum of optically thin synchrotron radiation from a power-law distribution N(E) is also a power law where the index is $\alpha = (p-1)/2$.
The peak of the emission (corresponding to $\tau \simeq 1$) gradually shifts to low frequencies, as the emitting gas travels along the jet axis and expands (see Figure 3.5). The result is a superimposition of several peaked synchrotron spectra generated

by different regions along the outflow where the emission at a given frequency is a mixture of optically thick and thin emission from different regions of the jets. Assuming that the magnetic field scales as r^{-1} (see Eq. 3.2) and $k \propto r^{-2}$, it turns out that this combined partially absorbed emission is independent by the photon frequency and the resulting spectrum is flat (see Figure 3.5). This component is

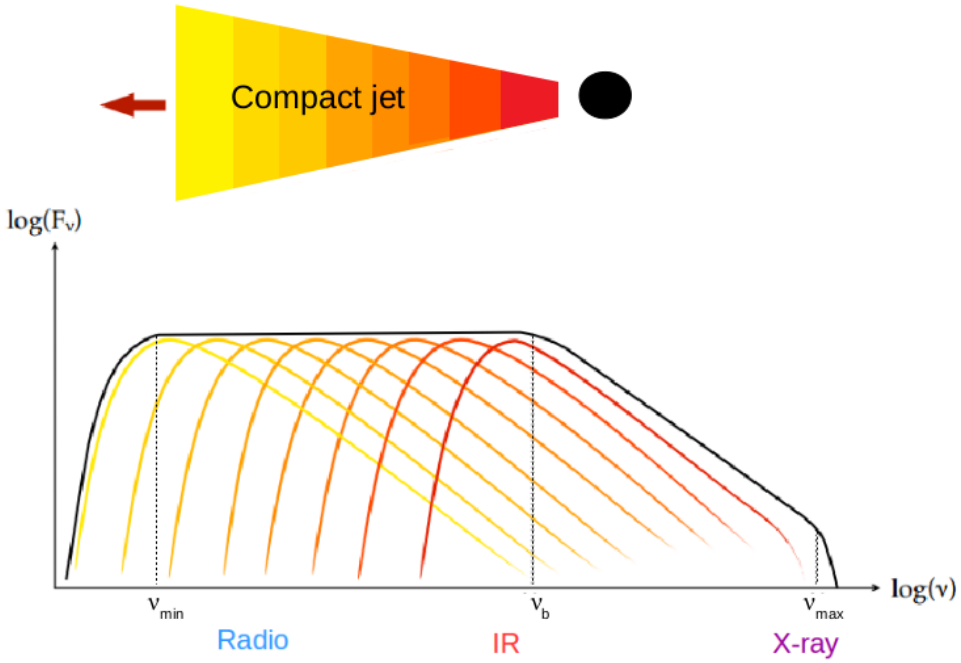

Figure 3.5: Schematic representation of the emission spectrum of a compact jet according to the standard model.

bounded by two characteristic cut-off frequencies: ν_{min} and ν_b. At low frequencies the flat spectrum extends to the frequency ν_{min} for which $\tau(\nu_{min}) \sim 1$. ν_{min} corresponds to the farthest region of the jet containing relativistic electrons. For frequencies $\nu < \nu_{min}$, we find the dependence $F_\nu \propto B^{-\frac{1}{2}}\nu^{\frac{5}{2}}$ of the SSA emission. The emitting electrons are accelerated at a distance from the black hole corresponding to ν_b, for which $\tau(\nu_b) \sim 1$. This frequency corresponds to the base of the jet emitting region, while ν_{min} corresponds to the end of the large scale 'top' of the jet emitting region. There is then another characteristic frequency in the spectrum which corresponds to the emission of the most energetic electrons in the distribution. From the expression of the critical frequency at which a single electron of energy γ emits, it is possible to estimate a maximum frequency

$$\nu_{max} = \frac{3\gamma_{max}^2 eB}{4\pi m_e c} \tag{3.6}$$

beyond which the total flow density decreases exponentially.

3.2.2 Internal shock emission model

It has been shown that assuming continuous re-acceleration of the electrons along the jet allows to reproduce the flat radio spectrum usually observed (Blandford & Königl, 1979). A dissipation mechanism compensating for the cooling caused by adiabatic expansion is required to maintain the flat spectral shape, otherwise we would observe a strongly inverted radio spectrum due to the dimming of synchrotron emission as the outflow expands (Marscher, 1980). The most invoked mechanism to compensate these losses is based on the continuous energy input by internal shocks (Kaiser et al., 2000).
The internal shock models are based on the discretisation of the jet into homogeneous ejecta which are injected at the base of the jet with variable velocities. The interactions between faster and slower ejecta lead to shocks in which the kinetic energy is converted into internal energy and, ultimately, synchrotron radiation. Malzac (2013, 2014) showed that internal shocks caused by fast fluctuations of the jet velocity can be an effective dissipation mechanism along the jets. The origin of the fluctuations is likely driven by the variability of the accretion flow.
The internal shock emission model (ISHEM), proposed by Malzac (2014), simulates the hierarchical merging of shells of plasma ejected at the base of the jet with variable velocities and at uniform time-intervals comparable to the dynamical time-scale of the inner accretion flow. The fluctuation of the shells' Lorentz factor Γ_{av} in the jet is defined assuming that its power spectrum has the same shape and amplitude of variability of the PDS observed in X-rays. The ISHEM model takes as input a number of parameters related to three families:

- **the source**. Its properties are defined by the distance (D), the system inclination with respect to the line of sight (ϑ) and the mass of the black hole ($M_{\rm BH}$);
- **the jet**. In addition to the jet half-opening angle ϕ and the jet power ($P_{\rm jet}$), this group includes also the parameters necessary to define the launch of the shells such as the radius of the base of the jet (R_c), the mass of the shells, the volume filling factor and the average Lorentz factor (Γ_{av});
- **the particles**. This group introduces the parameters that describe the distribution of the radiating particles. The electrons responsible for the synchrotron emission follow a power-law energy distribution extended from γ_{min} to γ_{max} with index p.

Malzac (2013) shows that the distribution of the velocity fluctuation amplitudes over their time-scales (described by the PSD), determines how much kinetic energy of the ejecta is converted into internal energy and where it is deposited. Therefore, given a set of parameters that describe the source, its jet and the particles and the X-ray PDS, which determines the temporal evolution of the Lorentz factor of each shell injected at the base of the jet, the ISHEM model computes a synthetic Spectral Energy Distribution (SED). It turns out that the shape of the SED is determined mainly by the power spectrum of the Lorentz factor fluctuations. The only other parameter that has an effect on the SED shape is the slope

p of the power law energy distribution. Indeed, p affects the slope of the optically thin synchrotron emission at frequencies above the jet spectral break. In particular, the p parameter controls the jet luminosity around 1 MeV and determines whether the jet is responsible for the observed high energy excess (see Chapter 6). The effect of the other parameters is to change the flux normalisation or shift the SED along the frequency axis without altering the SED profile. It is possible to show that for a BHB the flux normalisation scales as:

$$F_\nu \propto \frac{\delta^2 i_\gamma^{\frac{5}{p+4}}}{D^2 \tan\phi} \left(\frac{P_{jet}}{(\Gamma_{av}+1)\Gamma_{av}\beta} \right)^{\frac{2p+13}{2p+8}} \tag{3.7}$$

and the break frequency (Malzac, 2013) as:

$$\nu_b \propto \frac{\delta i_\gamma^{\frac{2}{p+4}}}{\tan\phi} \left(\frac{P_{jet}^{\frac{p+6}{2p+8}}}{(\Gamma_{av}+1)\Gamma_{av}\beta} \right)^{\frac{3p+14}{2p+8}} \tag{3.8}$$

where $i_\gamma = (2-p)(\gamma_{max}^{2-p} - \gamma_{min}^{2-p})^{-1}$ and D is the source distance. A detailed study about the effects of the different parameters was presented by Péault et al. (2019). It is worth noticing that if the synthetic SED shape does not fit the data there is no way to fine tune these parameters in order to match the data. On the other hand, if the predicted shape of the SED is similar to the observed SED, it is difficult to constrain the model parameters, as there is a strong degeneracy that makes it possible to reproduce the observed SED with many different parameters combinations.

Chapter 4

Instruments and methods

Then, I describe the main steps of the *Swift*/XRT, BAT and *INTEGRAL*/SPI data reduction I have performed to extract the X/γ-rays spectra of GRS 1716–249 during its 2016-2017 outburst. Sampling the emission of these objects in the widest energy range possible gives an unique opportunity to understand the behaviour of the various emitting components, and therefore of the physical processes which are taking place. For this purpose it is important to coordinate a number of facilities in a very short time.
In this Chapter I present the technical characteristics of the telescopes that have been used for obtaining data in the radio, optical, near-infrared, X-ray and soft γ-ray energy bands for my research. For radio and infrared instruments I only describe the main instrumental characteristics since collaborators to the project have performed the data reductions. Then, I describe the main steps of the *Swift*/XRT, BAT and *INTEGRAL*/SPI data reduction I have performed to extract the X/γ-rays spectra of GRS 1716–249 during its 2016-2017 outburst.

4.1 Radio instruments

4.1.1 Australian Telescope Compact Array (ATCA)

Figure 4.1: Five antennas of the Australia Telescope Compact Array.

The Australian Telescope Compact Array[1] (ATCA, Figure 4.1) is an earth-rotation aperture synthesis radio interferometer. It is located at the Paul Wild Observatory in Australia. It is composed of six antennas of 22 m diameter aligned east–west. The position of the five antennas can be moved along a 3 km long east–west track and a 214 m long north-south track, while the sixth one is fixed in position at 3 km to the west of the main track. The array can be used to observe in five wavelength bands between 27 cm–3 mm (frequencies of approximately 1.1–105 GHz).
The main observational properties of ATCA are summarised in Table 4.1.

Band Name	16 cm	4 cm	15 mm	7 mm	3 mm
Band Code	L / S	C / X	K	Q	W
Frequency Range (GHz)	1.1–3.1	3.9–11.0	16–25	30–50	83–105
Primary beam	42′–15′	12′–4′	2′	70″	30″
System temperature (K)	45	36	60	112	724
System sensitivity (Jy)	55	43	72	136	1051
Synthesized beam	9”–3”	3”–1”	0.5”	0.2”	2”
Flux sensitivity (mJy/beam) (10 min)	0.04	0.03	0.05	0.09	0.70
Flux sensitivity (μJy/beam) (12 hr)	4	3	5	33	83

Table 4.1: Frequencies at which the ATCA operates and telescope properties. The vales reported in the tables are from https://www.narrabri.atnf.csiro.au/observing/users_guide/html/chunked/ch01s02.html.

4.1.2 Very Large Arrey (VLA)

Figure 4.2: Very Large Array.

The Very Large Array[2] [3] (VLA, see Figure 4.2) is located on the Plains of San Agustin in south-western New Mexico (USA). It consists of 27 parabolic

[1] http://www.narrabri.atnf.csiro.au/
[2] https://science.nrao.edu
[3] http://www.vla.nrao.edu/

antennas of 25 m diameter positioned in a Y-shaped configuration and it performs observations with the aperture synthesis technique.
The telescope covers a wide range of frequencies from 54 MHz to 50 GHz. The VLA can vary its resolution through the movement of the antennas: it can reach a maximum resolution of 1.4 arcseconds at 1.4 GHz and of 40 milliarcseconds at 50 GHz. It is possible to observe in two frequency bands simultaneously only if these frequencies are separated by more than ∼450 MHz.
The VLA can map large-scale structure of gas and molecular clouds in addition to the ejections of plasma from black holes. The main characteristics of VLA are reported in Table 4.2.

	4 Band	P Band	L Band	C Band	X Band	U Band	K Band	Q Band
Frequency (GHz)	0.073–0.0745	0.30–0.34	1.34–1.73	4.5–5.0	8.0–8.8	14.4–15.4	22–24	40–50
Wavelength (cm)	400	90	20	6	3.6	2	1.3	0.7
Primary beam (arcmin)	600	150	30	9	5.4	3	2	1
Highest resolution (arcsec)	24.0	6.0	1.4	0.4	0.24	0.14	0.08	0.05
System Temp (K)	1000-10,000	150-180	37-75	44	34	110	50–190	90–140

Table 4.2: VLA frequencies and telescope properties.

4.1.3 Long Baseline Array (LBA)

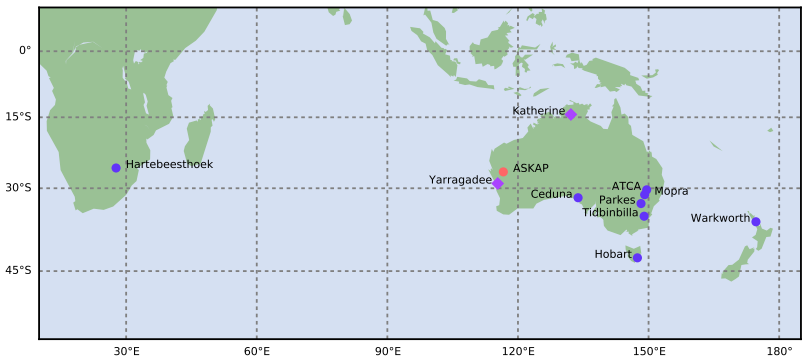

Figure 4.3: Map showing the positions of all telescopes available within the LBA network. http://www.atnf.csiro.au

The Long Baseline Array[4] (LBA) is part of the Very Long Baseline Interferometry[5] (VLBI) array which can observe regularly the entire southern sky. It

[4] https://www.atnf.csiro.au
https://ned.ipac.caltech.edu

[5] It involves a network of radio telescopes in Australia and overseas. It is carried out by observing at various telescopes in the network relatively independently of each other.

consists of the Australia Telescope National Facility's Parkes 64 m telescope, Mopra 22 m telescope, and the ATCA, in addition to the University of Tasmania's Hobart 26 m and Ceduna 30 m telescopes located along the east coast of Australia (see Figure 4.3). The telescopes extension in a north-south direction limits the (u, v) coverage.
LBA can operate in the frequency bands at 1.4, 1.6, 2.3, 4.8, 6.7, 8.4 and 22 GHz, although not all bands are supported by all telescopes. The array has been designed to actively suppress signals above 80 MHz.

4.2 Infrared/Optical instruments

4.2.1 Rapid Eye Mount (REM)

The Rapid Eye Mount[6] (REM, Antonelli et al., 2003) is a fully robotic fast-slewing telescope located at ESO-La Silla Observatory in Chile. It has been achieved in the framework of the Fast Robotic Observatory System for Transient (FROST). It is a Ritchey-Cretien 60 cm rapid-reaction automatic telescope with a focal ratio f/8.
The telescope has been mainly designed to follow the afterglows of γ-ray bursts (GRBs) detected by the *Neil Gehrels Swift Observatory*, *INTEGRAL*, *AGILE* and others. The accurate fast pointing (10 deg) makes REM suitable for immediate response to random alerts (typically it points a source within 30 seconds). In particular, it is very useful to perform the multi-wavelength monitoring of highly variable and transient sources (i.e.: flaring stars, AGN or galactic black holes).
The telescope hosts two instruments that can observe simultaneously:

- The **REM Infrared imaging camera** (REMIR, Vitali et al., 2003) performs high efficiency imaging. It covers 0.95-2.3 μm range with high performance near-IR filters: J, H and K. The instrument is characterised by a field of view (FoV) of about $10' \times 10'$ and a 512-pixel camera with pixel scale of $1.1''$/pix.
- The **REM Optical Slitless Spectrograph** (ROSS, Palazzi et al., 2002). It has almost the same FoV of the REMIR camera. It is equipped with the g', r', i', z' filters and it operates in the 0.45–0.95 μm energy band.

[6] http://www.rem.inaf.it

4.3 High energy instruments

4.3.1 Neil Gehrels Swift Observatory

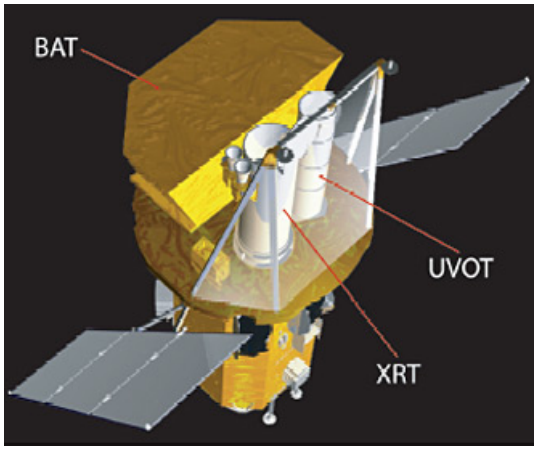

Figure 4.4: The *Swift* spacecraft showing the three instruments on-board: Burst Alert Telescope, X-ray Telescope and UV/Optical Telescope.
Figure from https://www.nasa.gov/mission_pages/swift/spacecraft/index.html.

The *Neil Gehrels Swift Observatory*[7] [8] (hereafter *Swift*) is a NASA Medium Explorer mission developed in collaboration with UK and Italy. It is a multi-wavelength observatory (from optical to γ-ray energy bands) designed with the main aim to study GRBs. Nevertheless, the capabilities of the different instruments on board of *Swift* make it suitable to observe other types of transient sources.
The satellite is orbiting in a low earth circular orbit at an altitude of about 600 km, and a maximum inclination of 22°. It was launched in 2004 November. The *Swift* rapid reaction provides a unique ability to respond in short times with sensitive γ-ray, X-ray, ultraviolet, and optical observations to most events on the sky. Furthermore, it can determine the sources' position with arcsecond accuracy. For these reasons the observatory is frequently used for Target of Opportunity (ToO) observations of X-ray transients, pulsar glitches, outbursts from X-ray binaries and stellar flares.
The satellite carries three co-aligned instruments (Figure 4.4): the Burst Alert Telescope (BAT), the X-Ray Telescope (XRT) and the UV-Optical Telescope (UVOT). BAT is the primary instrument. It is characterised by a large FoV, while XRT and UVOT are high precision focusing instruments. In the following a brief description of the three telescopes:

Burst Alert Telescope (BAT, Barthelmy et al., 2005) is a highly sensitive coded mask instrument. It consists of a mask made of opaque and transparent elements placed on top of the telescope. The X/γ-rays coming from

[7] https://swift.gsfc.nasa.gov
[8] https://www.swift.psu.edu

the observed source project the shadow of the mask onto the detector plane producing the so called *shadowgram*. This is analysed to create an image of the sky in the FoV by finding the position and intensity of the different sources in the FoV. The high energy photons from distant objects are rare and given their penetrating power they cannot be focused by mirrors. The coded aperture imaging technique was developed to observe hard X/γ-ray sources and weak fluxes with respect to the background counting rate. For more detail on coded masks properties I refer to Caroli et al. (1987).
BAT instrument can observe daily up to 80% of the whole sky in survey mode in the 15–150 keV band. Its wide FoV (1.4 sr) is particularly suitable to identify the hard X-rays sources and determining their location on the sky to within $1'$–$4'$ accuracy. Its Point Spread Function (PSF) is of $17'$ and the energy resolution is about 7 keV.
The telescope works in two distinct operating modes: *Scan-Survey mode* and *Burst mode*. BAT spends most of the time in Scan-Survey mode. It performs an all-sky hard X-ray survey, with a sensitivity of $\sim$1 mCrab[9] in the energy range 15–150 keV, waiting for a burst occurring in the FoV. This allows the instrument to be a monitor for hard X-ray transients when GRBs are not observed. As soon as a GRB is revealed, the telescope switches into the Burst mode to identify and define its position.

X-ray Telescope (XRT, Burrows et al., 2005) is an imaging spectrometer designed to make prompt observations of GRBs and transient sources measuring fluxes, spectra, and lightcurves in 0.2–10 keV energy range.
The soft X-ray photons are focused through a grazing incidence Wolter I telescope (3.5 m focal length) onto a CCD. It is characterised by an effective area of 110 cm^2 , a FoV of 23.6×23.6 arcmin and a PSF of $18''$ HPD (Half Power Diameter) at 1.5 keV. Then, the Full Width at Half Maximum (FWHM) energy resolution is about 260 eV at 5.9 keV.
XRT is characterised by a rapid and accurate position determination, i.e. it can localise a point source with $\sim 3''$ accuracy. Then, high time resolution light curves and spectrum with moderate resolution can be produced selecting the different operative modes in which XRT can operate. The telescope can work in four different operative modes[10]: *Imaging mode* (IM), *Windowed Timing mode* (WT) and *Photon Counting mode* (PC). The fourth operative mode *Photodiode mode* (PD) was disabled on May 2005 for technical issues (see Section 4.3.2.2).
The observations of GRS 1716–249 - I analyse in this thesis - have been performed using XRT in WT mode.
The WT mode is optimal for timing studies thanks to its high time resolution ($\sim$1.8 ms). Furthermore, it is ideal to perform spectroscopy of bright sources (fluxes between 1–600 mCrab). When this operative mode is selected, only 200 columns covering the central $8'$ of the FoV are used and the read out electronics produce only one dimensional imaging informa-

[9] 1 Crab = 2.4×10^{-8} erg cm^{-2} s^{-1} in the energy range 2–10 keV.
[10] http://www.swift.ac.uk/analysis/xrt/files/xrt_swguide_v1_2.pdf

tion. The PC mode is suitable to study the sources when the flux is weak (lower than 1 mCrab): the BHT ending part of the outburst and/or the quiescence. This operative mode retains full imaging and spectroscopic resolution with a limited time resolution (2.5 s). When the source has more than ∼0.6 counts/s the data suffers from pile-up (see Section 4.3.2.2).

UV/Optical Telescope (UVOT, Roming et al., 2005) is co-aligned with XRT and it provides simultaneous optical/ultraviolet observations in the 1650–6000 Å range. UVOT is a 30 cm modified Ritchey-Chrétien telescope with a focal ratio of 12.72.
Its ultraviolet capabilities put together with the absence of atmospheric extinction, diffraction, and background makes UVOT a powerful instrument. The detector is a photon counting CCD, it is able to retain both position and timing information of the incident photons. The FoV is about $17' \times 17'$. The image resolution is about $2.5''$ at 350 nm. It is sensitive to magnitude 22.3 in a 17 minutes exposure. It has seven broadband filters and two grisms (see Table 4.3). The FWHM is of about $2.5''$, although there are small variations in the width of the PSF between the filters.

Filter	λ_c (nm)	FWHM (nm)	Sensitivity (counts)
V	544	75.0	143
B	439	98.0	441
U	345	87.0	217
UW1	251	70.0	99
UM2	217	51.0	53
UW3	188	76.0	87
White	385	260.0	1306

Table 4.3: Characteristics of UVOT filters. The columns reports the filters, the central wavelength and the full width half maximum of each filter. The last column reports the UVOT sensitivity limits for Vega with an exposure of 1000 s.

4.3.2 *Swift* data processing

The raw telemetry data from the instruments and the spacecraft (e.g. events data, housekeeping, attitude) are converted into FITS format by the Swift Data Center (SDC). The *Swift* data are available from the High Energy Astrophysics Science Archive Research Center (HEASARC) public archive[11] and the mirror web sites in Italy[12] and UK[13]. Since it is not guaranteed that the data have been processed using the most recent calibration database (CALDB) or software version, it is usually recommended to reprocess them.

[11] https://heasarc.gsfc.nasa.gov/docs/archive.html
[12] http://www.ssdc.asi.it/mmia/index.php?mission=swiftmastr
[13] https://www.swift.ac.uk/swift_portal/

4.3.2.1 XRT data reduction

To reprocess[14] the XRT observations performed on GRS 1716–249, I used the XRT Data Analysis Software package (XRTDAS) included in the HEASARC software package HEASoft (v.6.20) and the Calibration Database (CALDB; release 20160609).
The first step I did to extract the WT spectra of GRS 1716–249 was to clean and calibrate the data. The process consists of the identification and removal of the bad/hot columns, coordinate transformation, reconstruction of events and the procedures to convert the pulse height to physical units. In this phase the X-rays events are identified and classified to eliminate any events due to charged particles. The charge in a pixel is recognised as an event when it exceeds a defined threshold and it is higher than its neighbouring pixels. For each event the following parameters are recorded: position, time and pulse height of the central pixel, in addition to the pulse heights of the surrounding pixels. In WT mode the charges are distributed in a pixel matrix 7×1. Each event is classified assigning a grade: i.e. a number characterising the pattern of pixels whose charges are higher than a threshold value. This classification is based on the morphology of the local maximum and the analysis of the surrounding neighbouring pixels. An example of the grades considered good in WT mode is shown in Figure 4.5: i.e. a central single-pixel event with a charge higher than the threshold value is assigned a grade of 0.

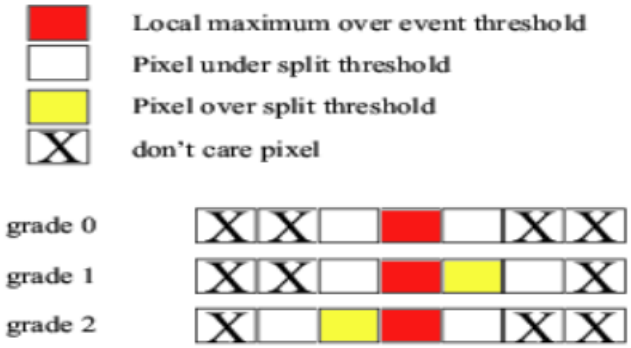

Figure 4.5: Definition of the XRT good grades for WT mode. The figure shows a 7×1 matrix centred on the pixel containing the higher charge (local maximum, red) which is used to define the event grade, the pixels exceeds a defined threshold value (yellow) and the pixels with a charge under the threshold value (white). Figure from Capalbi et al. (2015).

Spectral distortion at low energies ($\lesssim 1.0\,\mathrm{keV}$) can be observed in the spectrum of bright and/or heavily absorbed (columns $\geq 10^{22}\,cm^{-2}$) sources. They are not intrinsic to the source, but are due to charge traps: i.e. imperfections in the structure of the CCD due to radiation damage or manufacturing faults, which can hold a fraction of the charge released by X-ray photon interactions. In the WT mode, the trapped charges can be released into the WT readout rows in a

[14] www.swift.ac.uk/analysis/xrt/

time scale comparable to the WT readout time. This is detected as additional low energy events[15].
In the GRS 1716–249 data reduction I selected only the grade 0 events as suggested by the hardware team. This grade filter, in addition to reducing spectral distortions[16], provides a first correction to the pile-up (a detailed treatment of this issue is reported in Section 4.3.2.2). All these procedures are implemented and automatised by the *xrtpipeline* script. The output are re-calibrated events according to the CALDB files (available in HEASARC site[17]). In addition, an exposure map is created corresponding to each event file. This is used to correct for the loss of flux which occurs when the source is positioned over a CCD bad column (see Section 4.3.2.2 for more detail).
To extract the spectra and light curves of GRS 1716–249 I run the task *xrtproducts* applying regions[18], time and energy filters. Using the ds9 tool I selected a circular region for the source in each event file with a radius of about 20 pixels as suggested by the hardware team[19] (1 pixel = 2.36″). Since a number of spectra extracted using this circular region showed some spectral distortion due to pile-up (see Figure 4.7), I carried the pile-up correction out selecting an annular region that could remove the innermost and brightest pixels in the source region (see Section 5.1.1). More information about the pile-up issue are reported in Section 4.3.2.2.
The background for each spectrum of GRS 1716–249 has been extracted from a region of the same size and shape of the source region located away from the source PSF so to avoid the inclusion of source counts.
The *xrtproducts* task produces the spectra and the corresponding Auxiliary Response Files (ARF) created using in input the exposure maps, thus ensuring the correction for some damaged columns (hereafter *bad columns*, see Section 4.3.2.2), and applying the PSF correction for the loss of counts due to any geometry of the extraction region. Furthermore, an exposure map is generated during the reduction procedure. This is then used to generate the ARF, thus ensuring the correction for bad columns, bad pixels and any loss of counts caused by the selection of an annular extraction region (if the source is piled-up).
For the spectral analysis of GRS 1716–249 I used the ARF files described above. Then I used for each spectrum the corresponding Redistribution Matrix (RMF, these are included in the CALDB) to associate the correct energy to each instrument channel. Finally, to apply the χ^2 statistics I grouped the channels of each spectrum for having at least 50 counts per energy bin.

[15] https://www.swift.ac.uk/analysis/xrt/digest_cal.php#traps
[16] The software was recently updated implementing the correction to identify and remove the trailing charge from WT event files. The spectra extracted with the latest HEASOFT version show strongly reduced fluctuations at low energies. For more information I refer to https://www.swift.ac.uk/analysis/xrt/digest_cal.php#trail and https://heasarc.gsfc.nasa.gov/docs/software/lheasoft/release_notes.html.
[17] https://heasarc.gsfc.nasa.gov/docs/heasarc/caldb/caldb_intro.html
[18] It is possible to apply a region filter on PC and WT data because in the events is included the information on the position of the source.
[19] https://www.swift.ac.uk/analysis/xrt/xselect.php

4.3.2.2 XRT issues

The XRT telescope shows some instrumental issues that affect the data[20]. In the following I report on the main issues that I confronted in the XRT data analysis of GRS 1716–249.

Bad columns

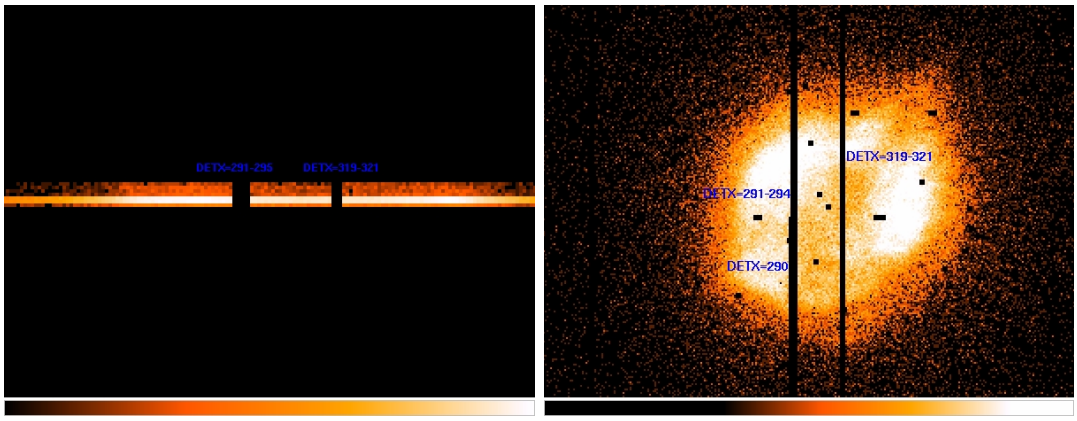

Figure 4.6: The supernova remnant, Cas A, observed with XRT in WT (left panel) and PC (right panel) mode. In both the cases the source is positioned over the bad columns. The images are from https://www.swift.ac.uk/analysis/xrt/digest_sci.php.

A micrometeorite collided with the CCD damaging a small number of columns (*bad columns*) and made the Photo-Diode operative mode unusable.
Since these bad columns are near the centre of the telescope FoV, it is possible that during the observations in WT and PC modes the sources can occasionally lie on top of them. When it occurs the number of counts and the flux are underestimated. Therefore, both the extraction of the spectra and light curves have to be corrected for the loss of counts.
It is worth noticing that these columns are evident only when we plot the image in detector coordinates, or for a single orbit at a time (see Figure 4.6). For sources that lie close to the bad columns, the correction factor which compensates for the flux loss due to those columns is very sensitive to the exact location of the object on the CCD. Thus, the software for the analysis compensates for the bad columns' issue through the production of an exposure map by incorporating it into the generated ARF.

Pile-up

Pile-up is due to two or more photons hitting a single pixel, or collected in neighbouring pixels on CCD before that the charge has been read-out (Ballet, 1999). It occurs when the observed source is too bright and/or the read out time of the detector is "slower" than the rate of incident photons.
This issue affects mainly the centre of the XRT PSF. The observations performed

[20] https://www.swift.ac.uk/analysis/xrt/digest_sci.php

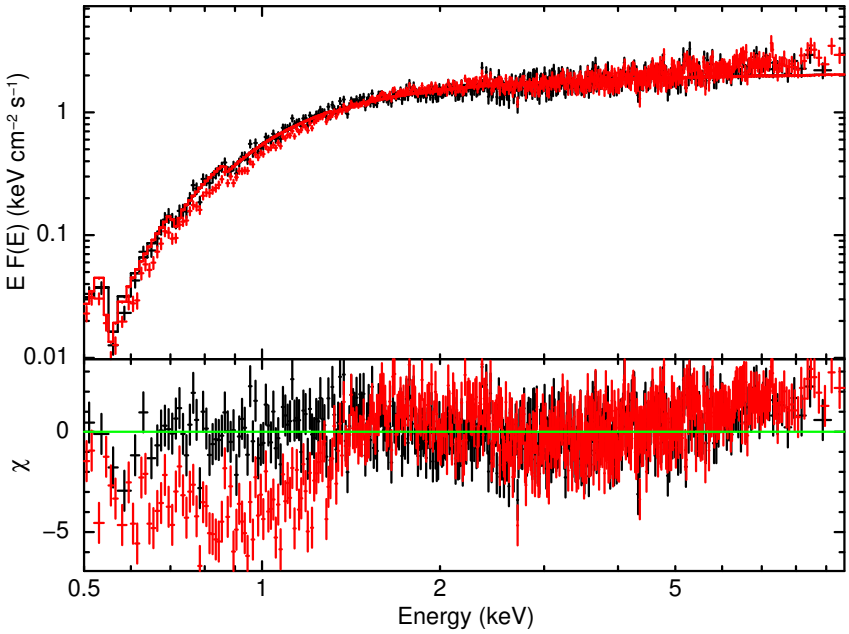

Figure 4.7: GRS 1716–249 pointing #30. The figure shows the spectrum corrected for pile-up (black data) overlapped to the spectrum not corrected (red data). In red data are evident strong soft residuals and few hard residuals. That is due to the pile-up that make the spectrum harder.

in PC modes are more subjected to that issue, although very bright sources (fluxes higher than 600 mCrab) are affected by pile-up also in WT mode. The piled-up observations show a loss of information: the count rate results underestimated and the spectrum is harder than the real one. Figure 4.7 shows the spectrum of GRS 1716–249 of the pointing #30 before (red data) and after (black data) that the correction for pile-up has been carried out. As mentioned in Section 4.3.2.1, the pile-up effect can be corrected by selecting an adequate source region. Romano et al. (2006) showed that in the observation performed in WT mode, the pile-up correction should be applied for sources with count rate above $\sim$100 ct s^{-1} removing the events that fell in the pixel within the extension of the PSF core using a region with annular shape.
Performing this correction in the data sets of GRS 1716–249, I noticed that the observations with a count rate between 90–100 ct s^{-1}were still affected by pile-up. Therefore, I applied this correction to all the observations with a count rate higher than 90 ct s^{-1} . Figure 4.8 shows the spectrum of the pointing #24 of GRS 1716–249. Even though the count rate is $\sim$ 90 ct s^{-1}, the spectrum shows some residuals around 10 keV (red data) indicating that it is still affected by pile-up. More information about specific XRT observations to which I carried out the pile-up correction are reported in Section 5.1.1.
It is worth noticing that the increase of the flux entails an increase in the effects of pile-up. Therefore, it is necessary to exclude progressively a bigger region to

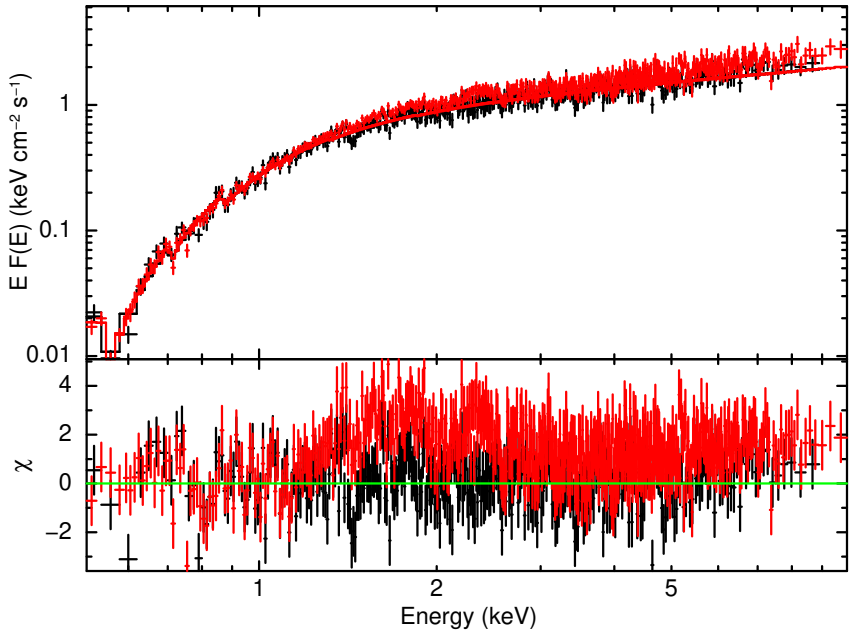

Figure 4.8: GRS 1716–249 pointing #24 with a count rate of ~ 90 cts. The residuals at high energies (red data) are corrected caring out the pile-up correction (black data).

correct the spectrum.

Rolling of the satellite

Another issue that I had to deal with during the data reduction is relative to rolling of the satellite during the observations due to operational reasons. This issue is particularly important in WT mode. The *Swift* pointing system has been designed to optimise the observation time, therefore the satellite slews to observe another source when the observed source goes out of the *Swift* FoV. Once the first source enters newly in the FoV of *Swift* the telescope starts again to observe it. In this phase it is possible that the satellite rolls changing its position angle (hereafter *roll angle*) respect the previous snapshot. That results in two or more strips with different angles (see Figure 4.9) which may have an impact on the ARF generation and on the background evaluation. Nevertheless, it can be easily fixed during the spectrum extraction procedure by splitting the main event file in two event files (or more according to the number of snapshots).

Even though some of the events files of GRS 1716–249 showed snapshots with different roll angles, the angles difference was generally so small to be considered negligible. I applied the roll angle correction only to the pointing #61.

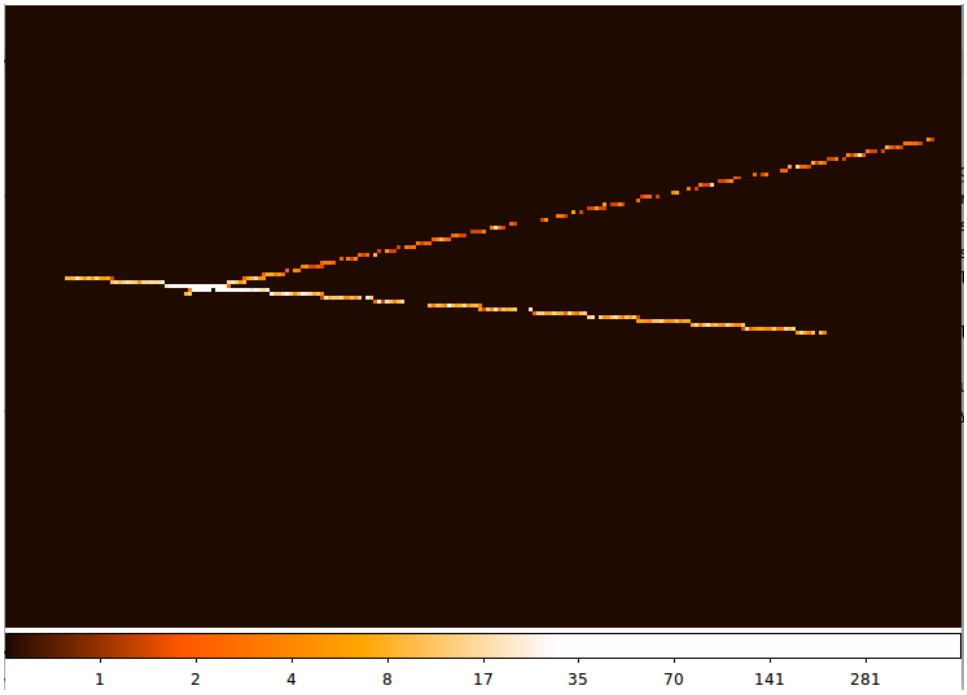

Figure 4.9: Pointing #61 of GRS 1716–249. In the image are evident two snapshots with different roll angles.

4.3.2.3 BAT data reduction

To extract the BAT spectra of GRS 1716–249 I used the BATIMAGER software (Segreto et al., 2010). This software is based on the cross-correlation via fast Fourier transform (FFT) between the shadowgram, the mask pattern and the iterative removal of sources.
The BATIMAGER software performs a preliminary cleaning to identify and subtract possible bright sources. Then, based on the analysis of the shadowgram residuals, the background is modelled and subtracted. These procedures allow to reduce the systematic error in the background reconstruction and to improve the signal to noise ratio for fainter sources. Then, a procedure which optimises both time and energy band of the detection is applied to the source.
At this point I could proceed to extract the spectra and the light curves of GRS 1716–249 using the program *spectra extractor* (v. 6.0). First, I defined the most adequate energy ranges and good time intervals (GTIs) to extract the spectra and light curves for my study. Since the spectral transition in BHTs can occur in a very short time (a few days), I extracted the light curves of GRS 1716–249 selecting a minimum GTI of 1 day. Assuming longer GTIs I observed that the variability of the source was diluted in the light curve with the main consequence losing the possibility to observe important features (dips and peaks). Then, to investigate the spectral variability of GRS 1716–249 in hard X-ray I extracted the light curves selecting two energy bands: one softer (15–30 keV) and one harder (30–90 keV). This allowed me to compute the hardness ratio (soft count rate over hard count rate) and to observe possible features due to the source spectral vari-

ation (e.g. spectral softenings) along the trend of the curve.
In a second step I extracted the spectra assuming longer GTIs (see Table 5.4) with the aim to improve the spectra statistics and to perform the broad band analysis of the source (the description of the broad band analysis of GRS 1716–249 and the results are reported in Chapter 5). Since the data statistics is high at low energies and decreases at high energies, I applied a logarithmic binning of the channels in order to improve the statistics at the high energies in the spectra.

4.3.3 INTEGRAL

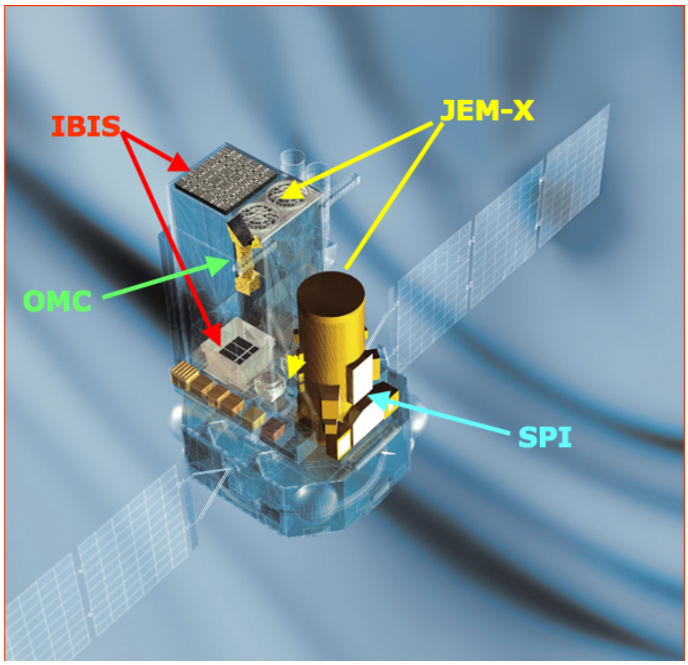

Figure 4.10: The *INTEGRAL* spacecraft.

The International Gamma-Ray Astrophysics Laboratory[21] [22] (*INTEGRAL*, Winkler et al., 2003) is an ESA medium-size scientific mission (M2) of the Horizon 2000 programme. *INTEGRAL* is lead by ESA with contributions from Russia and NASA. It was launched in 2002 October into an eccentric 72-hours orbit with an inclination of 52.2°, at a height from 9000 km up to 155000 km from Earth. The telescope is capable to perform high spectral and spatial observations in the 3 keV to 10 MeV energy domain.
The aim of the *INTEGRAL* mission is fine spectroscopy with imaging and accurate positioning of sources emitting at γ-ray energies. The fine imaging capability within the large FoV permits the accurate location and the identification of γ-ray sources. The wide energy range of *INTEGRAL* allows to study the changes in spectral shape over the evolution of the BHT outbursts and to observe the hard component up to 100 keV or even to the MeV range.

[21] https://heasarc.gsfc.nasa.gov
[22] https://www.cosmos.esa.int/web/integral

INTEGRAL carries two main γ-ray instruments and two monitor instruments (see Figure 4.10). The spectrometer SPI and the imager IBIS have been designed in order to complement each other:

SPectrometer on INTEGRAL (SPI, Vedrenne et al., 2003) performs high-resolution spectroscopy of astrophysical sources in the broad energy range from 20 keV to 8 MeV.
The gamma camera is a hexagonal array of 19 detectors with geometrical area of 508 cm^2. It is associated with a coded mask to perform imaging. The camera FoV is 16°. The telescope is characterised by an energy resolution of 2.5 keV (FWHM) at 1.33 MeV and a modest spatial resolution of 2.5°. SPI can localise the sources within 10′ depending on the source intensity. The imaging capabilities of the instrument are limited by the small number of detectors, in addition to the strong background. The problem is reduced increasing the number of measurements by dithering the whole spacecraft around the target of interest.

Imager on Board the INTEGRAL Satellite (IBIS, Ubertini et al., 2003) is a coded mask instrument optimised to provide fine imaging (12′ FWHM), with an unprecedented spatial resolution (1′–2′), accurate localisation of point sources (30″), good spectral resolution (9% at 1001 keV and 10% at 11 MeV) and high time resolution (61 μs).
The telescope operates in the 15 keV–10 MeV energy range with two simultaneously operating detectors. IBIS can be used to localise the sources seen by SPI below 200 keV even more precisely. The total FoV is 29.1°×29.4°, while the fully coded FoV is 8.3°×8°.
The spectrometer is composed of two detector planes: ISGRI and PICsIT. ISGRI is characterised by a collecting area of 2600 cm^2 and it is sensitive in the 15–1000 keV energy band.

These instruments are supported by the X-Ray Monitor JEM-X and the Optical Monitoring Camera OMC. They provide complementary observations in the X-ray (3–35 keV) and optical (V-band, 550 nm) energy bands:

Joint European X-Ray Monitor (JEM-X, Lund et al., 2003) plays a central role in the detection and identification of the γ-ray sources. It is a coded mask telescope. It works simultaneously with SPI and IBIS, even though its field of view is smaller (48° full camera FoV).
JEM-X provides images with 3′ angular resolution in the 3–35 keV energy band. The camera can localise point sources with ∼1′ accuracy.

Optical Monitoring Camera (OMC, Mas-Hesse et al., 2003) is an optical system. It is located on the focal plane with a Visible (V) filter to cover the energy range 500–600 nm. The optics focal length is of 154 mm and the FoV is of 5°×5°. The camera can perform long observations in the optical band simultaneously with those instruments observing at X-rays and γ-rays energies. This provides the possibility to investigate the nature and the physics of the sources over a broad wavelength range.

All four instruments are co-aligned with overlapping fully coded mask FoV and they observe simultaneously.

4.3.3.1 INTEGRAL data processing

SPI data reduction

To perform the reduction and analysis of the the SPI data of GRS 1716–249 I used the SPIDAI[23] software. The SPI camera records the signal contribution from several sources in the FoV, in addition to the source of interest. Therefore it is important to determine a sky model where these sources are shown. This component has to be defined carefully, in particular if there are strong or variable sources in the FoV.
For my study on the high energy emission in GRS 1716–249 (above 200 keV, see Chapter 6) I analysed ten revolutions (from revolution 1780 up to 1793), covering the period from February 2 to March 15, 2017. To obtain the SPI spectrum of GRS 1716–249 in each revolution I took the following steps:

- select the revolution;
- create the sky model selecting and inserting in the program the significant sources in the FoV;
- define the variability of the selected sources;
- specify the variability time scale of the normalisation of the background pattern;
- verify if any pointing is affected by solar flares and/or high solar activity, and remove the "bad" pointings.

Due to the low spatial resolution of SPI, it has been necessary to resort to the IBIS/ISGRI maps to resolve the possible sources to include in the sky model.
A continuous time interval during which all data acquired result from a specific pointing is called Science Window (SCW). For each SCW within the selected revolution, I selected the sources with a significance higher than 5σ in the ISGRI maps. Then, I verified that these sources were still significant in the full revolution ISGRI map selecting the most significant sources ($\sigma \geq 10$). Table 4.4 shows the selected sources I used to build the sky model for each revolution. To define the selected sources variability I used their ISGRI light curves with the SCW binning time. In the program I introduced their variability choosing between: constant flux during the revolution, constant flux over 3 SCWs or 1 SCW if the source was very variable. Then, I assumed a constant background during 12 Science Window (SCW). Some pointings in the revolutions 1787, 1790 and 1792 were affected by solar flares, therefore I removed them from the analysis.
Finally, I extracted the SPI spectrum of GRS 1716–249 for each revolution in 39 channels in 25–1000 keV energy range. Since I was mainly interested in studying the emission above 200–300 keV (see Chapter 6), I required at least 2σ significance

[23] https://sigma-2.cesr.fr/integral/documents/SPIDAI_user_manual.pdf

in the higher energy bin (i.e. $\geq$300 keV), up to the statistics was sufficient. Then, I summed up all the revolution spectra to maximise the spectrum statistics.

	1780	1782	1783	1786	1787	1789	1790	1791	1792	1793
Sco X-1	X									
GX 1+4	X	X	X	X	X	X	X	X	X	X
1E 1740	X		X			X	X	X	X	X
1A 1743	X	X	X							
GRS 1758	X	X	X	X	X	X	X	X	X	X
4U 1700	X	X	X	X	X	X	X	X	X	X
GX 17+2	X									
OAO 1657		X		X	X					X
GRO 1744-28		X								
GX 354-0		X	X							
KS 1741				X			X	X	X	X
GX 349+2				X	X			X	X	
GX 5-1					X					X
H 1702-429					X					
SLX 1735-269									X	

Table 4.4: Sources selected in each revolution.

Chapter 5

The long outburst of the black hole transient GRS 1716–249

In this chapter I present the X-ray study performed on the Galactic black hole transient GRS 1716–249 within the period 2016-2017.
After more than twenty years in quiescence, the source was observed being in outburst on December 18, 2016 by *MAXI* (Monitor of All-sky X-ray Image, Negoro et al., 2016; Masumitsu et al., 2016). This object was almost continuously observed with the XRT and BAT instruments on board of *Swift* during the whole outburst, from 2016 December until 2017 October. The XRT monitoring campaign (Del Santo et al., 2017) gave me the opportunity to study the evolution of the physical parameters of the accretion, possibly associated with the geometry variation, during the spectral transitions observed along the whole outburst. Then, I discuss the broad band spectral behaviour related to the timing proprieties of the source. In particular, I argue about the distance of the inner radius of the accretion disc from the black hole during the softer episodes observed, according to the truncated disc scenario.
Finally, I report on the radio observations performed during the outburst of GRS 1716–249 and on the source location on the radio/X-ray luminosity plane.

5.1 X-ray Observations and Data Reduction

I retrieved and analysed all XRT and BAT observations performed on GRS 1716–249 in the period 2016 December-2017 October. XRT was set in Window Timing (WT) mode (see Section 4.3.1). The X-ray spectral analysis was performed using XSPEC v. 12.9.1 and the errors on the spectral parameters are given at the 90% confidence level.

5.1.1 XRT

The XRT monitoring campaign of GRS 1716–249 was performed from January 28 (MJD 57781) to October 20, 2017 (MJD 58046), with target IDs 34924 and 88233. A log of the observations is provided in Table 5.1. Since in observations #046, #059 and #067 the source was out of the part of the CCD used in WT

mode, I excluded these data from the analysis.
The 0.2–10 keV count rate was extracted from each observation (see column 4 in Table 5.1) corrected for instrumental artifacts (i.e. bad columns on the CCD, for more information see Section 4.3.2.2) using the on-line products generator[1] (Evans et al., 2007, 2009).
With the same tool, I extracted the count rate in 0.5–2 keV and 2–10 keV energy ranges pointing by pointing in order to study the Hardness-Ratio (HR), defined as the ratio of the hard count rate over the soft one (see Section 5.3.2 and Figure 5.1).
Then, I reprocessed the XRT data running the task *xrtpipeline* (see Section 4.3.2.1). Since the source was bright, I selected only events with grade 0 (see Section 4.3.2.1). Then, I extracted the source and background spectra as explained in Section 4.3.2.1. Since in the pointings #054, #058 and #060 the source was on the edge of the CCD, I selected a region with a radii of 5, 8 and 4 pixels respectively.
Thus, the pile-up correction was carried out for observations with count rate (values plus uncertainties) $\geq 90\,\mathrm{ct\,s^{-1}}$ (see Table 5.1, more detail on the criteria adopted are reported in Section 4.3.2.2). For these observations I extracted the spectra from an annular region centred on the source with an outer radius of 20 pixels and an inner radius of 3 pixels.
To apply the χ^2 statistics I grouped the channels for having at least 50 counts per energy bin.

The fractional *rms* in the frequency range 0.035–10 Hz, was derived. It is worth noticing that after MJD 58000 (2017 September 4) the source count rate was too low ($\lesssim 5$ counts/s) to allow us to estimate the fractional *rms*. For this reason, no fractional *rms* values after this date have been reported.

[1] http://www.swift.ac.uk/user_objects/

Table 5.1: XRT pointings of GRS 1716–249 analysed in this work. The columns are: (1) sequence number, (2) start time in Terrestrial Time (TT), (3) exposure time, (4) 0.2–10 keV count rate and errors obtained using the on-line products generator (Evans et al., 2007, 2009). In columns (5) and (6) I report the photon index and the reduced chi squared, respectively, obtained by fitting spectra with an absorbed power-law model (see Sec. 6.3.2).
† Observations not used since GRS 1716–249 was out of the part of the CCD used in WT mode.
* Pile-up correction has been applied.
◇ Spectrum has been extracted in a region of radius smaller than 20 pixels since the source was on the edge of the CCD.
‡ Spectral fits need an additional component (i.e. DISKBB, see Sec. 5.3.3) to the simple power-law.

Seq # (1)	**Start Time** (2)	**Exposure (s)** (3)	**Count Rate (ct s^{-1})** (4)	Γ (5)	χ^2_ν**(dof)** (6)
001*	2017-01-28 00:08:01	992	93.1±0.4	$1.55^{+0.03}_{-0.03}$	1.08(342)
002*	2017-01-29 19:08:57	999	102±3	$1.57^{+0.04}_{-0.05}$	0.93(315)
003*	2017-01-31 00:05:15	683	95±2	$1.58^{+0.04}_{-0.04}$	1.10(248)
004*	2017-02-02 17:31:57	990	100±4	$1.60^{+0.03}_{-0.03}$	1.04(372)
005*	2017-02-04 18:56:10	924	100.2±0.3	$1.58^{+0.03}_{-0.03}$	1.03(373)
006*	2017-02-06 10:59:09	305	96±1	$1.53^{+0.06}_{-0.05}$	0.95(138)
007*	2017-02-08 04:15:42	946	97.9±0.3	$1.59^{+0.03}_{-0.03}$	1.12(384)
008*	2017-02-09 02:19:11	1478	80±12	$1.62^{+0.03}_{-0.03}$	1.07(432)
009*	2017-02-09 05:43:11	1282	87±11	$1.57^{+0.03}_{-0.03}$	1.02(365)
010*	2017-02-09 09:01:44	1451	97.4±0.3	$1.62^{+0.03}_{-0.02}$	1.03(452)
011*	2017-02-09 13:27:07	1287	102±1	$1.64^{+0.03}_{-0.03}$	1.14(400)
012*	2017-02-09 18:11:07	1360	103±3	$1.64^{+0.03}_{-0.03}$	0.89(364)
013*	2017-02-09 21:27:58	1367	103±0.7	$1.62^{+0.03}_{-0.03}$	1.00(425)

Table 5.1 – continued from previous page

Seq # (1)	**Start Time** (2)	**Exposure (s)** (3)	**Average Rate (ct s^{-1}, 0.2–10 keV)** (4)	Γ (5)	χ^2_ν**(dof)** (6)
014*	2017-02-11 07:11:47	949	101±3	$1.57^{+0.04}_{-0.03}$	0.99(299)
015*	2017-02-12 13:17:33	1209	81±12	$1.57^{+0.03}_{-0.03}$	1.06(431)
016*	2017-02-14 08:42:43	921	87±4	$1.55^{+0.03}_{-0.03}$	1.10(322)
017*	2017-02-14 19:35:14	975	91.6±0.4	$1.60^{+0.03}_{-0.03}$	0.99(358)
018*	2017-02-16 03:30:55	997	90.2±0.3	$1.59^{+0.03}_{-0.03}$	1.17(357)
019*	2017-02-22 13:56:26	1734	92±5	$1.57^{+0.03}_{-0.03}$	1.05(398)
020*	2017-02-24 09:00:33	966	100.3±0.3	$1.56^{+0.03}_{-0.03}$	1.19(362)
021*	2017-02-26 15:27:03	934	100.1±0.3	$1.60^{+0.03}_{-0.03}$	1.05(348)
022*	2017-03-09 12:48:10	1063	97.4±0.4	$1.63^{+0.03}_{-0.03}$	1.04(375)
024*	2017-03-15 18:46:20	985	90.2±0.3	$1.59^{+0.03}_{-0.03}$	1.08(348)
025*	2017-03-21 20:16:46	959	98.7±0.3	$1.67^{+0.03}_{-0.03}$	0.92(384)
026*	2017-03-27 22:36:50	940	124±11	$1.69^{+0.03}_{-0.03}$	0.92(333)
027*	2017-04-02 09:07:26	960	128±6	$1.76^{+0.03}_{-0.03}$	1.09(389)
029*‡	2017-04-07 08:50:41	1664	131±1	$1.85^{+0.02}_{-0.02}$	1.21(511)
030*‡	2017-04-08 23:11:36	965	131.0±0.7	$1.93^{+0.05}_{-0.03}$	1.33(413)
031*‡	2017-04-10 21:12:42	1933	143±6	$2.01^{+0.02}_{-0.02}$	1.19(514)
032*‡	2017-04-11 03:50:28	727	147±3	$2.06^{+0.03}_{-0.03}$	1.20(383)
033*‡	2017-04-12 11:26:48	1852	137±3	$1.98^{+0.02}_{-0.02}$	1.23(508)
034*‡	2017-04-14 00:37:03	929	123±7	$1.92^{+0.03}_{-0.03}$	1.13(351)
035*	2017-04-21 01:39:30	444	98.1±0.5	$1.75^{+0.04}_{-0.04}$	1.07(236)

Table 5.1 – continued from previous page

Seq # (1)	Start Time (2)	Exposure (s) (3)	Average Rate (ct s^{-1}, 0.2–10 keV) (4)	Γ (5)	χ^2_ν(dof) (6)
036	2017-05-05 17:42:16	1152	83±0.3	$1.72^{+0.02}_{-0.02}$	1.17(525)
037	2017-05-11 01:28:31	1258	79.2±0.3	$1.71^{+0.02}_{-0.02}$	1.03(538)
038*‡	2017-05-22 22:52:31	839	100.3±0.4	$1.90^{+0.03}_{-0.03}$	1.11(333)
039*	2017-05-26 17:55:22	724	91.8±0.5	$1.79^{+0.04}_{-0.04}$	1.15(261)
040	2017-06-02 12:29:01	354	78.6±0.5	$1.79^{+0.03}_{-0.03}$	0.99(295)
041	2017-06-07 00:25:55	1059	74.8±0.3	$1.75^{+0.02}_{-0.02}$	1.20(486)
042	2017-06-12 04:46:37	3354	75.4±0.9	$1.81^{+0.01}_{-0.01}$	1.15(641)
043	2017-06-17 02:58:56	1058	76±1	$1.82^{+0.02}_{-0.02}$	1.17(475)
044	2017-06-23 21:29:38	1033	74.0±0.3	$1.91^{+0.02}_{-0.02}$	1.13(464)
045*‡	2017-06-30 20:57:38	437	91±4	$2.13^{+0.04}_{-0.04}$	1.29(267)
046†	2017-07-09 18:39:24	964	-	-	-
047‡	2017-07-16 03:43:26	978	66.9±0.3	$2.12^{+0.02}_{-0.02}$	1.31(413)
048*‡	2017-07-23 11:12:15	988	100.1±0.3	$2.64^{+0.04}_{-0.04}$	1.35(295)
049*‡	2017-07-25 15:33:47	980	106.0±0.3	$2.68^{+0.04}_{-0.04}$	1.30(286)
050*‡	2017-07-26 17:10:39	1491	110.6±0.3	$2.79^{+0.03}_{-0.03}$	1.34(349)
051‡	2017-07-29 20:00:17	972	80.6±0.3	$2.57^{+0.02}_{-0.02}$	1.41(404)
052‡	2017-07-30 18:30:24	973	78.3±0.3	$2.55^{+0.02}_{-0.02}$	1.42(397)
053‡	2017-07-31 22:58:09	919	74.7±0.3	$2.53^{+0.03}_{-0.03}$	1.46(388)
054◇‡	2017-08-06 19:19:08	863	20.8±0.2	$1.95^{+0.04}_{-0.04}$	0.99(229)
055‡	2017-08-11 06:27:11	817	28.7±0.2	$1.87^{+0.04}_{-0.04}$	0.99(263)

Table 5.1 – continued from previous page

Seq # (1)	**Start Time** (2)	**Exposure (s)** (3)	**Average Rate (ct s^{-1}, 0.2–10 keV)** (4)	Γ (5)	χ^2_ν**(dof)** (6)
056	2017-08-13 09:08:40	1081	23.1±0.2	$1.81^{+0.04}_{-0.03}$	1.17(277)
057	2017-08-15 05:46:59	1058	21.4±0.1	$1.74^{+0.04}_{-0.04}$	0.95(252)
058$^{\diamond}$	2017-09-08 03:38:00	1667	4.24±0.07	$1.58^{+0.07}_{-0.06}$	0.93(107)
059†	2017-09-11 01:47:00	1529	-	-	-
060$^{\diamond}$	2017-09-15 00:05:15	1226	2.85±0.08	$1.52^{+0.11}_{-0.10}$	0.89(51)
061	2017-09-17 00:05:15	1106	3.31±0.07	$1.58^{+0.11}_{-0.10}$	0.95(45)
062	2017-09-21 01:07:13	1639	3.24±0.06	$1.55^{+0.07}_{-0.07}$	0.95(94)
063	2017-10-01 00:10:50	1425	4.09±0.06	$1.47^{+0.08}_{-0.07}$	0.99(84)
064	2017-10-05 01:25:00	1591	4.29±0.07	$1.56^{+0.09}_{-0.08}$	1.29(69)
065	2017-10-10 00:57:59	1372	3.61±0.06	$1.63^{+0.10}_{-0.09}$	1.05(68)
066	2017-10-15 00:33:11	1477	3.66±0.06	$1.61^{+0.08}_{-0.08}$	1.27(75)
067†	2017-10-20 11:21:50	1388	-	-	-
ID 88233001*‡	2017-07-28 16:51:27	3716	100.0±0.2	$2.75^{+0.02}_{-0.02}$	1.57(481)

5.1.2 BAT

BAT observed GRS 1716–249 almost continuously from December 1, 2016 (MJD 57723). The data were processed using the `BAT-IMAGER` software (see Section 4.3.2.3, Segreto et al., 2010) and the official BAT spectral redistribution matrix was used.
I extracted the light curves in two energy bands (15–30 keV and 30–90 keV) in order to compute the HR, defined as the count rate ratio [30–90] keV/[15–30] keV, with one-day time interval.
I extracted the spectra in 30 channels with logarithmic binning in the energy range 15–185 keV. Due to the poor statistics of the hard X-ray emission at the beginning of the outburst, I excluded the data from MJD 57723 until MJD 57739.

5.2 Radio observations and data reduction

GRS 1716–249 was monitored in radio energy bands with ATCA, VLA and LBA telescopes (see Section 4.1). The radio data reduction was performed by collaborators at this research project. The observations and the main steps performed are reported in the next Sections.

5.2.1 ATCA

GRS 1716–249 was observed with the ATCA simultaneously in two 2-GHz bands, centred at 5.5 and 9.0 GHz, with the array in its extended 6D configuration, with a maximum baseline of 6 km. The data reduction was performed using the Multichannel Image Reconstruction, Image Analysis, and Display MIRIAD software package (Sault et al., 1995) and the Astronomical Image Processing System (AIPS; Greisen, 2003). Following deconvolution, the source flux density has been measured by fitting a point source in the image plane.

5.2.2 LBA

The LBA observed GRS 1716–249 three times between February and August 2017. Details of the different observations are given in Table 5.2.

Program code	Date, Time (UT)	MJD	Bandwidth	Array
V447D	2017-02-21, 17:18–02:30	57805.91 ± 0.19	1×64 MHz	At-Cd-Ho-Mp
V447E	2017-04-22, 11:56–23:00	57865.73 ± 0.23	4×16 MHz	At-Cd-Ho-Mp
V447F	2017-08-13, 06:56–16:00	57978.48 ± 0.19	4×16 MHz	At-Cd-Ho-Ke-Mp-Pa-Td-Ti-Wa-Yg

Table 5.2: LBA observations of GRS 1716–249. Station codes are At (the phased-up ATCA); Cd (Ceduna); Ho (Hobart); Ke (Katherine); Mp (Mopra); Pa (Parkes); Td (the 34m DSS36 antenna at Tidbinbilla); Ti (the 70m DSS43 antenna at Tidbinbilla); Ww (the Warkworth 12m antenna); Yg (Yarragadee).

Data were correlated using the DiFX software correlator (Deller et al., 2011), and reduced using AIPS. GRS 1716–249 flux density was determined by fitting a

point source in the image plane, since in no case was it observed to be extended. The loss of one antenna (Cd) for the majority of the first observation (February 21, 2017) meant that imaging with three antennas could not reliably reproduce the source structure, so for this epoch the data were fitted with a point source in the *uv*-plane.

5.2.3 VLA

Further observations of GRS 1716–249 were performed with the VLA.
The array was in its moderately compact C configuration. The antennas were splitted into two subarrays of 14 and 12 antennas, each of which observed simultaneously in two 1-GHz basebands, centred at 5.25 and 7.45 GHz, and 8.8 and 11.0 GHz, respectively.
Data reduction was carried out following the procedures within the Common Astronomy Software Application (CASA; McMullin et al., 2007). GRS 1716–249 was significantly detected at all frequencies, and the source flux density was determined by fitting it with a point source in the image plane.

The final flux densities obtained by the radio monitoring campaign of GRS 1716–249 are detailed in Table 5.3.

Array	Date	MJD	Frequency (GHz)	Flux density (mJy)	Spectral Index
ATCA	2017 Feb 9	57793.835 ± 0.040	5.5	3.28 ± 0.05	-0.15 ± 0.19
ATCA	2017 Feb 9	57793.835 ± 0.040	9.0	3.04 ± 0.03	
LBA	2017 Feb 21	57805.911 ± 0.192	8.4	1.28 ± 0.15	-
LBA	2017 Apr 22	57865.729 ± 0.225	8.4	1.13 ± 0.11	-
VLA	2017 Aug 12	57977.256 ± 0.014	5.25	0.63 ± 0.04	-0.07 ± 0.19
VLA	2017 Aug 12	57977.256 ± 0.014	7.45	0.48 ± 0.05	
VLA	2017 Aug 12	57977.256 ± 0.014	8.8	0.68 ± 0.11	
VLA	2017 Aug 12	57977.256 ± 0.014	11.0	0.70 ± 0.14	
LBA	2017 Aug 13	57978.479 ± 0.188	8.4	0.29 ± 0.04	-

Table 5.3: Measured radio flux densities of GRS 1716–249. Quoted uncertainties are statistical only. Nominal systematic uncertainties are of order 5% for the VLA and ATCA, and at least 10% for the LBA. VLA flux densities have been corrected for the measured phase decorrelation, as described in Paragraph 5.2.3.

5.3 Results and Discussion

The XRT and BAT count rate and HRs evolution of GRS 1716–249 are shown in Figure 5.1.
I built the XRT light curves in 0.5–2.0 keV and 2.0–10.0 keV energy band (see panel *a* in Figure 5.1) and BAT light curves in 15–30 keV and 30–90 keV energy bands (see panel *c* in Figure 5.1). Then, I have computed the XRT and BAT HRs as the ratio 2.0–10 keV/0.5–2.0 keV and 30–90 keV/15–30 keV, respectively.

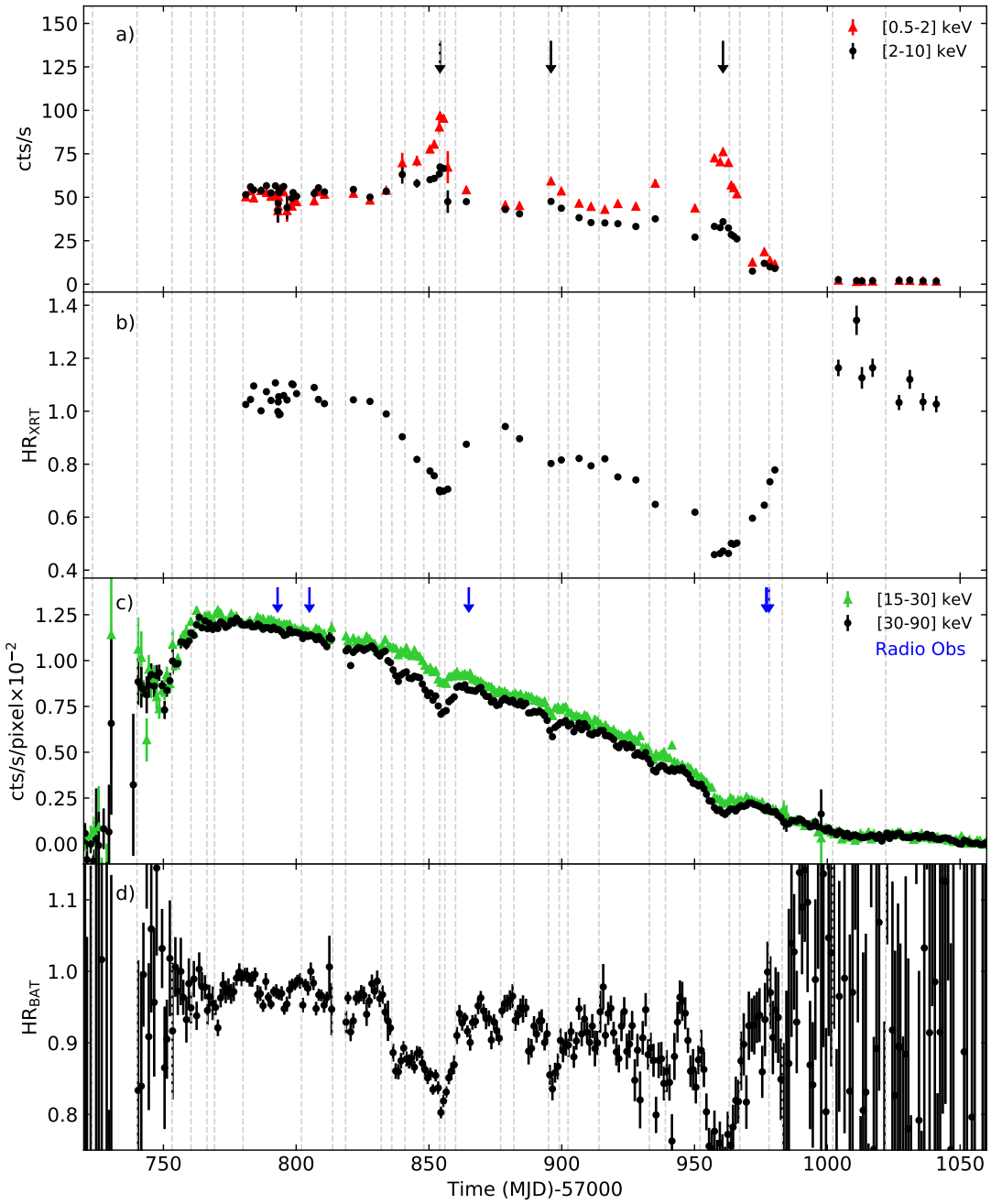

Figure 5.1: XRT light curves in the 0.5–2 keV and 2–10 keV energy ranges, extracted by pointing (panel *a*), plotted with the corresponding hardness ratio (panel *b*). In panel *c*, I show the 15–30 keV and 30–90 keV light curves observed by BAT, with a 1-day binning time, and the related hardness ratio (panel *d*). Dashed lines indicate the GTI considered for the broadband spectral analysis (see Table 5.4). In the XRT light curve, three strong peaks at MJD 57857.03, 57906.52 and 57964.77 (marked with black arrows) in correspondence to dips in the BAT light curve and in the hardness ratios have been observed. This indicates softening in the X-ray spectra.

I noted three peaks in the XRT light curves (panel *a* in Figure 5.1) which reach their maximum on MJD 57854.16 (#032) with a total of 143 ct s^{-1}, on MJD

57895.95 (#038) with 97 ct s^{-1} and on MJD 57960.72 (#050) with 103 ct s^{-1}. They correspond to dips in the BAT light curves (panel *c* in Figure 5.1) and in both the HRs (panels *b* and *d* in Figure 5.1). These clearly indicate a spectral softening. Furthermore, I observed that the third peak corresponds to the softest observed episode: the 2–10 keV count rate was lower than the 0.5–2 keV count rate by a factor of two, whereas it was of 30% and 20% for the first two peaks.

An useful tool to describe the spectral evolution of BHTs is the Hardness-Intensity Diagram (HID, see Paragraph 2.4.2). To observe the spectral evolution of GRS 1716–249 during the outburst, I plotted the XRT total 0.5–10 keV count rate versus the count rate ratio 2.0–10 keV/0.5–2.0 keV. I show the resulting HID in Figure 5.2 (top panel).
It is worth noting that due to the late XRT trigger with respect to the outburst beginning (the XRT monitoring started a few days after the hard X-ray peak), the HS right-hand branch in the HID was missed and the q-track starts from the bright HS. The outburst evolved towards the IMS on the horizontal branch. The three soft X-ray peaks in the XRT light curves are shown on the HID with a purple triangle, a green diamond and a magenta square. I observed the X-ray spectra of GRS 1716–249 to soften and harden twice along the upper IMS branch, until it reaches the softest observed state (magenta square), then the flux starts to decrease and the source simultaneously becomes harder along a diagonal track. The final shape of this HID is different from the q-track shape observed in the majority of BHTs (e.g. GX 339–4 , Belloni et al., 2006; Dunn et al., 2010). Indeed there is not a clear SS branch on the left side of the diagram as also observed in H 1743–322 and MAXI J1836–194 by Capitanio et al. (2009) and Ferrigno et al. (2012), respectively.

5.3.1 *XRT* temporal variability

As illustrated in the Paragraph 2.4.3, in BHTs the different spectral states are classified based on the fractional *rms* of the variability (Muñoz-Darias et al., 2011). Therefore, I studied the evolution of the fractional *rms* during the GRS 1716–249 outburst (Figure 5.2 bottom panel). The fractional *rms* measured from the XRT data is not directly comparable with those from *RXTE*/PCA (Muñoz-Darias et al., 2011), because of the different energy bands which the two instruments are sensitive to[2]. However, the overall behaviour of the fractional *rms* measured with XRT is expected to be similar to that would be measured by *RXTE*, with a difference in normalisation. In the first XRT observations GRS 1716–249 showed fractional *rms* between 25% and 30% (e.g. cyan dot), typical of the bright HS at the beginning of the HIMS branch. Then, after MJD 57830, the fractional *rms* started to decrease down to a value of 17% (MJD 57854), which corresponds to the purple triangle in the HID (Figure 5.2 top panel) and to the first dip in the HRs (Figure 5.1, b and d panels). Afterwards the fractional *rms* increased again up to values of about 25%, then a second dip

[2]Rossi X-ray Timing Explorer *RXTE*/PCA is a collimator that covers a sky region about 1∘. The instrument is sensitive in 2–60 keV energy band, while *Swift*/XRT observes in the range 0.2–10 keV (Paragraph 4.3.1).

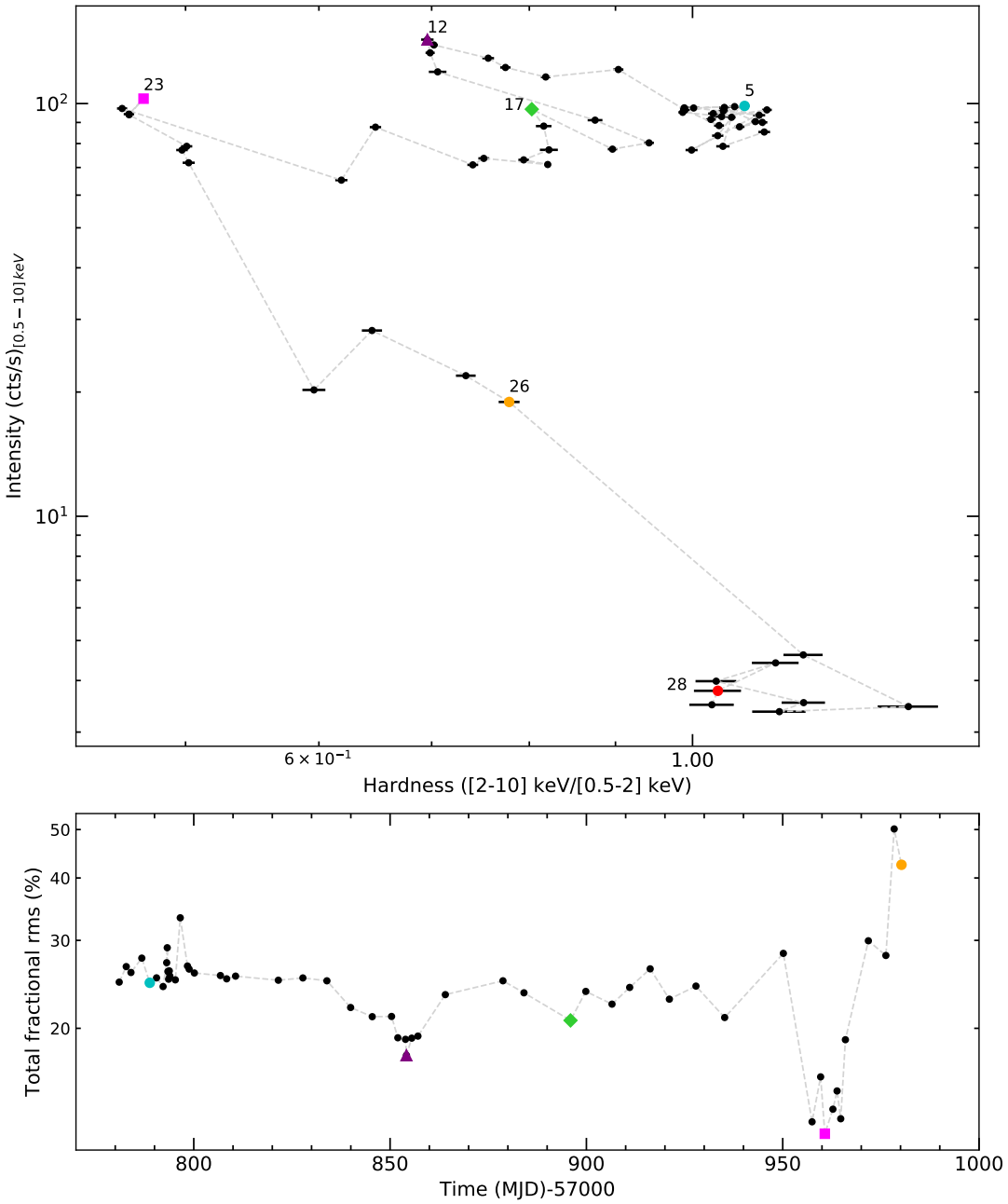

Figure 5.2: *Top panel:* Hardness-Intensity Diagram. The coloured dots are associated with the broadband spectra shown in Figure 5.5. The outburst has been observed by XRT when GRS 1716–249 was at the top-right side of the pattern (cyan dot, broadband spectrum *5*), then it evolves along the horizontal branch (purple triangle, spectrum *12*). It reaches the softest state (magenta square, spectrum *23*) and then takes a diagonal trajectory (orange dot, spectrum *26*) on its return to the hard state (red dot, spectrum *28*), before going in quiescence. The magenta square, purple triangle, and green diamond correspond to the softest points in each of the three softening episodes. *Lower panel:* XRT fractional *rms* evolution. The soft points observed in the HID correspond to fractional *rms* values typical of the HIMS (10%-30%, Muñoz-Darias et al., 2011).

(green diamond) with fractional *rms* of 20% at MJD 57896 (corresponding to the second softening) occurred. Simultaneously with the third HR softening, the fractional *rms* decreased down to 12% (magenta square, at MJD 57961). Finally, the *rms* of GRS 1716–249 rose back to 40% in the final part of the outburst, indicating that the source returned to the HS.
It worth noticing that the GRS 1716–249 fractional *rms* has never decreased below 10%. That suggests that the source did not perform the spectral transition to SIMS, usually expected at *rms*$\sim 7\% - 10\%$ (Muñoz-Darias et al., 2011).

5.3.2 XRT spectral analysis

I fitted each XRT spectrum in the $0.5 - 10$ keV energy band with an absorbed (TBABS) power-law model using the cosmic abundances of Wilms et al. (2000) and the cross section for interstellar absorption of Verner et al. (1996).
In Figure 5.3 I show the evolution of the spectral parameters. N_H shows values around (0.6-0.7) $\times\ 10^{22}\,cm^{-2}$, with a peak value at $\sim 0.9 \times 10^{22}\,cm^{-2}$ (MJD 57960.72). The photon index (Γ) remains between 1.5 and 1.7 throughout the whole outburst, except for significant increases during the three XRT peaks and BAT dips observed over the periods of spectral softening (Figure 5.1). The XRT spectrum corresponding to the first peak (2017 April 11, #032) shows a photon index $\Gamma \sim 2.1$, while on May 22 (#038) I obtained a photon index of ~ 1.9. The source reached its steepest spectral slope on July 26 (#050) with $\Gamma \sim 2.8$, corresponding to the lowest HR value and the highest $N_H \sim 0.9 \times 10^{22}\,cm^{-2}$, even though the reduced χ^2 is not statistically acceptable (see Table 5.1). I show the fitted spectrum of this last pointing in Figure 5.4. The high χ^2 obtained fitting this spectrum (and the other softer events) and the large column density variations derived in the last, and softest, events can be due to the inadequacy of the simple power law model adopted. Indeed, at low energies a possible flattening due to the presence of an accretion disc, can be artificially compensated by the increasing the column density. I therefore added a multicolor disc black-body (DISKBB, see Paragraph 2.2.2.1) component to the previous model in all spectra with $\chi^2_\nu > 1.1$. I estimated with the F-test that this component is required by all spectra with $\Gamma \geq 1.8$. However, I noted that in a few spectra where $\Gamma < 1.8$ with $\chi^2_\nu > 1.1$, the bad residuals are due to the known strong instrumental silicon (1.84 keV) and gold (2.2 keV) edges[3], so I considered these fits acceptable.

[3] https://www.swift.ac.uk/analysis/xrt/digest_cal.php

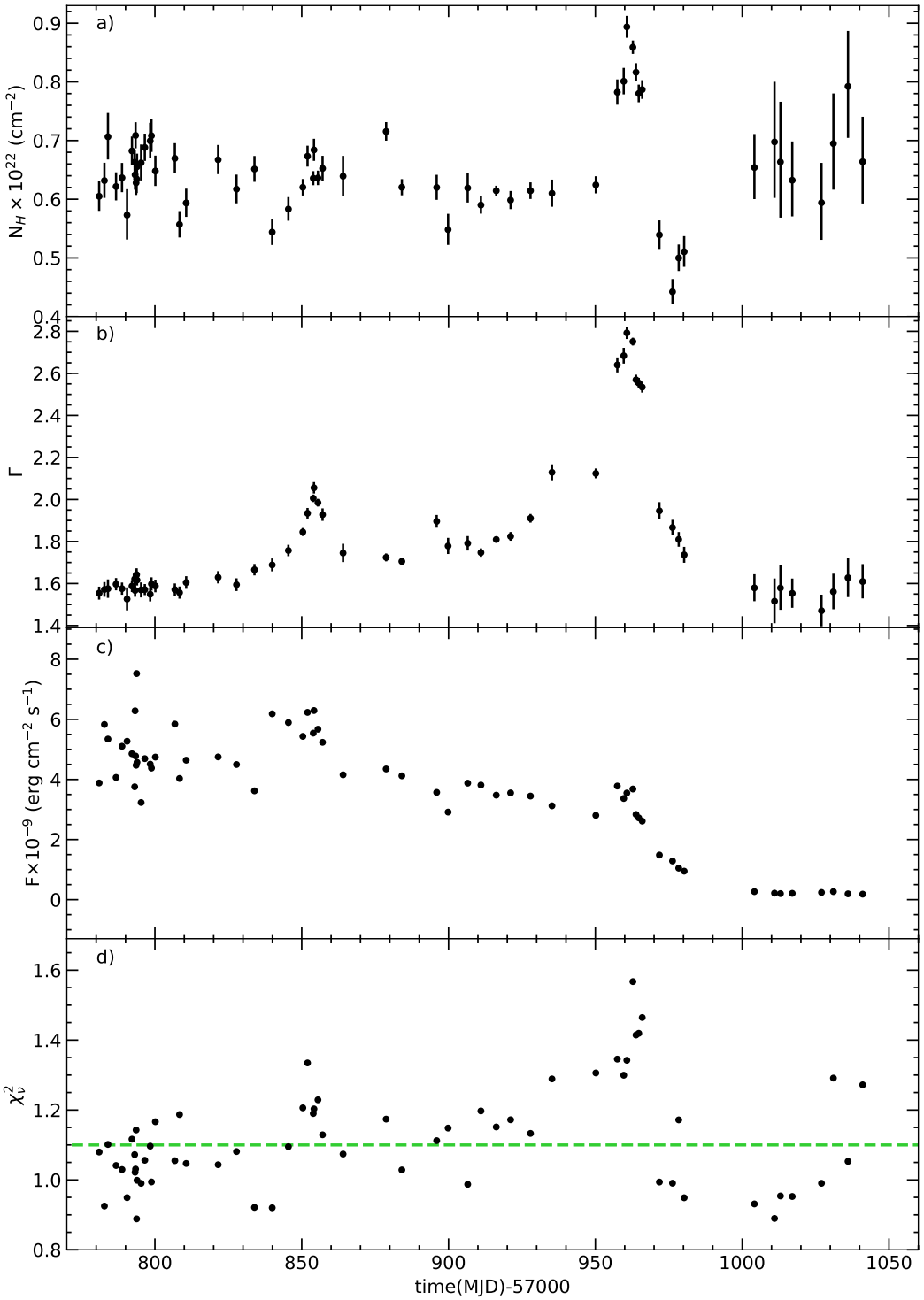

Figure 5.3: Parameters of the XRT spectra fitted with an absorbed power law model (TBABS*PO). From the top to the bottom panel: a) hydrogen column density in units of 10^{22} cm^{-2}, b) photon index, c) 0.5–10 keV absorbed flux in units of 10^{-9} erg cm^{-2} s^{-1}, d) reduced χ^2. The high variation of N_H is due to a non adequate spectral modeling. The spectra with a $\chi^2_\nu > 1.1$ and $\Gamma \geq 1.8$ require an additional multicolor disc black-body (DISKBB) component.

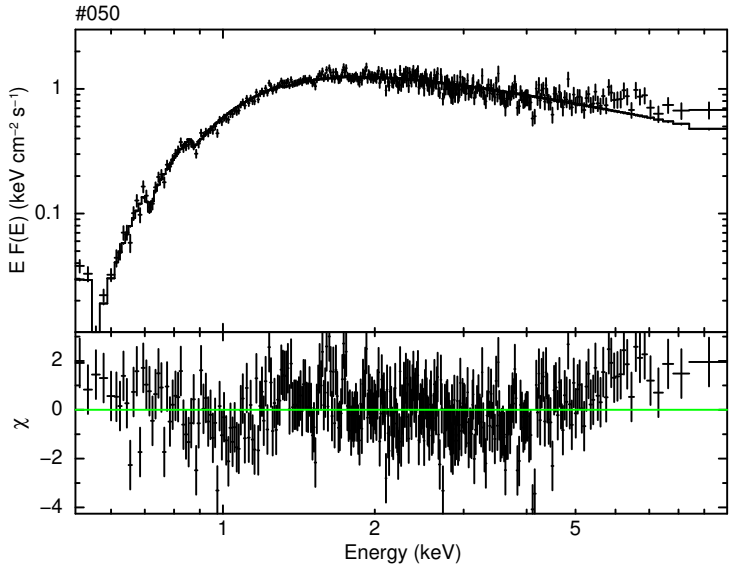

Figure 5.4: GRS 1716–249 spectrum of XRT pointing #50. The figure shows the spectrum fitted with the simple absorbed power law model (TBABS*PO). It shows a $\chi^2(dof)$=1.34(349) (see Table 5.1).

5.3.3 Broadband X-ray spectra

To improve the spectral analysis I added the averaged BAT spectra to perform a broadband fit.
I selected good time intervals (GTIs, see Tabble 5.4), using the light curves and HRs (see Figure 5.1), based on two selection criteria:

1) Constant HR in both BAT and XRT,

2) BAT flux variation lower than 20%, with the exception of the two last intervals where the variation is about 30%.

I point out that there are a number of BAT GTIs averaged spectra which do not overlap with any XRT observations. When the XRT coverage was available, I selected one XRT spectrum for each GTI, making sure that it was consistent, in terms of spectral parameters and flux, with the other XRT spectra within the same GTI.
In the broadband spectra I introduced a systematic error of 2% according to the instrument calibration guidelines.
The broadband spectra were fitted with an absorbed thermal Comptonisation model (TBABS plus NTHCOMP, a description of the models is reported in Paragraph 2.3.1.1). The best-fit parameters obtained are reported in Table 5.4.
I assumed that the seed photons followed a disc black-body distribution (parameter *inp_type*=1 in NTHCOMP) and I fixed the seed photon temperature at 0.1 keV every time the disc black-body component was not required.

Table 5.4: Good Time Intervals and best-fit parameters of the broadband XRT and BAT spectra performed with an absorbed thermal Comptonisation model and a disc black-body model when required. (1) Number of the spectrum, (2) sequence number of the XRT pointing selected within the BAT GTI, start (3) and stop (4) time of the GTI in MJD, (5) hydrogen column density in units of $10^{22}\,\mathrm{cm}^{-2}$, (6) photon index, (7) comptonising electron temperature in keV, (8) inner disc temperature, (9) inner disc radius, (10) unabsorbed bolometric flux (0.1–500 keV), disc and Comptonised component fluxes, (11) reduced χ^2.
* broadband spectra fitted all together keeping linked N_H and letting the other parameters to vary.

n	Seq. (#)	MJD Start	MJD Stop	$N_H \times 10^{22}$ (cm^{-2})	Γ	kT_e (keV)	kT_{in} (keV)	R_{in} $(\cos\vartheta)^{1/2}$ (km)	Flux × 10^{-8} (erg cm^{-2} s^{-1})			χ^2_r(dof)
									Bol	Disc	Comp	
(1)	(2)	(3)	(4)	(5)	(6)	(7)	(8)	(9)		(10)		(11)
1	-	57740.08	57752.85	-	$1.69^{+0.05}_{-0.05}$	>57	-	-	2.01	-	2.01	1.22(25)
2	-	57753.24	57757.49	-	$1.68^{+0.04}_{-0.04}$	>50	-	-	2.26	-	2.26	1.01(25)
3	-	57760.41	57766.39	-	$1.69^{+0.02}_{-0.02}$	55^{+12}_{-8}	-	-	2.51	-	2.51	0.91(25)
4	-	57769.24	57779.96	-	$1.69^{+0.01}_{-0.01}$	53^{+5}_{-4}	-	-	2.54	-	2.54	0.97(25)
5	005	57780.01	57801.96	$0.69^{+0.02}_{-0.02}$	$1.67^{+0.01}_{-0.01}$	48^{+4}_{-3}	-	-	2.37	-	2.37	1.01(399)
6	020	57802.01	57813.70	$0.61^{+0.02}_{-0.02}$	$1.65^{+0.01}_{-0.01}$	41^{+2}_{-3}	-	-	1.86	-	1.86	1.18(388)
7	022	57818.61	57831.99	$0.70^{+0.02}_{-0.02}$	$1.68^{+0.01}_{-0.01}$	47^{+4}_{-3}	-	-	2.19	-	2.19	0.99(401)
8	025	57832.02	57835.98	$0.67^{+0.02}_{-0.02}$	$1.70^{+0.02}_{-0.02}$	52^{+9}_{-6}	-	-	1.60	-	1.60	0.89(410)
9	026	57836.02	57840.96	$0.57^{+0.02}_{-0.02}$	$1.75^{+0.02}_{-0.02}$	50^{+7}_{-5}	-	-	2.42	-	2.42	0.90(359)
10	027	57841.00	57848.00	$0.58^{+0.02}_{-0.02}$	$1.77^{+0.02}_{-0.02}$	60^{+10}_{-7}	-	-	2.34	-	2.34	1.03(415)
*11**	030	57848.06	57853.97	$0.59^{+0.01}_{-0.01}$	$1.79^{+0.01}_{-0.01}$	52^{+5}_{-4}	$0.40^{+0.02}_{-0.02}$	$14.1^{+1.5}_{-1.5}$	2.25	0.13	2.12	1.12(3411)
*12**	032	57854.02	57855.96	$0.59^{+0.01}_{-0.01}$	$1.83^{+0.02}_{-0.02}$	58^{+13}_{-8}	$0.42^{+0.02}_{-0.02}$	$15.6^{+1.5}_{-1.3}$	2.14	0.20	1.94	1.12(3411)
*13**	034	57856.01	57860.00	$0.59^{+0.01}_{-0.01}$	$1.79^{+0.01}_{-0.01}$	52^{+7}_{-5}	$0.42^{+0.03}_{-0.03}$	$12.5^{+1.6}_{-1.1}$	1.85	0.12	1.73	1.12(3411)
14	035	57860.00	57876.96	$0.62^{+0.02}_{-0.02}$	$1.72^{+0.02}_{-0.02}$	56^{+7}_{-5}	-	-	1.81	-	1.81	1.00(262)

Table 5.4 – continued from previous page

n	Seq. (#)	MJD Start	MJD Stop	$N_H \times 10^{22}$ (cm^{-2})	Γ	kT_e (keV)	kT_{in} (keV)	R_{in} $(\cos\vartheta)^{1/2}$ (km)	Flux × 10^{-8} ($erg\,cm^{-2}\,s^{-1}$)			χ^2_r(dof)
									Bol	Disc	Comp	
(1)	(2)	(3)	(4)	(5)	(6)	(7)	(8)	(9)		(10)		(11)
15	036	57877.00	57881.95	$0.71^{+0.01}_{-0.01}$	$1.72^{+0.01}_{-0.01}$	66^{+13}_{-9}	-	-	1.97	-	1.97	1.09(550)
16	037	57882.00	57894.97	$0.62^{+0.01}_{-0.01}$	$1.72^{+0.01}_{-0.01}$	57^{+7}_{-5}	-	-	1.79	-	1.79	0.96(563)
*17**	038	57895.02	57898.94	$0.59^{+0.01}_{-0.01}$	$1.79^{+0.02}_{-0.02}$	54^{+12}_{-8}	$0.35^{+0.03}_{-0.03}$	$13.9^{+2.7}_{-2.0}$	1.32	0.07	1.24	1.12(3411)
18	039	57899.05	57901.32	$0.54^{+0.02}_{-0.02}$	$1.77^{+0.03}_{-0.02}$	73^{+40}_{-18}	-	-	1.17	-	1.17	1.11(287)
19	040	57902.27	57913.89	$0.59^{+0.02}_{-0.02}$	$1.76^{+0.02}_{-0.02}$	75^{+21}_{-13}	-	-	1.64	-	1.64	0.93(321)
20	043	57914.01	57932.96	$0.54^{+0.01}_{-0.01}$	$1.75^{+0.02}_{-0.02}$	80^{+24}_{-14}	-	-	1.47	-	1.47	0.96(380)
*21**	045	57933.01	57938.95	$0.59^{+0.01}_{-0.01}$	$1.81^{+0.02}_{-0.02}$	>70	$0.34^{+0.01}_{-0.01}$	$21.6^{+2.8}_{-2.1}$	1.24	0.16	1.08	1.12(3411)
*22**	047	57939.05	57951.97	$0.59^{+0.01}_{-0.01}$	$1.78^{+0.02}_{-0.02}$	90^{+41}_{-21}	$0.37^{+0.01}_{-0.01}$	$16.9^{+1.4}_{-1.3}$	1.13	0.14	0.99	1.12(3411)
*23**	050	57952.09	57963.00	$0.59^{+0.01}_{-0.01}$	$1.88^{+0.03}_{-0.03}$	74^{+46}_{-19}	$0.50^{+0.01}_{-0.01}$	$15.2^{+0.7}_{-0.7}$	1.11	0.38	0.73	1.12(3411)
*24**	052	57963.09	57966.98	$0.59^{+0.01}_{-0.01}$	$1.92^{+0.02}_{-0.04}$	>120	$0.45^{+0.01}_{-0.01}$	$14.7^{+0.8}_{-0.7}$	0.92	0.22	0.70	1.12(3411)
*25**	056	57967.02	57977.99	$0.59^{+0.01}_{-0.01}$	$1.80^{+0.01}_{-0.03}$	>150	$0.21^{+0.02}_{-0.01}$	$42.7^{+12.1}_{-10.2}$	0.60	0.08	0.52	1.12(3411)
26	057	57978.08	57982.99	$0.51^{+0.02}_{-0.02}$	$1.74^{+0.02}_{-0.03}$	>122	-	-	0.46	-	0.46	0.95(278)
27	-	57983.06	58001.97	-	$1.65^{+0.05}_{-0.05}$	>56	-	-	0.24	-	0.24	0.90(25)
28	061	58002.03	58022.0	$0.72^{+0.08}_{-0.07}$	$1.66^{+0.05}_{-0.06}$	>58	-	-	0.12	-	0.12	1.08(71)
29	066	58022.0	58075.38	$0.70^{+0.07}_{-0.07}$	$1.68^{+0.06}_{-0.06}$	35^{+32}_{-10}	-	-	0.08	-	0.08	1.23(101)

I observed that some spectra had poor χ^2_ν (see pointings marked with ‡ in Table 5.1) and showed strong residuals at low energies. In these cases I verified that the addition of a DISKBB component improved significantly the fit (F-test values always lower than 8×10^{-5}).

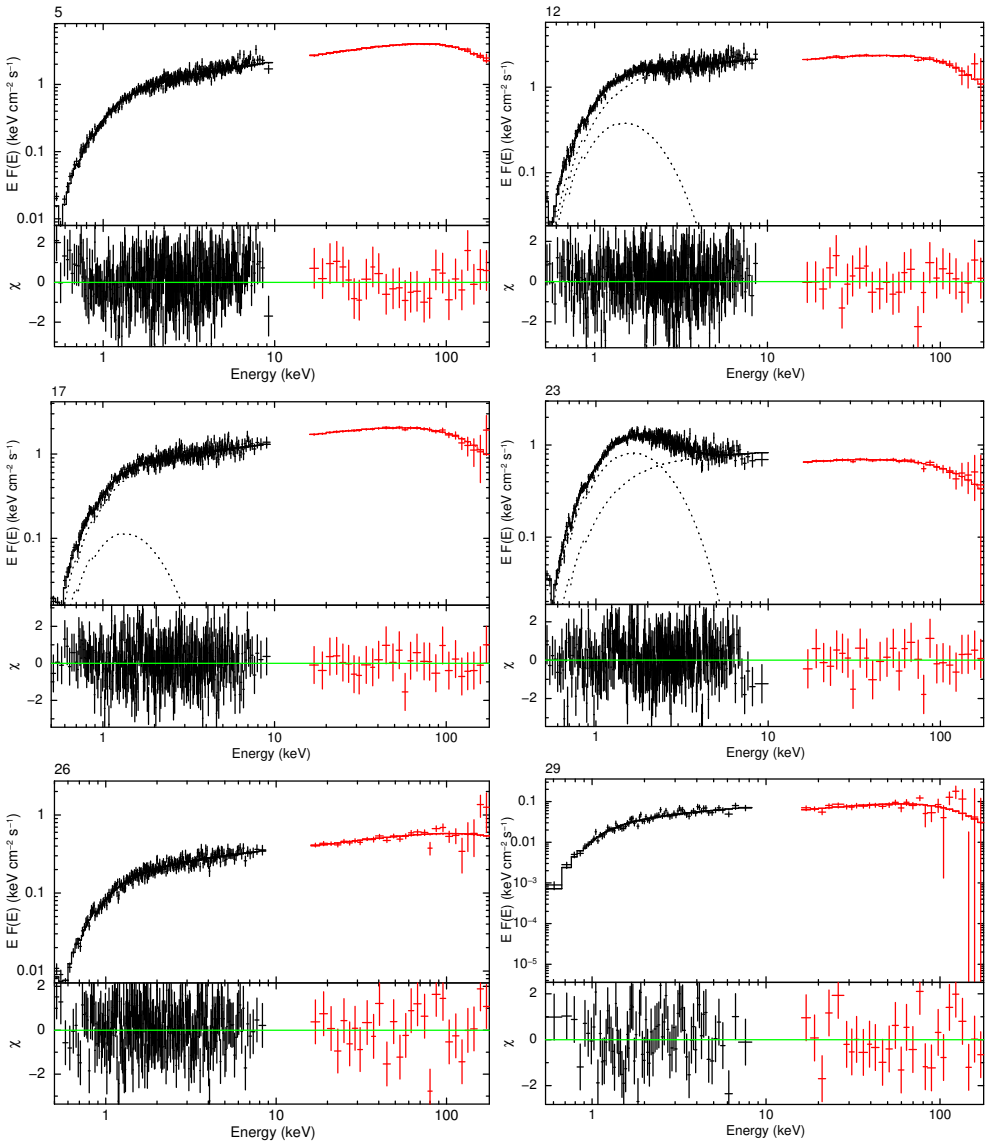

Figure 5.5: Broadband energy spectra of six different XRT pointings (#5, #32, #38, #50, #57 and #66, see Table 5.1) with average BAT spectra in the corresponding quasi-simultaneous GTIs (see Table 6.3.2). The broad band spectra are fitted with an absorbed Thermal Comptonisation model (TBABS*NTHCOMP) plus a multicolour disc black-body component (DISKBB), when required (*12*, *17* and *23*). The spectral parameters are reported in Table 6.3.2 (spectra *5*, *12*, *17*, *23*, *26* and *29*).

In Figure 5.5 I show the energy spectra, models and residuals for six representative observations: the three softening peaks (HIMS, *12*, *17*, *23*), one bright HS spectrum (*5*), one HIMS spectrum collected during the outburst decreasing phase (*26*) and a HS spectrum (*28*) collected before the source quiescence.

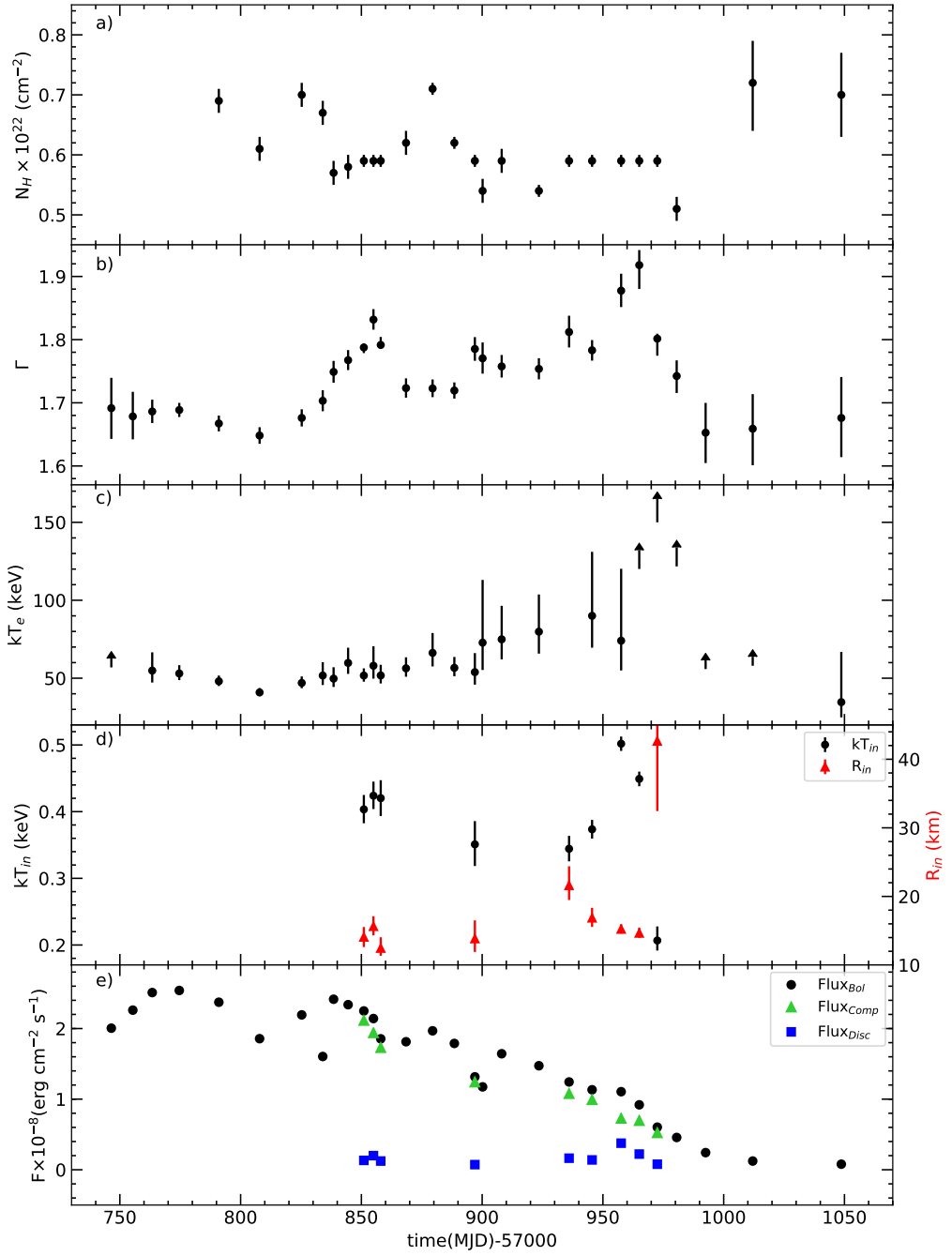

Figure 5.6: Evolution of the main spectral parameters and flux obtained fitting the broadband spectra with an absorbed thermal Comptonisation model (TBABS*NTHCOMP) plus a disc black-body component (DISKBB) when required (parameters reported in Table 5.4). From the top to the bottom panel: a) hydrogen column density in units of 10^{22} cm^{-2}, b) photon index, c) Comptonising electron temperature in units of keV, d) inner disc black-body temperature in units of keV (black dots) and inner disc radius depending on the inclination angle (R_c) in units of km (red triangles) and e) 0.1–500 keV unabsorbed bolometric flux in units of 10^{-8} erg cm^{-2} s^{-1}(black dots). The green triangles show the Comptonised flux and the blue squares show the disc flux. The disc luminosity never dominates the energetic of the source.

Fitting all spectra with a constant N_H, I noticed statistically significant discrepancies in the residuals of several spectra, so that I left this parameter free to vary in all the HS spectra. In these spectra I found that N_H varies from $0.51\times10^{22}\,cm^{-2}$ up to $0.72\times10^{22}\,cm^{-2}$ (see panel a in Figure 5.6). In the case of the nine spectra in which I added the disc component, I fitted them simultaneously keeping the N_H tied to each other (see Table 5.4). That let me found a unique $N_H = 0.59\times10^{22}\,cm^{-2}$ for these spectra. I observed that the photon index varies from 1.6 up to 1.9 (see panel b in Figure 5.6) and the electron temperature (kT_e, see panel c in Figure 5.6) is in the range 35–90 keV when the source is in the hard state. However, there are some case where I only obtained a lower limit on this parameter, e.g., the last spectral softening. It is possible that extra components in addition to the thermal Comptonisation play a role (i.e. non-thermal Comptonisation, reflection) in the intermediate states. Nevertheless, the BAT statistics and the poor high energy coverage do not allow me to disentangle these components.

The thermal disc component is well detected in the spectra collected during the three peaks observed in the XRT light curve. The inner disc temperature (kT_{in}) varies between 0.2 and 0.5 keV, the latter was observed during the third peak softening (see panel d in Figure 5.6). These findings are in agreement with Muñoz-Darias et al. (2011) who found that the presence of the accretion disc is detected when the fractional *rms* is ∼20%.

In the spectra collected during the peak of the three softenings (spectra *12*, *17* and *23* in Table 5.4), I estimated that the disc flux contributes 9%, 5% and 34%, respectively, to the total unabsorbed bolometric flux of GRS 1716–249. This finding, put together with the *rms* trend always higher than 10% (see Paragraph 5.3.1), supports the hypothesis that in spite of the three softening events that occurred during the outburst, GRS 1716–249 did not perform the transition to the canonical soft state (neither to the SIMS). Therefore, GRS 1716–249 could be added to the sample of X-ray binaries that have shown "failed" state transitions outburst (see Paragraph 2.4.2), in which the source does not complete the full q-track pattern in the HID.

In their study on an all-sky database of galactic BHTs, Tetarenko et al. (2016) found that ∼40% of sources are "hard only", including also sources showing "failed" state transition outbursts (i.e., HS-HIMS only). The authors suggest that the mass transfer rate ($\dot{M}$) over the whole outburst could be insufficient to allow the source to perform the transition to the soft states. Indeed, they found that all "hard only" sources show outburst peak luminosities lower than $0.11\,L_{Edd}$. I observed that the peak bolometric luminosity of GRS 1716–249 (L_{peak} ∼$0.03\,L_{Edd}$ for a black hole mass of $4.9\,M_\odot$ (Masetti et al., 1996)) is in agreement with their limit.

On the other hand, it is worth noticing that the "failed" state transition source Swift J1745–26 (Del Santo et al., 2016) showed L_{peak} ∼$0.37\,L_{Edd}$ ($M_{BH} \sim 10\,M_\odot$ and d∼7 kpc; Muñoz-Darias et al., 2013), which is more than a factor of three higher than the upper limit reported in Tetarenko et al. (2016). This would suggest that the overall mass-transfer rate during the outburst is not the only parameter involved in the "failed" state transition behaviour or that the limit is

higher than what Tetarenko et al. (2016) thought. However, although the most widely accepted distance of Swift J1745–26 is 7 kpc (Curran et al., 2014; Kalemci et al., 2014), this value is poorly constrained (Muñoz-Darias et al., 2013). Thus, if we assume a distance lower than ∼4 kpc, even the BHT Swift J1745–26 would fall within the proposed upper limit of 0.11 L_{Edd}.
In addition, I have estimated the inner disc radius of GRS 1716–249 as a function of the inclination angle (see Table 5.4) from the DISKBB normalisation (see Eq. 2.16). It is worth noticing that from the data it is possible to derive the apparent radius R_{in}. This is related to the true inner radius r_{in} as:

$$r_{\rm in} = \xi f^2 R_{\rm in} \tag{5.1}$$

where ξ=0.41 is the correct factor for the zero-torque inner boundary condition (Kubota et al., 1998) and f=1.7 is the spectral hardening factor (Shimura & Takahara, 1995). Therefore, I applied these correct factors to calculate an upper limit on the inner radius of the GRS 1716–249 accretion disc.
In Figure 5.7 (left), I plot R_{in} $(\cos\vartheta)^{1/2}$ (hereafter R_c) versus kT_{in} of GRS 1716–249 which shows that most of the measurements are consistent with a constant radius R_c ∼15 km. There is only one point (at lower temperature) that appears to have a significantly higher inner disc radius (larger than 40 km) and a second point with a value about ∼23 km which is not consistent with the mean radius. These two points correspond to observations when the source was in a harder state in which the inner accretion disc may have been larger. Indeed, in the truncated disc model scenario (as explained in Paragraph 2.4.4), the inner radius of the accretion disc decreases as the source become softer and it grows again when the source gets harder (see red triangles in panel c in Figure 5.6).
I also estimated whether the disc luminosity varies as a function of the inner disc temperature according to $L \propto T^4$. I show the observed disc flux and temperature against each other for all observations where R_c was almost constant in Figure 5.7 (right).

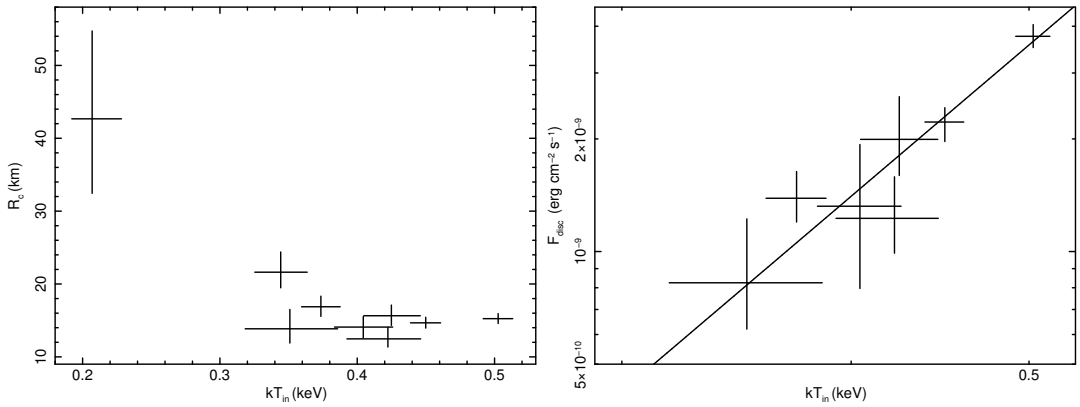

Figure 5.7: *Left panel:* R_{in} $(\cos\vartheta)^{1/2}$ (R_c) as a function of the inner disc temperature. R_c decreases with the increase of the temperature until it reaches an almost constant value. *Right panel:* the observed disc flux versus the inner disc temperature including only spectra with R_c almost constant. The slope of the power-law in log-log is $\alpha = 4.2 \pm 1.0$, in agreement with a constant inner disc radius scenario.

The power-law index from the best-fit is $\alpha = 4.2 \pm 1.0$ (χ^2(dof) = 4.5(5)). The probability to have the χ^2 obtained is of 0.52%. This suggests that the inner disc temperature variations are only driven by changes in mass accretion rate at constant inner disc radius ($R_{in} \propto \dot{M}$), and appears inconsistent with a scenario where the inner disc radius varies at constant mass accretion rate ($L \propto T^{4/3}$; Done et al., 2007). This is particularly evident within the third softening when a flux variation of about a factor of three is observed in combination with a constant R_c and an increase of kT_{in} (see Table 5.4 and Figure 5.6 panel c).
The GRS 1716–249 behaviour appears in agreement with a truncated disc model scenario, where the inner radius of the accretion disc is at large radii when the source is in a hard state, while it is smaller when we observe softer spectra. In addition, my results suggests that, even though the disc temperature continues to increase, the inner accretion disc had reached a constant value. Therefore, I argue that GRS 1716–249 might have reached the ISCO in the HIMS.
The observation of specific periodic phenomenology (i.e. eclipses and/or dips) in the XRBs light curves leads to place constrain onto the inclination angle of the systems. The direct occultation of the compact object (eclipse) by the companion star and the partial covering by an accumulation of matter on the point where the accreted material impacts the outer part of the accretion disc (dip), produce characteristic features in the light curves. However, these phenomena can be observed only if the binary system has a large inclination angle i with respect to the observer (Figure 5.8).

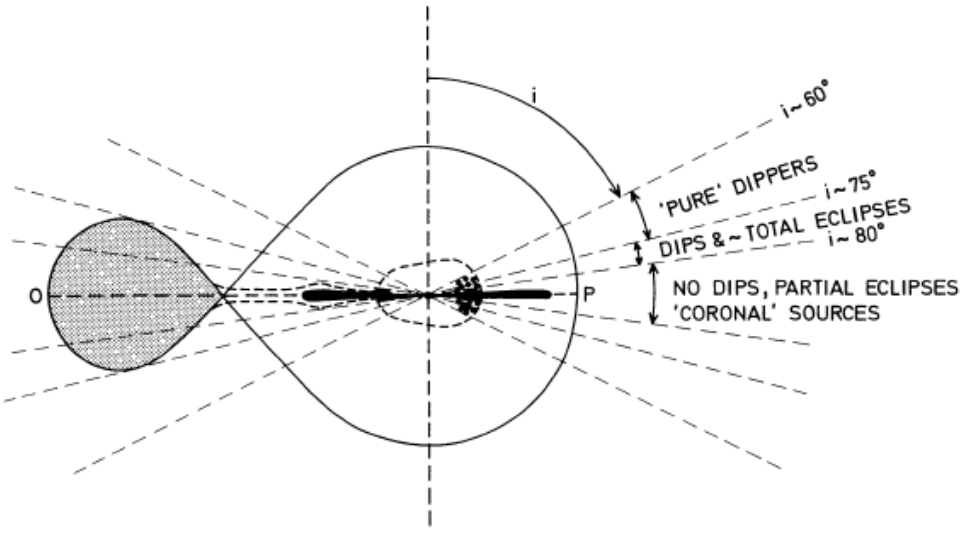

Figure 5.8: Ranges of inclinations corresponding to dips and eclipses. (Frank et al., 1987)

Dips can be generally observed in XRBs with inclination angles between and 60°–80°, while at high inclinations ($\geq 80°$) partial eclipses are observed when the companion obscures the compact object. Then, at $i \leq 60°$ no dips or eclipses are observed (Frank et al., 1987).

The XRT light curves were folded at the binary system period (∼14.7 hr), covering about ∼80% of this. I did not find any evidence for dips or eclipses. Further study on the *INTEGRAL*/JEM-X light curve (3-6 keV) collected during the 96 ks of *INTEGRAL* ToO when the source was in HS, was performed searching for any possible features. This light curve covered ≈100% of the binary period and even in this case no evidence of features indicative of a high inclination system for GRS 1716–249 were found, which is likely to be ruled out.
To estimate a possible, even though rough, value for the inner disc radius and the spin of the BH, I assumed an inclination angle upper limit $\vartheta < 60°$ (Frank et al., 1987). Using the inner disc radius R_c ∼15 km, I obtained an upper limit $R_{ISCO} < 21$ km. The lower limit on the BH mass ($M_{BH} > 4.9\,M_\odot$, Masetti et al., 1996) allowed me to estimate a lower limit on the gravitational radius as $R_g > 7.3$ km which results in a $R_{ISCO} < 3\,R_g$. In the Schwarzschild metric $R_{ISCO} = 6\,R_g$, therefore the black hole in GRS 1716–249 would be rotating with a spin lower limit of $a_* > 0.8$ (with a_* the dimensionless spin).
Recently, this result has been confirmed by Tao et al. (2019). These authors detected a broad relativistic iron line and a strong Compton hump from the *NuSTAR* data when GRS 1716–249 was in the hard intermediate state. Consistently with my results, they assumed that the accretion disc extended down to the ISCO. Fitting the *Swift*/XRT and *NuSTAR* broad band spectra with a KERBB+RELXILL model, they inferred a black hole spin $a_* > 0.92$ (consistent with my results) and an inclination angle of the system $\vartheta = 40°$-$50°$. Furthermore, Tao et al. (2019) found an upper limit on the black hole mass of about $8\,M_\odot$.
In order to place better constraints onto the inner disc radius and spin values, I made the calculation previously presented by using both the mass lower limit of $4.9M_\odot$ and the mass upper limit of $8\,M_\odot$, combined with the lower and upper limits on the inclination angle reported by Tao et al. (2019). Assuming $\vartheta = 50°$ and $M_{BH} = 4.9M_\odot$, I obtained an upper limit of $R_{ISCO} = 2.56\,R_g$, which implies a lower limit on the BH spin of 0.86. Similarly, assuming $\vartheta = 40°$ and $M_{BH} = 8M_\odot$, a lower limit $R_{ISCO} = 1.45\,R_g$ and an upper limit $a_* = 0.99$ can be derived.

5.3.4 Radio and correlation with X-rays

An important tool to investigate the emission properties of BHTs is the radio/X-ray correlation (see Paragraph 3.1.1).
In Figure 5.9, I show the radio/X-ray luminosity correlation combining data made available by Bahramian et al. (2018) and references therein[4]. All X-ray luminosities are calculated in the 1–10 keV energy range.

To this plot, I added a simultaneous XRT (in hard state, see Del Santo et al. 2016) and radio observation performed on MJD 56187.99 of the source Swift J174510.8–262411 (hereafter Swift J1745–26) which has been never taken into account in previous radio/X-ray luminosity correlation planes. I estimated a X-ray luminosity for Swift J1745–26 of $4.4 \times 10^{37}\,erg\,s^{-1}$ at a distance of 7 kpc (Muñoz-Darias et al., 2013) and I used the 5 GHz radio flux density from Curran

[4] https://github.com/arushton/XRB-LrLx_pub

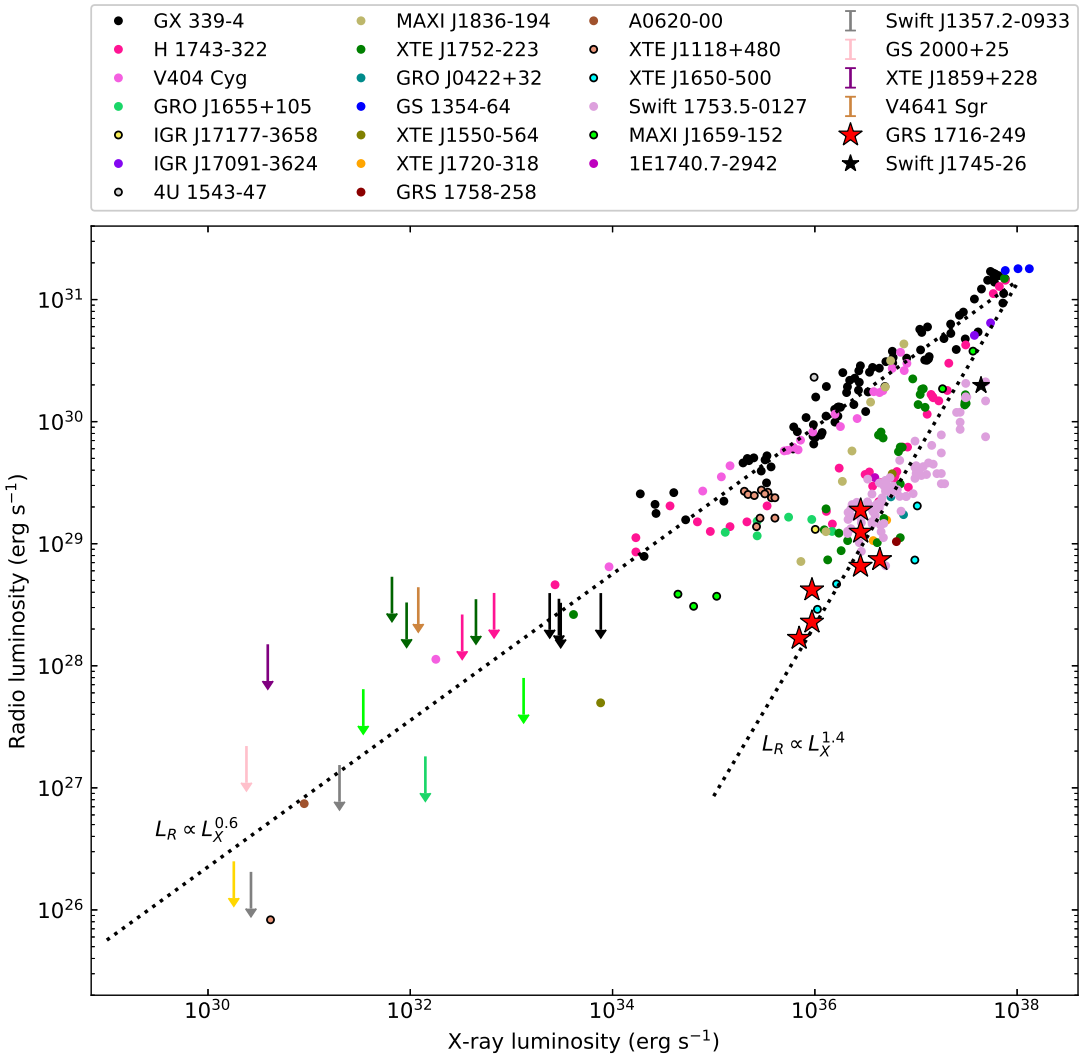

Figure 5.9: Radio/X-ray luminosity correlation. The X-ray luminosities have been calculated in the 1–10 keV energy range and the radio observations, collected at different frequencies, have been converted by Bahramian et al. 2018 to a common radio frequency, i.e. ∼5 GHz. GRS 1716–249 (red stars) is located on the radio-quiet branch. For this source I plotted radio observations performed both at ∼5 GHz and ∼9 GHz.

et al. (2014).
Then, I measured the X-ray flux of GRS 1716–249 in the 1–10 keV energy band, using data that were quasi-simultaneous with the radio observations performed at ∼5 GHz and ∼9 GHz (see Table 5.3). I estimated X-ray luminosities (d=2.4 kpc) of:

- 2.8×10^{36} erg s^{-1} on MJD 57793,
- 4.4×10^{36} erg s^{-1} on MJD 57805,
- 2.8×10^{36} erg s^{-1} on MJD 57865,
- 9.4×10^{35} erg s^{-1} on MJD 57977,
- 7.0×10^{35} erg s^{-1} on MJD 57978.

Both GRS 1716–249 and Swift J1745–26 are located on the steeper branch (slope 1.4) and they increase the number of radio-quiet BHTs.
The radio spectral indices of GRS 1716–249 measured by ATCA at the beginning ($\alpha = -0.15 \pm 0.08$ on MJD 57793.835) and close to the end of the outburst ($\alpha = -0.07 \pm 0.19$ on MJD 57977.256) by VLA are both consistent with a flat-spectrum compact jet, despite R_{in} being at the ISCO. It is worth noting that, it does not appear that GRS 1716–249 got soft enough to quench the compact jet and to create transient ejecta (Fender et al., 2004). The radio observations were performed when GRS 1716–249 was in HS-HIMS (see Table 5.3 and Figure 5.1 panel c). Therefore, it is not possible to exclude that the jet changed its properties when the X-ray emission became softer and that there were rapid ejection events, quenching or steepening episodes that have not been observed. However, based on the available data I observe that the source has never left the radio-quiet branch during the outburst, arguing against a quenching of the jet.
The power-law slopes of the radio spectra of GRS 1716–249, as also the radio slope of Swift J1745–26 ($\alpha \sim 0$; Curran et al., 2014), are within the statistical distribution of the radio-quiet slope reported by Espinasse & Fender (2018) (Section 3.1.1).
It was proposed that the origin of different radio loudness of BHTs are due to the geometric effects associated with the inclination of the sources: i.e the radio-quiet sources would be at high inclination (Motta et al., 2018). However, GRS 1716–249 is a radio-quiet system, and as discussed above, it is most likely seen at low inclination on account of the lack of observed dips or eclipses. Nevertheless dips can be transient as observed in H 1743–322 (Motta et al. 2015 and references therein), so the low inclination of GRS 1716–249 has to be confirmed.
The radio-quiet/X-ray-bright behaviour of the source can also be related to the very small inner disc radius that I inferred from my disc modeling. Indeed, the small inner disc radius does not necessarily imply the disc extends uninterrupted from its outer parts and down to the ISCO. Coupled disc/corona condensation evaporation models, developed in the framework of the truncated disc model, predict that when the sources are close to intermediate states, the inner hot-flow may re-condensate into an inner cool ring which would present observational signatures that are very similar to that of a full disc (Meyer-Hofmeister et al., 2009). Then, the contribution from the soft photons of the disc would make the accretion flow brighter in X-rays with respect to an accretion flow at the same accretion rate (and therefore radio luminosity) in which this mini inner-disc would be absent. Meyer-Hofmeister & Meyer (2014) argue that this could drive the different slope of the radio X-ray correlation of radio-quiet sources. The results on GRS 1716–249 appear to be consistent with their picture.

5.4 Conclusions

I have presented the X-ray spectral and timing analysis of the BHT GRS 1716–249 during its 2016-2017 outburst.
I analysed the XRT and BAT observations collected during the whole outburst occurred from December 2016 to October 2017. In addition, I have reported on five radio observations and their correlation with X-ray data. The main results of this study can be summarised as follows:

1) GRS 1716–249 can be added at the sample of the known BHTs that show a "failed" state transition outburst. During the outburst the source showed three softer episodes without making the transition to the soft state. Timing results and spectral parameters evolution are consistent with the source being in the HS at the beginning and at the end of the outburst, and in the HIMS during the spectral softening.

2) The data suggest that the inner disc might have reached the ISCO during the three softening episodes, even-though the source was in the HIMS. However, disc/corona condensation-evaporation models predict that in the intermediate state the hot accretion flow may re-condense into an inner mini-disc, mimicking the emission of the full disc.

3) The source might host a rapidly rotating BH with a rough estimation of the spin value between 0.86 and 0.99.

4) In the radio/X-ray luminosity plane GRS 1716–249 is located on the radio-quiet branch, which is in agreement with the X-ray brightness due to the condensed inner accretion flow.

Chapter 6

On the nature of the soft γ-ray emission in GRS 1716–249

In this chapter I focus on the high energy emission above 200 keV observed in the GRS 1716–249 spectrum when the source was in the bright hard spectral state. The multi-wavelength sampling (from the radio band to γ-rays) of the source gave me the opportunity to investigate the origin of this high energy emission through the application of different models. Such excess is usually interpreted as inverse Compton emission of the soft photons by a fraction of non-thermal electrons in the X-ray corona. In the following, I show the results of the X/γ-ray spectral fits, including the high energy tail, using the non-magnetised and magnetised hybrid thermal/non-thermal Comptonisation models EQPAIR and BELM, respectively.
Another scenario suggests that the high energy excess observed in hard states can originate from synchrotron emission in the radio jet. In order to test this hypothesis, I fitted the radio/γ-ray SED using an irradiated disc plus Comptonisation model combined with the jet internal shock emission model ISHEM. In the following, I discuss the possible combinations of jet parameters (electron distribution, half opening angle, jet inclination and jet power) with which it is possible to reproduce the high energy tail observed in the source hard state spectrum.

6.1 Observations and data reduction

On February 9, 2017 when GRS 1716–249 was in bright HS, a multi-wavelength campaign was performed offering a sampling of observations from radio to γ-rays. The source was simultaneously observed with ATCA, REM, *Swift* and *INTEGRAL*.
In this work I used the values of ATCA flux density 3.28 ± 0.05 mJy and 3.04 ± 0.03 mJy measured at 5.5 GHz and 9 GHz, respectively (see Table 5.3). Then, the radio spectral index $\alpha = -0.15 \pm 0.08$ was consistent with a flat-spectrum compact jet.

6.1.1 REM near-IR Observations

The observations of GRS 1716–249 were performed in a completely automated way with the IR camera REMIR (see Section 4.2) during the night of February 9, 2017 by acquiring one single observation in the J, H filters, and two points in the K filter. The final images have exposure times of 300 s, 150 s, and 75 s for the J, H and K filter, respectively. The final science frames were reduced and analysed using PSF–fitting photometry package DAOPHOT (Stetson et al., 1989; Stetson, 1994) and calibrated with the 2MASS survey. Table 6.1 shows the final results.

Date (TT)	JDMID	Exposure (s)	Filter	Magnitude/Flux
2017-02-09T07:47:00.384	57793.32466	300.0	J	14.18±0.22
2017-02-09T07:52:33.542	57793.32834	150.0	H	13.81±0.14
2017-02-09T07:56:11.098	57793.33077	75.0	K	13.84±0.29
2017-02-09T07:58:12.403	57793.33218	75.0	K	13.59±0.16

Table 6.1: REM start time in Terrestrial Time (TT) of the observations analysed. In the third and fourth columns the exposure and the filters are reported. In the last column I show the REM magnitude for each filter.

6.1.2 Swift Observations

On February 9, 2017 six observations were performed with the XRT and the UVOT telescopes on board *Swift* (for the telescopes description I refer to the Section 4.3.1).
I processed the XRT data using the FTOOLS software package in HEASoft v.6.26 and the *Swift* relative Calibration Database (CALDB). To correct the pile-up and to extract the source spectrum I adopted the criteria described in Sections 4.3.2.2 and 5.3.2, respectively. Due to the high Signal-to-Noise Ratio (SNR), I grouped the energy channels to have at least 50 counts per energy bin in order to apply the χ^2 statistics. It is known that residuals around the instrumental silicon (1.84 keV) and gold (2.2 keV) edges[1] affect the continuum of the source XRT spectra with good statistics. Averaging the six spectra of GRS 1716–249 the systematics due to these instrumental edges increase and dominate the final spectrum. Therefore, I decided to use only one of these six spectra. I have made sure that the spectral parameters and the fluxes of the 6 observations were consistent with each other, and I selected the pointing 00034924012.

By combining the 6 observations taken on February 9 we extracted an average power density spectrum (PDS), using custom software written in IDL[2]. It was adopted ≈29-s long intervals and a Nyquist frequency of ≈64 Hz, and from each interval a PDS in the energy band 0.4–10.0 keV was computed. Then the PDS

[1] https://heasarc.gsfc.nasa.gov/docs/heasarc/caldb/swift/docs/xrt/SWIFT-XRT-CALDB-09_v19.pdf
[2] GHATS, http://www.brera.inaf.it/utenti/belloni/GHATS_Package/Home.html

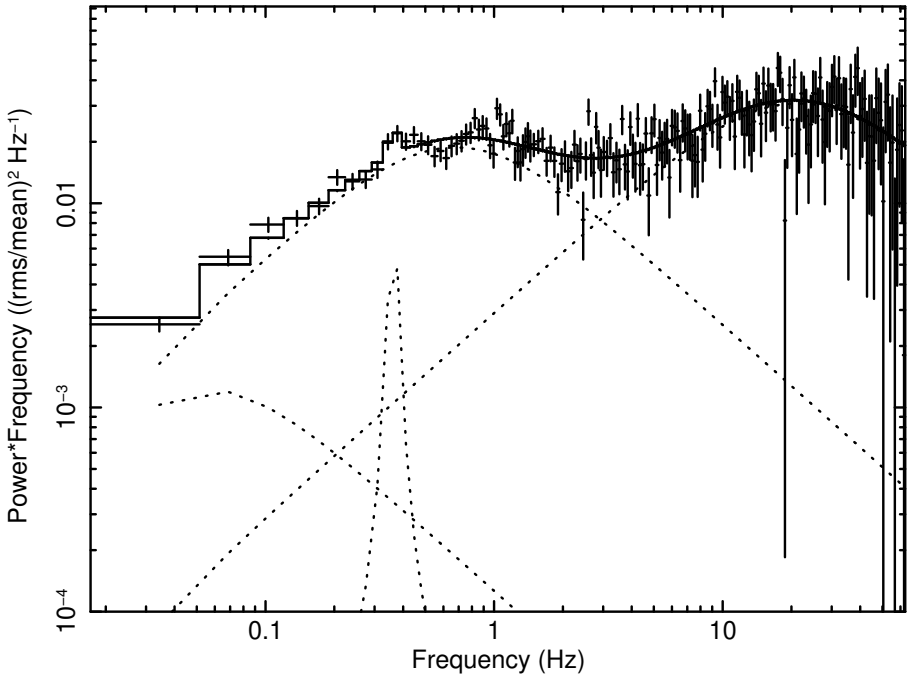

Figure 6.1: Average XRT PDS of the six pointings on February 9, 2017. They were fitted with three Lorentzians, of which two are zero-centred, plus a QPO.

Lorentzian Component	r	ν_0 (Hz)	Δ (Hz)	Q (Hz)
1	$0.1^{+0.01}_{-0.01}$	0	0.05	0
2	$12.69^{+0.95}_{-0.89}$	< 2.9	$20.95^{+2.72}_{-3.06}$	<0.07
3	$1.80^{+0.09}_{-0.10}$	0	$0.68^{+0.07}_{-0.06}$	0
4	$0.03^{+0.03}_{-0.06}$	$0.36^{+0.01}_{-0.01}$	$0.01^{+0.05}_{-0.02}$	14^{+27}_{-11}

Table 6.2: Results of the GRS 1716–249 average XRT PDS fitted with multiple Lorentzians, given individually by $P(\nu) = r^2/\pi[\Delta^2 + (\nu - \nu_0)^2]$ (Belloni et al., 2002). For each Lorentian, I report the integrated *rms* over the full range of $+\infty$ to $-\infty$ (r), the centred frequency ν_0 and its Half Width at Half Maximum Δ. In addition I show the frequency around which the component contributes most of its power Q=$\nu_0/(2\Delta)$.

were averaged and normalised according to the rms^2/Hz normalisation. In Figure 6.1 I show the total PDS fitted with a model constituted of three Lorentzians, two of which zero-centred. A fourth additional Lorentzian centred at 0.36 Hz (see Table 6.2) was used to model the QPO found at 2.9σ. In Table 6.2 I report the best fit (χ^2_r(dof)=1.01(178)) parameters.

The magnitudes and fluxes for each UVOT image were determined using the task *uvotsource*. A circular region of 5″ at the source coordinates and a larger region with no other source as background were selected.
In Table 6.3 I report the flux density calculated in different energy bands for each observation.

Filter	Exposure (s)	Flux Density
U	109	4.8± 0.5
B	109	6.5± 0.6
V	109	9.3± 1.0
UW1	217	1.68±0.34
UW2	436	< 1.19
UV2	339	< 1.46

Table 6.3: *Swift*/UVOT observation performed on 017-02-09T18:11:07 (MJD 57793.76) and analysed in this work. In the columns I report the filters, the exposures and the UVOT flux density in units of 10^{-16}erg/s/cm^2/A.

Afterwards, I selected the observations performed with the BAT telescope[3] from February 2 (MJD 57786) to March 15, 2017 (MJD 57827), during which the source flux was roughly constant in the hard X-ray band (see figure 5.1 and section 6.3.2). The data were processed using the BATIMMAGER software (Segreto et al., 2010) as described in the Section 4.3.2.3. I extracted the spectrum in 29 channels with logarithmic binning in the 15–185 keV energy range. Then, I used the official BAT spectral redistribution matrix.

6.1.3 INTEGRAL Observations

I analysed the *INTEGRAL*/SPI GRS 1716–249 data collected during the ToO campaign, in addition to the public observations performed from February 2 to March 15, 2017 (from revolution 1780 up to 1793).
I performed the SPI analysis using the SPIDAI tools[4] as explained in the section 4.3.3.1. I assumed a constant background during 12 Science Windows (SCWs). I determined the sky model for each revolution based on the maps of the individual IBIS/ISGRI SCWs and of the combined IBIS/ISGRI map. I selected the most significant sources ($\sigma \geq$10) present in the SPI FOV during each revolution (see Table 4.4). The sources' variability was defined using the IBIS/ISGRI light curves with a SCW binning time (1 SCW$\sim$1 hr).
I extracted the GRS 1716–249 SPI spectrum for each revolution in 39 channels in the 25–1000 keV energy range, requiring at least 2σ significance in the higher energy bins (i.e. $\geq$300 keV).

[3]The observations are available from the HEASARC public archive
[4]http://sigma-2.cesr.fr/integral/spidai

6.2 Broad band X/gamma-ray spectral results: the high-energy tail

I showed the spectral variability study of the XRT and BAT data in Section 5.4. I did not observe any significant variability in the emission of the source up to 150 keV from MJD 57786 to MJD 57827.
To investigate the variability above 150 keV, I fitted the SPI spectrum with a power law with a high energy exponential cut-off (*cutoffpl* in XSPEC) model

$$F(E) = kE^{-\Gamma}e^{-\frac{E}{kT_e}} \tag{6.1}$$

where Γ is the power-law photon index, kT_e the energy of the exponential cut-off expressed in keV and k is the model normalisation expressed in photons/keV/cm^2/s at 1 keV.

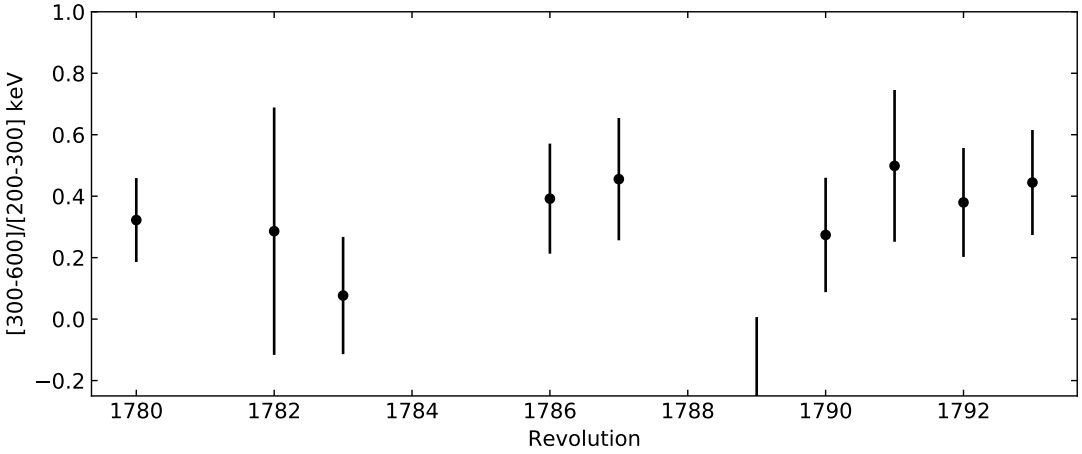

Figure 6.2: SPI hardness ratio [300–600] keV/[200–300] keV vs. revolution number.

I observed that the Γ and the kT_e values were consistent within the errors and the flux variability in the 25–300 keV energy band was lower than about 20%. I also checked any spectral variability in the energy range 200–600 keV and found that the hardness ratio [300–600] keV/[200–300] keV is constant (see Figure 6.2). Revolution 1789 is the only one that it is not consistent with the mean value of the HR. This is due to its lower exposure time combined with the different observing pattern.
Therefore, I used the averaged BAT and SPI spectra from MJD 57786 to MJD 57827 (February 2 to March 15, 2017) with the XRT pointing (MJD 57793.76) to perform the broad band spectral analysis in the larger energy range possible.

The spectra were fitted with XSPEC v. 12.9.1. All the errors reported are at the 90% confidence level. I introduced a systematic error of 2% in all the broad band spectra. In the fits I adopted the cosmic abundances of Wilms et al. (2000) and the cross-sections of Verner et al. (1996).
Even though I obtained a good χ^2 (χ^2_ν(dof)=1.05(336)) applying an absorbed

thermal Comptonisation model (TBABS plus NTHCOMP in XSPEC), I observed significant residuals above 200 keV. The addition of a power-law component at high energies allowed me to eliminate these residuals and improved the fit (χ^2_ν(dof) = 0.97(334)) with an F-test probability of 2.32×10^{-6}.
I found a hydrogen column density $N_H=0.70^{+0.02}_{-0.02}\times10^{22}\,cm^{-2}$, a photon index $\Gamma=1.68^{+0.01}_{-0.01}$ and an electron temperature $kT_e=50^{+4}_{-3}$ keV consistent with the values measured in the XRT and BAT broad band analysis (see Table 5.4). Then, I observed that a power law with $\Gamma=1.12^{+0.21}_{-0.63}$ reproduces the high energy excess above 200 keV and I obtained a flux of $2.5\times10^{-9}\,erg\,cm^{-2}\,s^{-1}$ in the 200–600 keV energy range.

6.2.1 Hybrid Comptonisation models

Below I show the results of the broad band spectral fits using the physical hybrid thermal/non-thermal Comptonisation models, i.e. EQPAIR and BELM. A description of these models is reported in Section 2.3.1.2.

6.2.1.1 Unmagnetised model

First, I fit the GRS 1716–249 X/γ-ray spectrum with the hybrid thermal/non-thermal Comptonisation model EQPAIR (Coppi, 1999). The emission of the disc/corona system is assumed to arise from a spherical, homogeneous and isotropic, cloud of hot ionised plasma with continuous injection of relativistic electrons illuminated by soft photons emitted by the accretion disc. I set the size of the Comptonising corona at $R\sim20\,R_g$, that corresponds to $R\simeq1.46\times10^7$ cm for GRS 1716–249. Since the source was in bright HS (see Figure 5.2) most of the luminosity comes from the corona and the contribution of the accretion disc is small or negligible (see Section 5.3.3). Following the assumption made in previous spectral analyses of Cyg X–1 and GX 339–4 (Gierliński et al., 1999; Del Santo et al., 2008, respectively) I fixed the soft photon compactness l_s, which is proportional to the luminosity of the thermal disc radiation entering the corona, to a value of 10. It is worth noticing that the predicted spectral shape is not sensitive to l_s but depends mostly on the compactness ratios: l_h/l_s and l_{nth}/l_h. Since the soft component is weak, constraining the seed photon temperature (kT_{max}) makes the fit unstable, so I kept this parameter frozen at a typical value observed in this state, i.e. 0.3 keV. The non-thermal electrons are injected with a power-law distribution $\gamma^{-\Gamma_{inj}}$ with a Lorentz factor γ in the range 1.3-1000. Because of the degeneracy of the parameters, following Del Santo et al. (2016), I fixed the slope of the electron distribution at the value $\Gamma_{inj}=2.5$ expected in shock acceleration models. Introducing a reflection component in the spectral model did not improve the fit significantly, therefore I fixed the reflection amplitude ($\Omega/2\pi$) at zero. In Figure 6.3, I show the best-fit model of the broad band spectrum. The best-fit parameters are reported in Table 6.4.
The best-fit hydrogen column density is compatible with the value obtained in the broad band spectral analysis using only XRT and BAT (see Table 5.4). The l_h/l_s values are close to those measured for other BHBs in bright hard and intermediate states: i.e. GX 339–4 (Del Santo et al., 2008), Cyg X–1 (Del Santo

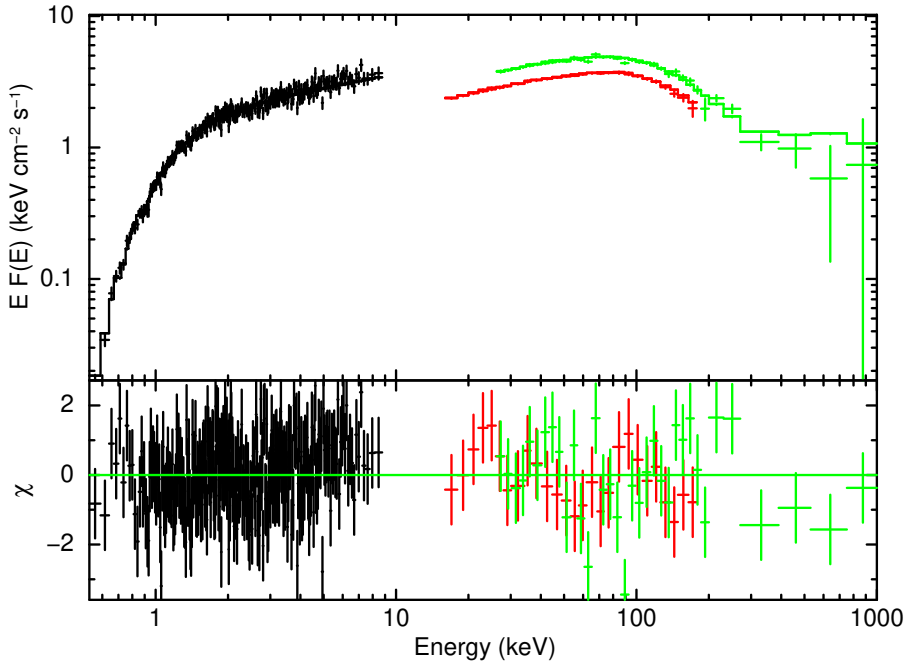

Figure 6.3: Broadband energy spectra of XRT pointing #12 (black points) with average BAT (red points) and SPI (green points) spectra in the simultaneous time interval (57792.968–57793.975 MJD) fitted with the EQPAIR model.

	l_h/l_s	l_{nth}/l_h	τ_p	τ_T	N_H (cm^{-2})	kT_e (keV)	Flux $\times 10^{-8}$ (erg cm^{-2} s^{-1})			χ^2_r(dof)
							Bol	Disc	Comp	
	(1)	(2)	(3)	(4)	(5)	(6)		(7)		(8)
EQPAIR	$9.69^{+0.31}_{-0.21}$	$0.57^{+0.04}_{-0.01}$	$1.79^{+0.08}_{-0.03}$	$\simeq$2.6	0.71 ± -0.01	$\sim$30	4.5	0.2	4.3	1.03(334)

Table 6.4: The best-fit parameters of the broadband XRT, BAT and SPI spectrum performed with an absorbed thermal/non-thermal Comptonisation (EQPAIR) model. (1) the total power provided to the electrons of the plasma over soft radiation coming from the accretion disc and entering in the corona, (2) the power in non-thermal electrons acceleration over the total power supplied to the plasma; (3) optical depth of ionisation electrons and (4) total Thomson optical depth, (5) hydrogen column density in units of 10^{22} cm^{-2}, (6) Comptonising electron temperature in keV, (7) unabsorbed bolometric flux (0.1–1000 keV), disc and Comptonised component fluxes, (8) reduced χ^2.

et al., 2013) and Swift J174510.8–262411 (Del Santo et al., 2016). The best-fit parameters suggest that about half of the total power is supplied to the plasma in the form of non-thermal electrons (see Tab. 6.4).

6.2.1.2 Magnetised model

The second hybrid thermal/non-thermal Comptonisation model I adopted to fit the GRS 1716–249 data is BELM (Belmont et al., 2008). As introduced in the

Section 2.3.1.2, in addition to the processes considered in EQPAIR, this model takes into account the magnetic field of the corona and the self-absorbed synchrotron emission.

I computed a table for a pure Synchrotron Self Compton (SSC) model, where the protons are cold (l_c=0), all the power is injected in the form of non-thermal particles and the external photons (i.e. from the disc) are negligible (l_s=0). Also in this model the spectral shape depends mostly on the ratio l_B/l_{nth} and is relatively insensitive to the value of the individual parameters. I fixed l_{nth}=10. Under this condition, the soft, self-absorbed synchrotron emission produced by the interaction between the non-thermal electrons and the magnetic field peaks around a few eVs. This component is then Compton up-scattered by the hybrid thermal/non-thermal electron distribution, extending the spectrum up to the X/γ-ray energies.
I obtained an acceptable χ^2_ν(dof)=0.94(341). The broad band spectrum and the different components' contribution to the model are shown in Figure 6.4. The hydrogen column density and the electron temperature are compatible with the values obtained with EQPAIR (N_H=$0.70^{+0.02}_{-0.02}\times10^{22}$ cm^{-2} and kT_e∼34 keV, respectively). In the BELM model, the electron acceleration index is better constrained, so I leave it free to vary, obtaining the best fit value Γ_{inj}=$2.64^{+0.20}_{-0.14}$. Then, I found a total optical Thompson depth of 3.3±0.1. Since the spectral shape is determined by the ratio l_B/l_{nth}, the best fit value of l_B highly depends on my choice of l_{nth}=10 and l_B does not represent the true magnetic compactness of the source. In order to estimate the magnetic field I need to rescale l_B to the real source compactness l_{obs}:

$$l_{\rm obs} = \frac{4\pi D^2 F \sigma_{\rm T}}{R m_e c^3} \tag{6.2}$$

estimated from its luminosity (see Del Santo et al., 2013). It can be expressed as:

$$l_{B,\rm obs} = \frac{l_B}{l_{\rm nth}} \frac{l_{\rm nth}}{l} l_{\rm obs} \tag{6.3}$$

It is worth noticing that l=l_{nth}+l_c+l_s. Since I am considering a case of pure SSC and purely non-thermal heating of the leptons, it results that l=l_{nth}. Thus, Equation 6.3 can be written as:

$$l_{B,\rm obs} = \frac{l_B}{l_{\rm nth}} l_{\rm obs} \tag{6.4}$$

Using the equations 2.37 and (6.4), I can estimate the magnetic field B in the limit of pure SSC emission:

$$B = \sqrt{\frac{l_B}{l_{\rm nth}} 32\pi^2 \frac{D^2 F}{cR^2}} \tag{6.5}$$

In the case where in addition to the synchrotron photons, soft photons from the disc represent a significant source of seed photons for the Comptonisation process, the efficiency of Compton cooling of the electrons in the corona is increased. Therefore, every other parameter being equal, the equilibrium temperature of the

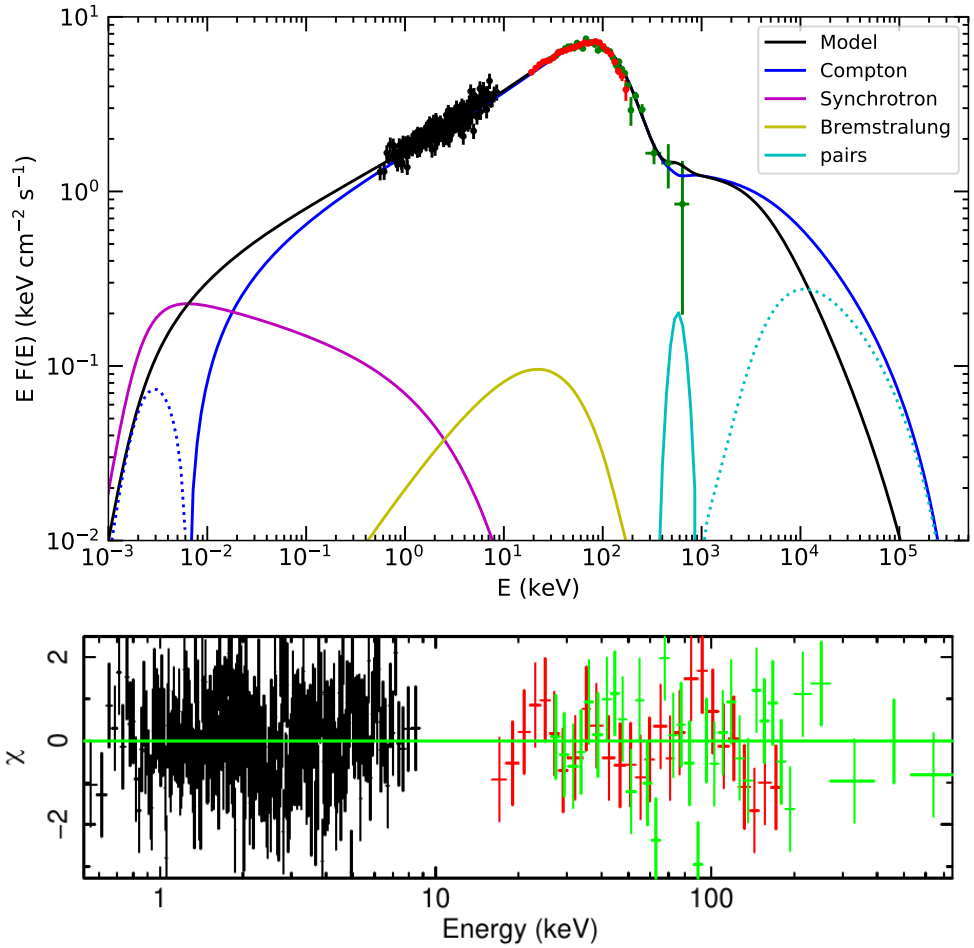

Figure 6.4: *Top:* Broadband energy spectra of XRT pointing #12 (black dots) with average BAT (red dots) and SPI (green dots) spectra in the simultaneous time interval (57792.968–57793.975 MJD) fitted with the BELM model. The total model (black line) correspond to fit of the broadband spectrum. The the positive (solid lines) and negative (dashed lines) components contribution to the spectrum: Compton (blue), Synchrotron (magenta), Bremmstrahlung (yellow) and pair annihilation/production (cyan). *Bottom:* Residuals obtained with magnetised model BELM by fitting XRT, BAT and SPI spectra.

thermal electrons is lower and a steeper Comptonisation spectrum with a lower energy cut-off is expected. In order to keep the model in agreement with the observed spectral shape, the Compton cooling needs to be reduced by cutting the amount of synchrotron seed photons. This can be achieved only by reducing the magnetic field. Therefore any model combining both disc and synchrotron photons would require a magnetic field that is lower than the one given by Equation 6.5.

Considering a pure SSC model, assuming a corona size of $R \sim 20\,\mathrm{R_g}$ (Del Santo et al., 2013) for a $M_{\mathrm{BH}} = 4.9\,M_{\odot}$ and using the measured bolometric flux F=$4.59 \times 10^{-8}\,\mathrm{erg\,cm^{-2}\,s^{-1}}$ in 0.1–1000 keV energy band and the best-fit value l_B/l_{nth}=$0.017^{+0.016}_{-0.006}$, using Equation 6.5 I calculated an upper limit on the magnetic field in the corona:

$\mathrm{B} < 1.5 \times 10^6 \left(\frac{20\,\mathrm{R_g}}{\mathrm{R}}\right)$ G.
At this point it is interesting to compare the observed magnetic field with the magnetic field in equipartition with the radiative energy density. The luminosity can be expressed as a function of the radiative energy density U_R, the volume of the sphere V and the photon escape time t_{esc}: i.e. $L = U_R V/t_{esc}$. Thus, the condition of equipartition between the magnetic field and the radiative energy density in the limit of low energy photons ($\mathrm{h}\nu < \mathrm{m}_e c^2$, Lightman & Zdziarski, 1987) is:

$$\frac{B_R^2}{8\pi} = U_R = \frac{L t_{esc}}{V} \tag{6.6}$$

where $t_{esc} \sim \left(1 + \frac{\tau_\mathrm{T}}{3}\right)\frac{R}{c}$. The magnetic compactness at the equipartition (l_{B_R}) can be obtained substituting Equation 6.6 in the magnetic field compactness (Eq. 2.37):

$$l_{B_R} = \frac{3l}{4\pi}\left(1 + \frac{\tau_T}{3}\right) \tag{6.7}$$

Therefore, the ratio between the observed magnetic field and the magnetic field in equipartition can be expressed in terms of compactness as:

$$\frac{l_{B,\mathrm{obs}}}{l_{B_R}} = \frac{l_B}{l_{nth}}\frac{l_{nth}}{l}\frac{\frac{4\pi}{3}}{1 + \frac{\tau_T}{3}} \tag{6.8}$$

Using the equation 6.8 and the best-fit parameters I calculated l_B/l_{B_R}=0.03 for GRS 1716–249.

6.3 Spectral energy distribution

6.3.1 Jet fitting procedure

To investigate whether the high energy excess of GRS 1716–249 can be explained as synchrotron emission from jets, I used the ISHEM model (Malzac, 2013, 2014). It takes as input a number of parameters related to the properties of the source, the jet and the distribution of the radiating particles. For a description of the model and its main parameters I refer to Section 3.2.2. Given a set of parameters I can compute a synthetic Spectral Energy Distribution (SED) using the observed X-ray PDS which is shown in Figure 6.1.
To fit the observed SED of GRS 1716–249 I followed these steps:

1) **Compute the synthetic SED.** In order to generate the synthetic jet SED I used the best fit parameters obtained for the average PDS (see Figure 6.1 and Table 6.2) in ISHEM and an initial set of parameters related to the source, jet and radiating particles' properties (see Section 3.2.2).
It is worth noting that if the X-ray QPO found in the PDS of GRS 1716–249 (see Figure 6.1) is a geometrical effect due to the accretion disc precession (Motta et al., 2015), it is not related to the intrinsic aperiodic variability of the accretion flow. Therefore, it should not be introduced in the model to simulate the shells propagation. However the QPO is weak (its significance

is 2.9σ, see Section 6.1.2) and its effect on the synthetic SED is negligible. Indeed, performing ISHEM simulations with and without the QPO shows that the resulting SEDs differ by no more than 4%. Such small difference does not affect the analysis. Therefore, in the next Section (6.3.2) I will show the results obtained including all the four PDS components in ISHEM.

2) **Fit the template SED.** Once I obtained the synthetic SED, I fitted the multi-wavelength data of GRS 1716–249 using the XSPEC local jet model named ISH with the break frequency and the break flux density as free parameters. This allowed me to compare the synthetic SED with the observed data and to quantify the shift in terms of frequency ($\Delta\nu$) and flux between the synthetic and the observed SED.

3) **Define the reasonable parameters combinations.** Based on the best fit normalisation and frequency shift parameters that I found, I defined a new set of physical parameters that resolve the flux normalisation and the break frequency equations (see Equations 3.7 and 3.8, respectively) by taking into account the required shifts.

It is worth noticing that in all the models I assume that the optically thin synchrotron power-law from the jet extends at least up to 1 MeV without any cooling break or high energy cut-off within the energy range covered by our observations. In the following I show the results of spectral fits with the index of the electron energy distribution, p, frozen to two different values: $p = 2.5$ and $p = 2.1$, which are both in the range of values expected in shock acceleration (Jones & Ellison, 1991).

6.3.2 Fitting results

I assembled the observed SED of GRS 1716–249from radio to γ-ray data collected during the multi-wavelength campaign.
To fit the whole SED with XSPEC, I created the spectra and the related pseudo-response matrix from the ATCA, REM, UVOT flux density and magnitudes (see Section 6.1 and Tables 6.1 and 6.3) running the task *ftflx2xsp*[5].
To fit the SED, I used the ISH model together with the irradiated disc model DISKIR (Gierliński et al., 2008) to describe the contribution of the accretion flow emission and with the models REDDEN (Cardelli et al., 1989) and TBABS to take into account the IR/optical and the X-ray interstellar absorption, respectively. The DISKIR model accounts for the irradiation of the outer disc and the reprocessing of the X-ray photons in the optical/UV band, in addition to the thermal Comptonisation in a hot corona. In table 6.5 I show the best-fit parameters. Note that the goodness of the fits is mainly driven by the X-ray data.
The best-fit hydrogen column densities, N_H, are in agreement with the values

[5]The *ftflx2xsp* FTOOL creates spectra and response files that can be read by XSPEC from an input text file of fluxes/magnitudes and errors. The response file created is a unit diagonal matrix.

obtained with my previous broad band spectral fits performed with the hybrid thermal/non-thermal models (see Section 6.2.1). Moreover, the E(B-V) values are in agreement with the value <E(B-V)>=0.9±0.2 reported by della Valle et al. (1994). The Comptonisation parameters Γ and kT_e are similar to those typically found in hard states (see e.g. Zdziarski & Gierliński, 2004; Done et al., 2007, and references therein). The ratio between the luminosity of the Compton tail with that of the unilluminated disc (L_c/L_d) is higher than 1 as expected in hard state spectra. The disc emission peaks in the UV band in agreement with what is expected for a disc truncated at large radii. The outer disc radius can be expressed in terms of the inner disc radius as $R_{out} \sim 10^{2.5-2.6}\, R_{in}$.

Jet emission component

	p=2.1	p=2.5
Shift	<-1.15	(-1.00)
N_H (10^{22} cm^{-2})	$0.65^{+0.02}_{-0.02}$	$0.67^{+0.02}_{-0.02}$
E(B-V)	$0.95^{+0.25}_{-0.02}$	$1.05^{+0.18}_{-0.20}$
kT_disk (10^{-2} keV)	$4.11^{+0.01}_{-0.02}$	$5.29^{+0.73}_{-0.77}$
Γ	$1.67^{+0.01}_{-0.01}$	$1.68^{+0.01}_{-0.01}$
kT_e(keV)	50^{+4}_{-3}	58^{+3}_{-3}
L_c/L_d	>2.02	$1.72^{+3.03}_{-0.70}$
fout ($\times 10^{-3}$)	$1.66^{+13.2}_{-1.5}$	>0.1
logrout	$2.54^{+0.24}_{-0.29}$	$2.56^{+0.31}_{-0.36}$
χ^2(dof)	1.01 (425)	1.06 (426)
γ_{min}	1	1
ϑ	15	15
Γ_{av}	4.5	4.5
ϕ	10.61	5.99
P_{jet} (L_E)	0.0447	0.0527

Table 6.5: Best-fit parameters of the Spectral Energy Distribution of GRS 1716–249 fitted with the irradiated disc (*diskir*) plus jet internal shock emission ISCHEM models for a black hole of 4.9 $M_\odot$ at 2.4 kpc and assuming a jet with an electron distribution p=2.5 and p=2.1.

As shown in Table 6.5, I obtained a good fit and reasonable jet and accretion flow parameters. However, the hard X-ray flux, as predicted by the ISHEM model with an electron distribution index p=2.5, underestimates the data by up to an order of magnitude, failing to reproduce the high energy tail detected with SPI (see top panel in Figure 6.5). As shown in the bottom panel of Figure 6.5, the adoption of a flatter electron energy distribution (p=2.1) makes the optically thin synchrotron emission harder and match the observed data: the jet emission can thus explain the high energy tail.
A possible combinations of jet parameters corresponding to the best-fit model

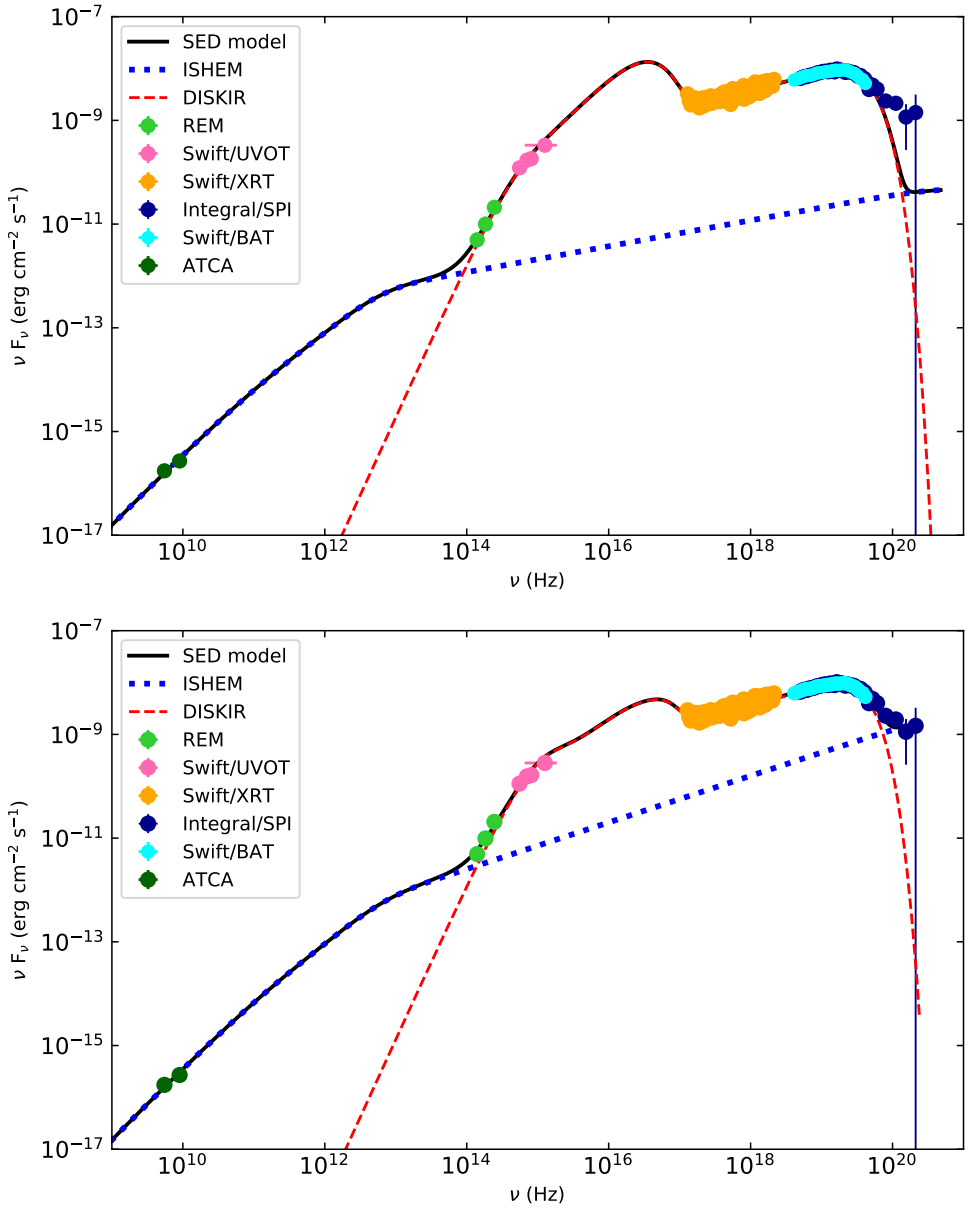

Figure 6.5: Spectral energy distribution of GRS 1716–249 built with the data collected during the multi-wavelength campaign performed on February-March 2017. To reproduce the observed high energy excess I used the ISHEM model assuming an electron distribution p=2.5 (upper panel) and p=2.1 (bottom panel). The total model *diskir+ish* is shown as a solid black line. The accretion disc contribution is modelled with DISKIR model and is shown as a dashed red line, while the blue dotted line represents the jet emission with ISHEM model.

are shown in Table 6.5. Of course, as mentioned in Section 3.2.2, the degeneracy between the parameters of ISHEM implies that many different combinations can fit the data equally well. For this reason the individual statistical uncertainty on each of these parameters is not meaningful and was not calculated. The degeneracy is illustrated in Figure 6.6. Each point in this figure represents a combination of jet parameters that produces the best-fit of the jet SED assuming $p = 2.1$. The

lines in the plot show how the jet power (P_{jet}) and the jet half-opening angle (ϕ) change to keep a constant SED when the jet bulk Lorentz factor Γ_{av} (blue dots lines in figure 6.6) or the inclination angle ϑ (green dots lines in figure 6.6) are varied keeping constant all the other parameters. In the case of the $p = 2.1$

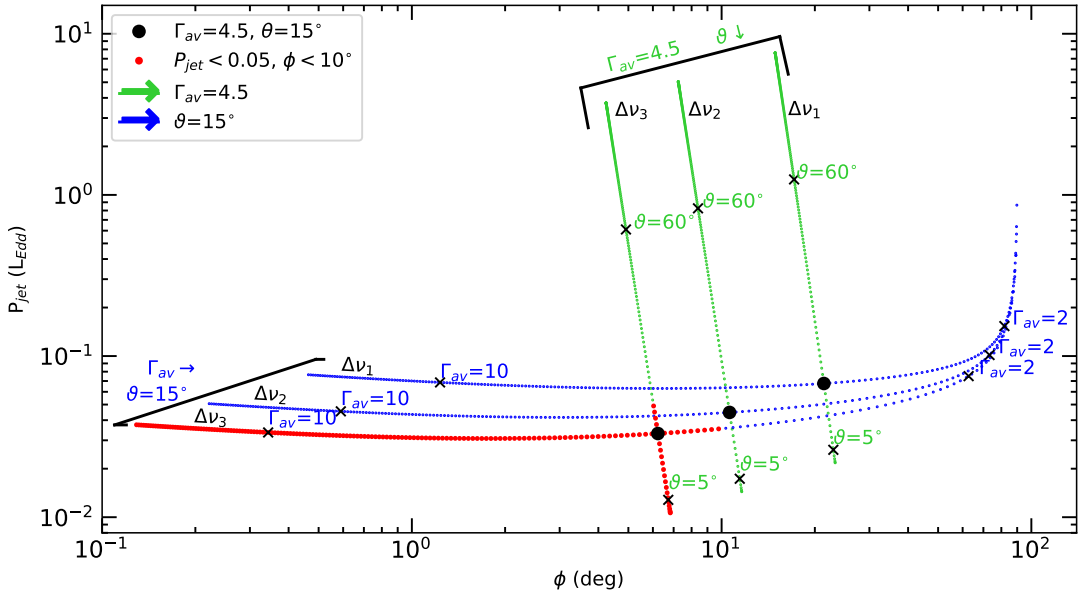

Figure 6.6: Evolution of the jet power (P_{jet}) versus the jet opening angle (ϕ) as a function of the mean Lorentz factor Γ_{av} and the jet inclination angle θ assuming $p = 2.1$. We investigated the possible parameters combinations assuming three SED frequency shifts between the synthetic and observed SED: $\Delta\nu_1$=$10^{-1.5}$, $\Delta\nu_2$=$10^{-1.3}$ and $\Delta\nu_3$=$10^{-1.15}$. For each $\Delta\nu$ we assumed a fixed Γ_{av}=4.5 and let ϑ free to vary from 60° to 5° (green dots). The blue dots are the evolution of P_{jet} versus ϕ, assuming a constant θ=15° and varying Γ_{av} in the range 1–10. The green and blue colour gradients show the increase of θ and Γ_{av}, respectively. The red dots are the combinations of θ and Γ_{av} for which we can obtain a collimated jet ($\phi \leq 10°$) with a jet power $P_{jet} \leq 0.05 L_{Edd}$.

model the XSPEC fit provided only an upper limit on the frequency shift $\Delta\nu$. In this case, the issue of degeneracy is even stronger and I have to account for combinations of parameters that correspond to lower values of frequency shifts than might produce statistically comparable fits. I found that, for a given ϑ and Γ_{av}, a smaller shift $\Delta\nu$ results in an increase of both ϕ and P_{jet} (black bullet in Figure 6.6). Figure 6.6 shows that, for a fixed $\Delta\nu$, small jet-opening angles (low ϕ) require large jet Lorentz factors (higher than a few). In this regime the jet power is rather insensitive to jet Lorentz factor and opening angle. A decrease of the mean Lorentz factor requires a larger jet-opening angle (high ϕ) with a slightly higher jet power (blue dots in Figure 6.6). When Γ_{av} decreases below 4.5 both the jet power P_{jet} and the opening angle ϕ significantly increase. When the jet opening angle exceeds $\sim$ 70°, the jet power must increase substantially to maintain the correct flux. When Γ_{av} $\sim$2, the jet opening angle reaches an almost constant value $\sim$100° and P_{jet} increases steeply. Decreasing ϑ at constant Γ_{av} implies slightly larger opening-angles and significantly lower jet power (green dots in Figure 6.6). Reasonably low power requires a small inclination.

Even though several parameter combinations can reproduce my data, not all of them are physically acceptable. Owing to the collimated nature of the jets, I favoured solutions corresponding to opening angles lower than 10° (Miller-Jones et al., 2006). The model of Körding et al. (2006) provides a simple estimate of the mean value of the jet power using the unabsorbed X-ray luminosity (see Drappeau et al., 2015; Péault et al., 2019):

$$P_{jet} \approx 43.6 \left[\frac{L_X}{L_{Edd}}\right]^{\frac{1}{2}} \%L_{\rm Edd} \tag{6.9}$$

The unabsorbed X-ray luminosity, $L_{[2-10\,keV]}$ ~0.01 $L_{\rm Edd}$, results in a jet power of about 0.05 $L_{\rm Edd}$. It is worth noticing that the Equation 6.9 is based on a number of assumptions (e.g. an inefficient accretion flow, the jet power corresponds to a constant fraction of the accretion rate, the variation of the accretion rate across the state transition is smooth and relatively slow) which are not necessarily true for GRS 1716–249. Therefore, we can only provide the order of magnitude of the jet power here.
In my analysis I favour solutions corresponding to half-opening angles in the range $\phi \leq$10° and $P_{\rm jet}$ lower than 0.05 $L_{\rm Edd}$. These constraints in turn favours jets with $\Gamma_{\rm av} \geq$4.5 and low jet inclination $\vartheta \leq$20° (red dots in figure 6.6).

Cooling spectral break

An important parameter with significant effects on the simulated SED, especially at high energies, is the cooling frequency spectral break in the synchrotron spectrum. This is due to the radiative cooling of the electrons during their propagation in the jet. The current version of the ISHEM model does not take into account the radiation losses and therefore does not account for the presence of the cooling break, even though the implementation of radiative cooling in the model is in progress.
For a complete analysis of the problem I refer to Péault (2019).
During the gas expansion in the jet, the electron distribution is induced to evolve under the influence of acceleration and cooling. The electrons are subject to two types of cooling: adiabatic cooling caused by the expansion of the jet in the interstellar medium, and radiative cooling caused by the emission of synchrotron photons. Assuming a constant injection of electrons described by a power law ($S = S_0\gamma^{-p}$) and constant adiabatic cooling during ejection, the electron distribution as a function of time t and of energy γ, can be written as:

$$N(t,\gamma) = \frac{S_0\tau_a}{p-1}\frac{\gamma^{-p}}{\frac{\tau_a\gamma}{\tau_s}+1}\left[1-\left(\frac{\gamma\tau_a}{\tau_s}e^{\frac{t_0-t}{\tau_a}}-1\right)^{p-1}\right] \tag{6.10}$$

where τ_a and τ_s are the adiabatic and synchrotron characteristic cooling times, respectively, and are defined according to the following relationships (Rybicki & Lightman, 1979; Péault, 2019):

$$\tau_a = \frac{3z}{2\Gamma_{av}\beta_{av}c} \tag{6.11}$$

$$\tau_s = \frac{6\pi m_e c}{\sigma_{\rm T} B_j^2} \tag{6.12}$$

where z is the position of the shock along the jet and $\beta_{av} = \sqrt{1 - \frac{1}{\Gamma_{av}^2}}$. Depending on the values chosen for τ_a and τ_s, different behaviours are observed. For $\tau_a \geq \tau_s$, synchrotron cooling is faster than adiabatic cooling and the latter does not have enough time to put itself in place. The electrons population behaviour changes significantly when adiabatic cooling becomes more efficient than radiation cooling ($\tau_a < \tau_s$). In this case adiabatic cooling dominates. This occurs at low energies causing the appearance of a cooling break at a frequency ν_{cool}. For $\nu < \nu_{cool}$ the population is dominated by adiabatic losses of energy, while at $\nu > \nu_{cool}$ electrons population is dominated by synchrotron losses.
From equation 6.10 it is possible to see that the electron energy at which the slope of the electron energy distribution changes is around:

$$\gamma_b(t) = \frac{\tau_s}{(p-1)\tau_a} \tag{6.13}$$

The ISHEM simulations provide the magnetic field profile along the jet and this allow to estimate the typical distance z at which most of the high energy synchrotron emission is produced and then to constrain the magnetic field in this region. From this we can estimate γ_b. The electrons at this energy produce synchrotron photons with a typical frequency:

$$\nu_c = \frac{3eB}{4\pi m_e c}\gamma_b^2 \tag{6.14}$$

which should correspond approximately to the observed frequency of the cooling break. From the above estimates and for the best-fit parameters given in Table 6.5 this is expected at around 10 keV ($\sim 10^{18}$ Hz). Although it might still be possible to reproduce the excess with jet synchrotron emission, this would require a harder index for the electron distribution ($p \leq 2$) in order to fit the observed high-energy excess. Such a hard electron distribution is difficult to reconcile with the standard shock acceleration mechanisms.

6.4 Conclusions

I have presented the analysis of the X/γ-ray broad band spectra and the Spectral Energy Distribution of the BHT GRS 1716–249 during its bright hard state which occurred in February–March, 2017. Similarly to what has previously been observed in several other sources, I detected the presence of a spectral component above 200 keV in excess of the thermal Comptonisation spectrum. The simultaneous multi-wavelength data collected when GRS 1716–249 was in outburst provide a good laboratory to explore the possible origin of this excess. In order to investigate the possible origin of this component I applied different models. In particular, I fitted the source X/γ-ray spectrum with both the unmagnetised (EQPAIR) and the magnetised (BELM) hybrid Comptonisation models. The fits

showed that non-thermal Comptonising electrons can be responsible for the excess above 200 keV. Overall the results agree with those obtained for other BHBs: GX 339–4 (Del Santo et al., 2008), Cyg X–1 (Malzac & Belmont, 2009; Del Santo et al., 2013), Swift J174510.8–262411 (Del Santo et al., 2016). The best-fit with BELM models in the limit of pure SSC, allowed me to place an upper limit onto the magnetic field of the corona of about $1.5\times10^6 \left(\frac{20\,R_{\rm g}}{R}\right)$ G. Furthermore, I found that the energy density of the magnetic field is not sufficient to explain the observed radiation. In fact, the U_B/U_R ratio (in terms of compactness) shows that the system is in a condition of sub-equipartition. A similar behaviour was also observed for Cyg X–1 in HS (Malzac, 2012; Del Santo et al., 2013).

The results from Sobolewska et al. (2011) indicate that for luminosities higher than $\sim$1% $L_{\rm Edd}$ the disc should supply the main seed photons contribution, while at lower luminosities synchrotron seed photons should dominate. The transition between these two regimes of Comptonisation occurs around a luminosity that is comparable to the measured bolometric luminosity of GRS 1716–249 ($L\sim0.01\,L_{\rm Edd}$). Indeed, I observed that the Comptonised spectrum of GRS 1716–249 can be explained without soft seed photons from the accretion disc. If there would be a significant contribution from the soft disc photons to the Comptonisation process, the magnetic field value should be significantly lower than the upper limit of $1.5\times10^6 \left(\frac{20\,R_{\rm g}}{R}\right)$ G I obtained in the hypothesis of pure synchrotron seed photons (assuming $R=20\,R_{\rm g}$).

I also investigated whether this soft γ-ray emission could be due to the jet. Fitting the SED of GRS 1716–249 (from radio to γ-rays) with the internal shock emission model ISHEM, in which the shocks are driven by the accretion flow variability, I found that the jet synchrotron emission could explain the soft-γ rays emission if the index of the electron distribution is flat enough ($p \simeq 2.1$). My results support a jet with an average bulk Lorentz factor ($\Gamma_{\rm av}$) higher than 4.5 and a maximum jet inclination angle of 20°, assuming reasonable values of jet opening angle ($\phi \leq 10°$, see Miller-Jones et al., 2006). The $\Gamma_{\rm av}$ I have found for GRS 1716–249 is higher than the upper limit on the bulk Lorentz factors of 2 generally assumed for the $L_X \propto L_R^{0.7}$ correlation (Gallo et al., 2003). Although the constraints on the bulk Lorentz factors of compact jets are few, it was shown that this correlation does not exclude high bulk Lorentz factors for BHBs jets (Heinz & Merloni, 2004). Miller-Jones et al. (2006) showed that XRBs can produce relativistic jets with bulk speeds up to $\Gamma_{\rm av} \sim 10$, similarly to what is found in AGNs. In any case, direct constrains on this parameter have been reported in only a few cases. From the IR/X-ray lags Casella et al. (2010) inferred a lower limit $\Gamma_{\rm av} \geq 2$ for GX 339–4 , while Tetarenko et al. (2019) constrained a $\Gamma_{\rm av} \sim 2.6$ for Cyg X–1 through the radio timing analysis. Additional constrains have been reported recently by Saikia et al. (2019); the authors studied a sample of nine BHBs observing that the bulk Lorentz factor lies in the range 1.3–3.5.

The position of the high energy cooling break in the synchrotron spectrum may give important information on the nature of the high energy emission in the HS of BHBs, i.e. if this emission is dominated by the synchrotron from the jet or

by the non-thermal Comptonisation process in the corona. However, the evidence for the presence of such break is still poor since it is usually hidden beneath other components. It has been directly detected only in MAXI J1836–194 (Russell et al., 2014). The fitting assumption I have done to extend the optically thin part of jet spectrum in GRS 1716–249 up to 1 MeV implies that the cooling break is at higher energies, which looks quite unlikely. I derived the cooling break being about 10 keV. This would imply a harder index of the electron distribution ($p \leq 2$) which is more difficult to reconcile with standard shock acceleration mechanisms. This seems to disadvantage the hypothesis of the jet emission as origin for the excess above 200 keV over the non-thermal Comptonisation process.
Similar results were obtained by Zdziarski et al. (2014b) who modelled the γ-ray emission of Cyg X–1 using a different jet model (Zdziarski et al., 2014a). The good constraints at MeV energies and the Fermi-LAT detection of γ-ray emission (Malyshev et al., 2013; Zdziarski et al., 2017) from Cyg X–1 made it possible to study the high energy emission of the source applying a self-consistent jet model which takes into account all the main emission processes (Zdziarski et al., 2014a,b). In accord with the measurement of strong linear polarization of Cyg X–1 at MeV energies (McConnell et al., 2002; Laurent et al., 2011; Jourdain et al., 2012; Rodriguez et al., 2015), Zdziarski et al. (2014b) showed that it is possible to associate the observed MeV emission to the synchrotron jet emission. However, the model requires an efficient particle acceleration and a hard electron index ($p \sim 1.5$) which led to the formation of a flat synchrotron spectrum able to model the MeV tail (Zdziarski et al., 2014b) but is difficult to reconcile with the shock acceleration mechanisms. In addition, the jet magnetic field has to be above the equipartition level not to produce an excess of emission at GeV energies (Zdziarski et al., 2014b). Thus, the non-thermal Comptonisation process within the corona seems more likely than the jet synchrotron as the nature of the soft γ-ray emission in GRS 1716–249, unless alternative acceleration mechanisms are invoked.

Chapter 7

Conclusions

The research topic of my thesis concerns the study of the accretion/ejection processes and their connection in transient Low Mass X-ray Binary systems hosting a black hole.
The X-ray observations performed on the Galactic black hole transient GRS 1716–249 during the whole 2016-2017 outburst allowed me to place constraints onto the physical processes and geometry of the accretion flow. Indeed, among the most important open questions about black hole transients, my research has been focused on the investigation of the accretion flows geometry in bright hard states, the physical parameters triggering the spectral transition and why some black hole transients do not make the transition to the soft states.

Studying the X-ray emission of GRS 1716–249 across the spectral states I could constrain the geometry of the system. Coherently with a scenario in which the disc moves closer to the compact object during the spectral transitions from hard to soft state, I observed that the inner disc radius in GRS 1716–249 decreased as the inner disc temperature increased, until a certain point where the temperature continued to increase at a constant radius. I found evidence of the accretion disc extending down to the innermost stable circular orbit in the hard intermediate state and not in the soft state as expected. Another possibility is that the hot accretion flow has been re-condensed into an inner mini-disc, mimicking the emission of the full disc (Meyer-Hofmeister et al., 2009). Furthermore, I estimated a lower limit on the black hole spin which indicates that the source might host a rapidly rotating black hole. However, it is worth noticing that my estimates both on the inner accretion disc radius and the spin of the source are rough. Indeed, due to the low statistics of the XRT spectra I could only use a simple model for the disc emission (DISKBB) of the source. Recently, Tao et al. (2019) confirmed my spin estimation thanks to the detection of the iron line in the spectrum of GRS 1716–249 obtained with an observation performed with *NuSTAR*. The moderate spectral resolution provided by *NuSTAR*, let them use reflection models to fit the spectra. Nevertheless, this telescope is not designed to perform monitoring campaigns. Thus, a study of the spectral evolution along the outburst like the one I did with *Swift* would not have been possible with *NuSTAR*. Future missions like *Athena* will combine large effective area and high spectral resolution to perform more accurate measurements of black hole spin and

accretion disc parameters (i.e. inner disc radius and inclination of the system) following their variability. However, the measurements based on the spectral analysis are in any case model dependent. Further techniques can be used to study the geometry of the accretion flow, e.g. the reverberation mapping using the timing analysis performed with *NICER*.

The study performed on a larger sample of black hole transients by Tetarenko et al. (2016) shows that the "failed" state transition behaviour of GRS 1716–249 keeps out to be an isolated case. This "unexpected" behaviour, could be led by the low mass accretion rate involved during the outburst, which might not be high enough to trigger the transition to the soft state. However, sources as Swift J1745–26 did not make the transition to the soft states (Del Santo et al., 2016) even though they are bright (peak luminosity $> 0.11\,L_{Edd}$). This suggests that other parameters may play an important role in the occurrence of the state transition. Further studies are necessary to understand which physical parameters are involved in the spectral transition and how they trigger it.

Another issue that I investigated is the nature of the connection between accretion and ejection processes. The radio observations performed during the outburst of GRS 1716–249 show that the source can be added to the even larger group of radio-quiet sources (namely "outliers"). Then, the slightly negative radio spectral index of GRS 1716–249 falls in the statistical distribution of the radio-quiet sources. The possible explanations are that either these black hole transients have different properties in the compact jets (Espinasse & Fender, 2018) or the efficiency of their accretion flow (Coriat et al., 2011) with respect to that in radio-loud black hole transients. Recently, it was also suggested that geometric effects such as the inclination of the binary system (Motta et al., 2018) can explain the different radio/X-ray correlations. High angular resolution radio observations (e.g. performed with the VLBI) of the jets of black hole transients might be a key tool to measure the jet inclination. Finally, the behaviour of GRS 1716–249 suggests the formation of an inner mini-disc in the intermediate state.

Similarly to what has been observed in other sources, I evidenced the presence of a high energy component above 200 keV in excess of the thermal Comptonised emission in the bright hard state spectrum of GRS 1716–249. According to what has been proposed for GX 339–4 (Del Santo et al., 2008), Cyg X–1 (Malzac & Belmont, 2009; Del Santo et al., 2013), Swift J1745–26 (Del Santo et al., 2016), inverse Compton scattering of the soft disc photons by non-thermal electrons (Poutanen & Coppi, 1998; Coppi, 1999; Gierliński et al., 1999) could be responsible for the soft γ-ray emission (above 200 keV) observed in the hard state spectrum of GRS 1716–249. However, the detection of a strong linear polarisation in Cyg X–1 (Laurent et al., 2011; Jourdain et al., 2012) above 400 keV supports the hypothesis that jet synchrotron emission could contribute significantly to the soft γ-rays. To test this idea, I used the jet internal shock emission model (ISHEM, Malzac (2013)) to model the spectral energy distribution of GRS 1716–249. I found that it is not possible to reproduce the observed MeV excess with the jet model unless the index of the electrons is very hard ($p < 2$), which is quite unlikely. Similar conclusions were obtained by Zdziarski et al. (2014b) from the modelling of the high energy emission of Cyg X–1 using a different model.

Thus, my results seem to disfavour the jet scenario for the soft γ-ray emission of GRS 1716–249.
Simultaneous and repeated measurements at different wavelengths, with a good coverage along the full electromagnetic spectrum, are crucial to constrain the jet ISHEM model. In particular, observations performed with satellites such as *SVOM* at IR, visible and hard X-ray energies, would help to have a complete view of the jet physics and to improve our knowledge on the jet/accretion flow coupling. Furthermore, spectra characterised by high statistics over a wide X-ray energy range (e.g. the spectra provided by the recently launched HXMT satellite) would allow to constrain the high-energy cut off in the thermal Comptonised spectrum and to follow its evolution along the outburst. Measurements of X-ray and soft γ-ray polarisation would place strong constraints onto the emission processes and geometry of the accretion flow and the jet in the hard state of black hole binaries.

Conclusion

Le sujet de ma thèse concerne l'étude des processus accrétion/éjection dans les systèmes binaires transitoires X de faible masse hébergeant un trou noir.
Les observations en rayons X effectuées sur la transitoire à trou noir galactique GRS 1716–249 durant toute l'éruption de 2016-2017 m'ont permis de donner des contraintes sur les processus physiques et la géométrie du flot d'accrétion. En effet, parmi les questions ouvertes les plus importantes sur les transitoires du trou noir, mes recherches se sont concentrées sur l'étude de la géométrie du flot d'accrétion dans les états spectraux durs brillants, sur les paramètres physiques déclenchant la transition spectrale et la raison pour laquelle certaines transitoires à trou noir ne font pas la transition vers les états mous.

En étudiant l'émission X de GRS 1716–249 dans différents états spectraux, j'ai pu contraindre la géométrie du système. En cohérence avec un scénario dans lequel le bord interne du disque se rapproche de l'objet compact au cours des transitions spectrales de l'état dur vers l'état mou, j'ai observé que le rayon interne du disque dans GRS 1716–249diminuait à mesure que la température du disque interne augmentait, jusqu'à un certain point à partir duquel, la température a continué d'augmenter à rayon constant. J'ai montré que le disque d'accrétion s'étend jusqu'à la dernière orbite circulaire stable dès l'état intermédiaire dur et non à l'état mou comme on le pensait généralement jusqu'ici. Une autre possibilité est que le flot d'accrétion chaud se soit re-condensé en un mini-disque interne, imitant l'émission du disque complet (Meyer-Hofmeister et al., 2009).
De plus, j'ai fourni une limite inférieure sur la rotation du trou noir qui indique que la source pourrait héberger un trou noir en rotation rapide. Cependant, il convient de noter que mes estimations du rayon interne du disque d'accrétion et du spin du trou noir sont approximatives. En effet, du fait des faibles statistiques des spectres XRT, je n'ai pu utiliser qu'un modèle simple pour l'émission du disque (DISKBB). Récemment, Tao et al. (2019) a confirmé mon estimation de spin grâce à la détection de la raie du fer dans le spectre de GRS 1716–249 obtenue avec une observation réalisée avec *NuSTAR*. La résolution spectrale modérée fournie par *NuSTAR* leur a permis d'utiliser des modèles de réflexion pour ajuster les spectres observés. Néanmoins, ce télescope n'est pas conçu pour effectuer des campagnes de suivis de sources. Ainsi, une étude de l'évolution spectrale le long de l'eruption comme celle que j'ai faite avec Swift n'aurait pas été possible avec *NuSTAR*. Les futures missions comme Athena combineront une grande surface effective et une haute résolution spectrale pour effectuer des mesures plus précises de la rotation du trou noir et des paramètres du disque d'accrétion (c.-à-d. rayon du disque interne et inclinaison du système) et suivre leur évolution.

Cependant, les mesures basées sur l'analyse spectrale sont sensibles au modèle utilisé. D'autres techniques peuvent être utilisées pour étudier la géométrie du flot d'accrétion: par ex. la cartographie par réverbération en utilisant l'analyse temporelles possibles par exemple avec *NICER*.

L'étude réalisée sur un plus grand échantillon de transitoires à trous noirs par Tetarenko et al. (2016) montre que le comportement de transition d'état "échoué" de GRS 1716–249 n'est pas un cas isolé. Ce comportement "inattendu" pourrait être relié au taux d'accrétion de masse atteint lors de l'éruption, qui n'est peut être pas suffisant pour déclencher la transition vers l'état mou. Cependant, des sources telles que Swift J1745–26 n'ont pas effectué la transition vers les états mous (Del Santo et al., 2016) alors qu' elles sont lumineuses (luminosité maximale $> 0.11\,L_{Edd}$). Cela suggère que d'autres paramètres peuvent jouer un rôle important dans l'occurrence de la transition d'état. Des études supplémentaires sont nécessaires pour comprendre quels paramètres physiques sont impliqués dans la transition spectrale et comment ils la déclenchent.

Un autre problème que j'ai étudié est la nature du lien entre les processus d'accrétion et d'éjection.
Les observations radio effectuées au cours de l'eruption de GRS 1716–249 montrent que la source peut être ajoutée au groupe toujours plus grand des sources radio-silencieuses. Ensuite, l'indice radio-spectral légèrement négatif de GRS 1716–249 tombe dans la distribution statistique des sources radio-silencieuses. Les explications possibles sont que ces transitoires à trou noir ont des propriétés de jet différentes (Espinasse & Fender, 2018) ou des différences d'efficacité radiative du flot d'accrétion (Coriat et al., 2011) par rapport aux transitoires à trous noirs radio-fortes.
Récemment, il a également été suggéré que des effets géométriques tels que l'inclinaison du système binaire (Motta et al., 2018) peuvent expliquer les différentes corrélations radio/X. Des observations radio à très haute résolution angulaire de jets de transitoires à trous noirs (par exemple effectuées avec le VLBI) pourraient être un outil clé pour mesurer l'inclinaison du jet. Enfin, le comportement de GRS 1716–249 suggère la formation d'un mini-disque interne dans les états les plus lumineux.

De manière similaire à ce qui a été observé dans d'autres sources, j'ai mis en évidence, dans le spectre d'état dur brillant de GRS 1716–249, la présence d'une composante de haute énergie au delà de 200 keV, en excès par rapport à l'émission de comptonisation thermique. Selon ce qui a été proposé pour GX 339–4 (Del Santo et al., 2008), Cyg X–1 (Malzac & Belmont, 2009; Del Santo et al., 2013), Swift J1745–26 (Del Santo et al., 2016), la diffusion Compton inverse des photons mous du disques par des électrons non-thermiques (Poutanen & Coppi, 1998; Coppi, 1999; Gierliński et al., 1999)) pourrait être responsable de l'émission au-dessus de 200 keV. Cependant, la détection d'une forte polarisation linéaire dans Cyg X–1 (Laurent et al., 2011; Jourdain et al., 2012) au-dessus de 400 keV soutient l'hypothèse selon laquelle l'émission synchrotron du jet pourrait contribuer de manière significative aux gammas mous. Pour tester cette idée, j'ai utilisé le modèle d'émission de choc interne du jet (ISHEM, Malzac (2013)) pour modéliser la distribution spectrale d'énergie de GRS 1716–249. J'ai trouvé qu'il

n'est pas possible de reproduire l'excès de MeV observé avec le modèle de jet à moins que l'indice de la distribution en énergie des électrons soit très dur ($p < 2$), ce qui est peu probable. Des conclusions similaires ont été obtenues par Zdziarski et al. (2014b) à partir de la modélisation des émissions à haute énergie de Cyg X–1 à l'aide d'un modèle différent. Mes résultats semblent donc défavoriser le scénario du jet pour l'émission de rayons γ doux du GRS 1716–249.
Des mesures simultanées et répétées à différentes longueurs d'onde, avec une couverture complète du spectre électromagnétique, sont cruciales pour contraindre le modèle d'émission de jet ISHEM. En particulier, des observations réalisées avec des satellites tels que SVOM aux énergies IR, visible et rayons X durs, permettraient d'avoir une vision complète de la physique des jets et d'améliorer nos connaissances sur le couplage jet/accrétion.
De plus, des spectres haute énergie caractérisés par une statistique élevée dans une large bande (par exemple les spectres fournis par le satellite HXMT récemment lancé) permettraient de contraindre la coupure à haute énergie dans le spectre de comptonization thermique et de suivre son évolution au cours de l'éruption.
Les mesures de la polarisation en rayons X et γ mous fourniraient de fortes contraintes sur les processus d'émission et la géométrie du flot d'accrétion et du jet dans l'état dur des binaires à trous noirs.

Appendix A

List of refereed and non refereed publications

A.1 Publications

- *On the nature of the soft γ-ray emission in the hard state of the black hole transient GRS 1716–249*
  T. Bassi, J. Malzac, M. Del Santo, E. Jourdain, J.-P. Roques, A. D'Aì, J.C.A. Miller-Jones, R. Belmont, S.E. Motta, A. Segreto, V. Testa, P. Casella
  MNRAS accepted

- Broadband spectral analysis of MXB 1659-298 in its soft and hard state.
  Iaria R.; Mazzola S.; **Bassi T.**; Gambino A. F.; Marino A.; Di Salvo T.; Sanna A.; Riggio A.; Burderi L.; D'Amico N. (2019)
  A&A, 630, A138
  doi:10.1051/0004-6361/201833982

- Broadband spectral analysis of MXB 1659-298 in its soft and hard state.
  Mazzola S.; Iaria R.; Gambino A. F.; Marino A.; Di Salvo T.; **Bassi T.**; Sanna A.; Riggio A.; Burderi L.; D'Amico (2019)
  Proceedings of the 12th INTEGRAL conference and 1st AHEAD Gamma-ray Workshop, Geneva (Switzerland), 11-15 February 2019

- The long outburst of the black hole transient GRS 1716–249observed in the X-ray and radio band.
  T. Bassi, M. Del Santo, A. D'Aì, S.E. Motta, J. Malzac, A. Segreto, J.C.A. Miller-Jones, P. Atri, R.M. Plotkin, T.M. Belloni, T. Mineo, A.K. Tzioumis (2019)
  MNRAS, Vol. 482, Issue 2, p.1587-1601
  doi:10.1093/mnras/sty2739

- The Long Outburst of the Black Hole Transient GRS 1716–249
  T. Bassi, M. Del Santo, A. D'Aì S.E. Motta, J. Malzac, A. Segreto, J.C.A. MillerJones, P. Atri, R.M. Plotkin, T.M. Belloni, T. Mineo, A.K. Tzioumis (2018)

SF2A-2018: Proceedings of the Annual meeting of the French Society of Astronomy and Astrophysics
https://ui.adsabs.harvard.edu/abs/2018sf2a.conf..225B

- Faint γ-ray sources at low-redshift: the radio galaxy IC 1531
T. Bassi, G. Migliori, P. Grandi, C. Vignali, M. A. PÃÍrez-Torres, R. D. Baldi, E. Torresi, C. Stanghellini (2018)
MNRAS, Vol. 481, Issue 4, p.5236-5246
doi:10.1093/mnras/sty2622

A.2 Posters

Posters presented during conferences:

- *The long outburst of the black hole transient GRS 1716–249*
Tiziana Bassi, Melania Del Santo, Julien Malzac, Antonello D'Aì, Sara Elisa Motta, Alberto Segreto, James C.A. Miller-Jones, Tomaso Belloni, Piergiorgio Casella, Vincenzo Testa, Teresa Mineo (2019)
X-ray astronomy 2019 - Current challenges and new frontiers in the next decade, 8-13 September 2019
https://indico.ict.inaf.it/event/720/contributions/5513/

- *The origin of the high energy excess observed during the hard state of the outburst of the black hole transient GRS 1716–249*
Tiziana Bassi, Melania Del Santo, Julien Malzac, Antonello D'Aì, Sara Motta, Piergiorgio Casella, Vincenzo Testa, James C.A. Miller-Jones, Alberto Segreto (2019)
EWASS 2019 - European Week of Astronomy and Space Science, 24-28 June 2019
https://k-poster.kuoni-congress.info/ewass2019/poster/\5928c36b-4508-46b1-839f-d61b5252082a

- *Faint γ-ray sources at low-redshift: the radio galaxy IC 1531*
Tiziana Bassi, Giulia Migliori, Paola Grandi, Critian Vignali, Miguel Angel Pérez Torres, Ranieri D. Baldi, Eleonora Torresi, Aneta Siemiginowska, Carlo Stanghellini (2019)
EWASS 2019 - European Week of Astronomy and Space Science, 24-28 June 2019
https://k-poster.kuoni-congress.info/ewass2019/poster/383bf764-f63a-42b1-8d6a-549bbe233ae5

- *The 2016-2017 outburst of the black hole transient GRS 1716–249*
Tiziana Bassi, Melania Del Santo, Antonello D'Aì, Sara Motta, Julien Malzac, Alberto Segreto, James C.A. Miller-Jones, Pikky Atri, R.M. Plotkin, Tomaso Belloni, Teresa Mineo, Tasso Tzioumis (2018)
Exploring the Hot and Energetic Universe: The second scientific conference dedicated to the Athena X-ray observatory

https://www.astropa.inaf.it/wp-content/uploads/2018/09/PosterBassi-2.pdf

- *A Journey In The Radio Galaxy IC 1531: Through The Linear Scale, Across The Electromagnetic Spectrum*
  Bassi T.; Miglior G.; Grandi, P.; Vignali C. (2016)
  AGN12, Napoli, Italy, 26-29 September 2016, id.65
  doi:10.5281/zenodo.163827

A.3 Observing proposal accepted

- 2019 - Neil Gehrels Swift Observatory monitoring campaign of black hole transients
  PI: **Tiziana Bassi**
  CO-Is: M.Del Santo, A. D'Aì, A. Segreto, S. Motta, A. Marino, C. Pinto, E. Ambrosi, G. Cosumano

- 2019 - Swift Monitoring campaign of six bursters at sub-level accretion rate
  PI: Alessio Marino
  CO-Is: M.Del Santo, **T. Bassi**, A. D'Aì, A. Segreto, R. Amato, E. Ambrosi, V. La Parola, C. Pinto, A. Tutone, G. Cosumano

- 2019- Neil Gehrels Swift Observatory Monitoring of the galaxies containing ULXS: NGC 4559, NGC 5643 and NGC 925
  PI: Elena Ambrosi
  CO-Is: A. D'Aì, M. Del Santo, F. Pintore, C. Pinto, **T. Bassi**, A. Marino, G. Cosumano

- 2019 - Focusing onto γ-ray emission of Black Hole Transients in hard states
  PI Melania Del Santo
  Co-Is: S. Motta, J. Malzac, **T. Bassi**, J. Miller-Jones, A. D'Aì, C. Ferrigno, S. Migliari, J. Tomsick, P. Casella, T. Belloni, G. Sivakoff, L. Bouchet, T. Munoz-Darias

- 2018 - Swift MONITORING CAMPAIGN OF BLACK HOLE TRANSIENT
  PI: **Tiziana Bassi**
  Co-Is: Melania Del Santo, Antonino D'Aì, Alberto Segreto, Sara Motta, Alessio Marino

- 2018 - Monitoring campaign of six bursters at sub-level accretion rate
  PI Alessio Marino
  Co-Is: M. Del Santo, **T.Bassi**, A. D'Aì, A. Segreto, R. Amato, V. La Parola, G. Cusumano

- 2017 - Swift monitoring campaign of black hole transients
  PI: **Tiziana Bassi**
  Co-Is: Melania Del Santo, Antonino D'Aì, Alberto Segreto, Sara Motta

A.4 The Astronomer's Telegram

- February 2019 - Monitoring the transient MAXI J1348-630 with the Neil Gehrels Swift observatory (#12477)
  Bassi T.; Del Santo M.; D'Aì A.; Motta S.; Marino, A.; Segreto A.

- May 2017 - GRS 1716-249 is going back to the hard state (#10371)
  Bassi T.; Del Santo M.; Motta S.

- February 2017 - INTEGRAL and ATCA observations of the black hole transient GRS 1716-249 (#10069)
  Del Santo M.; Ducci L.; Miller-Jones J.; Ferrigno C.; D'Aì A.; **Bassi T.**; Migliari S.; Tomsick J.; Casella P.; Belloni T; Sivakoff G.

- February 2017 - Swift broad band observations of the Black Hole transient GRS 1716-249 (#10036)
  Del Santo M.; D'Aì A.; **Bassi T.**; Segreto A.; Belloni T.; Cusumano G.; La Parola V.

A.5 Publications in preparation

- *A new Swift/Suzaku look to the LMXB 4U 0614+091*
  A. Marino, T. Di Salvo, **T. Bassi**, M. Del Santo, A.F. Gambino, S. Mazzola, R. Iaria, L. Burderi

References

Abramowicz M. A., Lasota J. P., 1995, Comments on Astrophysics, 18, 141

Antonelli L. A., et al., 2003, Mem. Soc. Astron. Ita., 74, 304

Bahramian A., et al., 2018, Radio/X-ray correlation database for X-ray binaries, doi:10.5281/zenodo.1252036, https://doi.org/10.5281/zenodo.1252036

Ballet J., 1999, A&A Supp., 135, 371

Ballet J., Denis M., Gilfanov M., Sunyaev R., Harmon B. A., Zhang S. N., Paciesas W. S., Fishman G. J., 1993, IAU Circulars, 5874

Barthelmy S. D., et al., 2005, Space Science Reviews, 120, 143

Belloni T. M., 2010, States and Transitions in Black Hole Binaries. p. 53, doi:10.1007/978-3-540-76937-8_3

Belloni T. M., Motta S. E., 2016, in Bambi C., ed., Astrophysics and Space Science Library Vol. 440, Astrophysics of Black Holes: From Fundamental Aspects to Latest Developments. p. 61 (arXiv:1603.07872), doi:10.1007/978-3-662-52859-4_2

Belloni T., Psaltis D., van der Klis M., 2002, ApJ, 572, 392

Belloni T., Homan J., Casella P., van der Klis M., Nespoli E., Lewin W. H. G., Miller J. M., Méndez M., 2005, A&A, 440, 207

Belloni T., et al., 2006, MNRAS, 367, 1113

Belloni T. M., Motta S. E., Muñoz-Darias T., 2011, Bulletin of the Astronomical Society of India, 39, 409

Belmont R., Malzac J., Marcowith A., 2008, A&A, 491, 617

Blandford R. D., Königl A., 1979, ApJ, 232, 34

Bouchet L., del Santo M., Jourdain E., Roques J. P., Bazzano A., DeCesare G., 2009, ApJ, 693, 1871

Burrows D. N., et al., 2005, Space Science Reviews, 120, 165

Capalbi M., Perri M., Saija B., Tamburelli F., Angelini L., 2015,

Capitanio F., Belloni T., Del Santo M., Ubertini P., 2009, MNRAS, 398, 1194

Cardelli J. A., Clayton G. C., Mathis J. S., 1989, ApJ, 345, 245

Caroli E., Stephen J. B., Di Cocco G., Natalucci L., Spizzichino A., 1987, Space Science Reviews, 45, 349

Casella P., Belloni T., Homan J., Stella L., 2004, A&A, 426, 587

Casella P., et al., 2010, MNRAS, 404, L21

Chen W., Shrader C. R., Livio M., 1997, ApJ, 491, 312

Coppi P. S., 1992, MNRAS, 258, 657

Coppi P. S., 1999, in Poutanen J., Svensson R., eds, Astronomical Society of the Pacific Conference Series Vol. 161, High Energy Processes in Accreting Black Holes. p. 375 (arXiv:astro-ph/9903158)

Corbel S., Fender R. P., 2002, ApJL, 573, L35

Corbel S., Fender R. P., Tzioumis A. K., Nowak M., McIntyre V., Durouchoux P., Sood R., 2000, A&A, 359, 251

Corbel S., Nowak M. A., Fender R. P., Tzioumis A. K., Markoff S., 2003, A&A, 400, 1007

Corbel S., Coriat M., Brocksopp C., Tzioumis A. K., Fender R. P., Tomsick J. A., Buxton M. M., Bailyn C. D., 2013, MNRAS, 428, 2500

Coriat M., et al., 2011, MNRAS, 414, 677

Curran P. A., et al., 2014, MNRAS, 437, 3265

Del Santo M., Malzac J., Jourdain E., Belloni T., Ubertini P., 2008, MNRAS, 390, 227

Del Santo M., et al., 2009, MNRAS, 392, 992

Del Santo M., Malzac J., Belmont R., Bouchet L., De Cesare G., 2013, MNRAS, 430, 209

Del Santo M., et al., 2016, MNRAS, 456, 3585

Del Santo M., D'Ai' A., Bassi T., Segreto A., Belloni T., Cusumano G., La Parola V., 2017, The Astronomer's Telegram, 10036

Deller A. T., et al., 2011, Publ. Astr. Soc. Pac., 123, 275

Done C., Gierliński M., Kubota A., 2007, A&A Rev., 15, 1

Drappeau S., Malzac J., Belmont R., Gandhi P., Corbel S., 2015, MNRAS, 447, 3832

Drappeau S., et al., 2017, MNRAS, 466, 4272

Droulans R., Belmont R., Malzac J., Jourdain E., 2010, ApJ, 717, 1022

Dunn R. J. H., Fender R. P., Körding E. G., Belloni T., Cabanac C., 2010, MNRAS, 403, 61

Egron E., 2013, PhD thesis, Universitá di Catania

Esin A. A., McClintock J. E., Narayan R., 1997, ApJ, 489, 865

Espinasse M., Fender R., 2018, MNRAS, 473, 4122

Evans P. A., et al., 2007, A&A, 469, 379

Evans P. A., et al., 2009, MNRAS, 397, 1177

Fender R., Gallo E., 2014, Space Science Reviews, 183, 323

Fender R., et al., 1999, ApJL, 519, L165

Fender R. P., Hjellming R. M., Tilanus R. P. J., Pooley G. G., Deane J. R., Ogley R. N., Spencer R. E., 2001, MNRAS, 322, L23

Fender R. P., Belloni T. M., Gallo E., 2004, MNRAS, 355, 1105

Fender R. P., Stirling A. M., Spencer R. E., Brown I., Pooley G. G., Muxlow T. W. B., Miller-Jones J. C. A., 2006, MNRAS, 369, 603

Fender R. P., Homan J., Belloni T. M., 2009, MNRAS, 396, 1370

Ferreira J., Petrucci P. O., Henri G., Saugé L., Pelletier G., 2006, A&A, 447, 813

Ferrigno C., Bozzo E., Del Santo M., Capitanio F., 2012, A&A, 537, L7

Frank J., King A. R., Lasota J.-P., 1987, A&A, 178, 137

Frank J., King A., Raine D. J., 2002, Accretion Power in Astrophysics: Third Edition

Gallo E., 2010, Radio Emission and Jets from Microquasars. p. 85, doi:10.1007/978-3-540-76937-8_4

Gallo E., Fender R. P., Pooley G. G., 2003, MNRAS, 344, 60

Gandhi P., et al., 2011, ApJL, 740, L13

Ghisellini G., 2013, Radiative Processes in High Energy Astrophysics. Vol. 873, doi:10.1007/978-3-319-00612-3,

Ghisellini G., Guilbert P. W., Svensson R., 1988, ApJL, 334, L5

Giacconi R., Gursky H., Paolini F. R., Rossi B. B., 1962, , 9, 439

Gierliński M., Zdziarski A. A., Poutanen J., Coppi P. S., Ebisawa K., Johnson W. N., 1999, MNRAS, 309, 496

Gierliński M., Done C., Page K., 2008, MNRAS, 388, 753

Gierliński M., Done C., Page K., 2009, MNRAS, 392, 1106

Greisen E. W., 2003, in Heck A., ed., Astrophysics and Space Science Library Vol. 285, Information Handling in Astronomy - Historical Vistas. p. 109, doi:10.1007/0-306-48080-8_7

Haardt F., Maraschi L., Ghisellini G., 1994, ApJL, 432, L95

Harmon B. A., Fishman G. J., Paciesas W. S., Zhang S. N., 1993, IAU Circulars, 5900

Heinz S., Merloni A., 2004, MNRAS, 355, L1

Homan J., Belloni T., 2005, Ap&SS, 300, 107

Ichimaru S., 1977, ApJ, 214, 840

Ingram A., Done C., 2012, MNRAS, 419, 2369

Ingram A., Done C., Fragile P. C., 2009, MNRAS, 397, L101

Jones F. C., Ellison D. C., 1991, Space Science Reviews, 58, 259

Jourdain E., Roques J. P., Chauvin M., Clark D. J., 2012, ApJ, 761, 27

Kaiser C. R., Sunyaev R., Spruit H. C., 2000, A&A, 356, 975

Kalemci E., et al., 2014, MNRAS, 445, 1288

Kara E., et al., 2019, Nature, 565, 198

Körding E. G., Fender R. P., Migliari S., 2006, MNRAS, 369, 1451

Kubota A., Tanaka Y., Makishima K., Ueda Y., Dotani T., Inoue H., Yamaoka K., 1998, Pub. Astron. Soc. Japan, 50, 667

Lasota J.-P., 2001, , 45, 449

Laurent P., Titarchuk L., 1999, ApJ, 511, 289

Laurent P., Rodriguez J., Wilms J., Cadolle Bel M., Pottschmidt K., Grinberg V., 2011, Science, 332, 438

Lightman A. P., Zdziarski A. A., 1987, ApJ, 319, 643

Longair M. S., 2011, High Energy Astrophysics

Lund N., et al., 2003, A&A, 411, L231

Lyubarsky Y. E., 2010, MNRAS, 402, 353

Malyshev D., Zdziarski A. A., Chernyakova M., 2013, MNRAS, 434, 2380

Malzac J., 2012, in International Journal of Modern Physics Conference Series. pp 73–83, doi:10.1142/S2010194512004448

Malzac J., 2013, MNRAS, 429, L20

Malzac J., 2014, MNRAS, 443, 299

Malzac J., 2016, Astronomische Nachrichten, 337, 391

Malzac J., Belmont R., 2009, MNRAS, 392, 570

Marcel G., et al., 2018a, A&A, 615, A57

Marcel G., et al., 2018b, A&A, 617, A46

Marcel G., et al., 2019, A&A, 626, A115

Marscher A. P., 1980, ApJ, 235, 386

Mas-Hesse J. M., et al., 2003, A&A, 411, L261

Masetti N., Bianchini A., Bonibaker J., della Valle M., Vio R., 1996, A&A, 314, 123

Masumitsu T., et al., 2016, The Astronomer's Telegram, 9895

McConnell M., et al., 1994, ApJ, 424, 933

McConnell M. L., et al., 2002, ApJ, 572, 984

McMullin J. P., Waters B., Schiebel D., Young W., Golap K., 2007, in Shaw R. A., Hill F., Bell D. J., eds, Astronomical Society of the Pacific Conference Series Vol. 376, Astronomical Data Analysis Software and Systems XVI. p. 127

Merloni A., Heinz S., di Matteo T., 2003, MNRAS, 345, 1057

Meyer F., Meyer-Hofmeister E., 1981, A&A, 104, L10

Meyer-Hofmeister E., Meyer F., 2014, A&A, 562, A142

Meyer-Hofmeister E., Liu B. F., Meyer F., 2009, A&A, 508, 329

Miller-Jones J. C. A., Fender R. P., Nakar E., 2006, MNRAS, 367, 1432

Mirabel I. F., 1994, ApJS, 92, 369

Mirabel I. F., Dhawan V., Chaty S., Rodriguez L. F., Marti J., Robinson C. R., Swank J., Geballe T., 1998, A&A, 330, L9

Mitsuda K., et al., 1984, Pub. Astron. Soc. Japan, 36, 741

Motta S., Belloni T., Homan J., 2009, MNRAS, 400, 1603

Motta S. E., Casella P., Henze M., Muñoz-Darias T., Sanna A., Fender R., Belloni T., 2015, MNRAS, 447, 2059

Motta S. E., Casella P., Fender R. P., 2018, MNRAS, 478, 5159

Muñoz-Darias T., Motta S., Belloni T. M., 2011, MNRAS, 410, 679

Muñoz-Darias T., et al., 2013, MNRAS, 432, 1133

Narayan R., McClintock J. E., 2008, , 51, 733

Narayan R., Yi I., Mahadevan R., 1994, arXiv e-prints, pp astro–ph/9411060

Negoro H., et al., 2016, The Astronomer's Telegram, 9876

Niedźwiecki A., Zdziarski A. A., 2006, MNRAS, 365, 606

Oda H., Machida M., Nakamura K. E., Matsumoto R., 2010, ApJ, 712, 639

Oda H., Machida M., Nakamura K. E., Matsumoto R., Narayan R., 2012, Pub. Astron. Soc. Japan, 64, 15

Palazzi E., Pian E., Ross Team 2002, Mem. Soc. Astron. Ita., 73, 1193

Péault M., 2019, PhD thesis, âĂŹUniversité Toulouse III - Paul Sabatier (UT3 Paul Sabatier

Péault M., et al., 2019, MNRAS, 482, 2447

Poutanen J., Coppi P. S., 1998, Physica Scripta Volume T, 77, 57

Rahoui F., Lee J. C., Heinz S., Hines D. C., Pottschmidt K., Wilms J., Grinberg V., 2011, ApJ, 736, 63

Remillard R. A., McClintock J. E., 2006, ARA&A, 44, 49

Rodriguez J., et al., 2015, ApJ, 807, 17

Romano P., et al., 2006, A&A, 456, 917

Roming P. W. A., et al., 2005, Space Science Reviews, 120, 95

Ruffini R., 1974, in Astrophysics and Gravitation. pp 349–424

Russell D. M., Fender R. P., Hynes R. I., Brocksopp C., Homan J., Jonker P. G., Buxton M. M., 2006, MNRAS, 371, 1334

Russell D. M., et al., 2013a, MNRAS, 429, 815

Russell D. M., et al., 2013b, ApJL, 768, L35

Russell T. D., Soria R., Miller-Jones J. C. A., Curran P. A., Markoff S., Russell D. M., Sivakoff G. R., 2014, MNRAS, 439, 1390

Rybicki G. B., Lightman A. P., 1979, Radiative processes in astrophysics

Saikia P., Russell D. M., Bramich D. M., Miller-Jones J. C. A., Baglio M. C., Degenaar N., 2019, arXiv e-prints, p. arXiv:1910.01151

Sanbuichi K., Yamada T. T., Fukue J., 1993, Pub. Astron. Soc. Japan, 45, 443

Sault R. J., Teuben P. J., Wright M. C. H., 1995, in Shaw R. A., Payne H. E., Hayes J. J. E., eds, Astronomical Society of the Pacific Conference Series Vol. 77, Astronomical Data Analysis Software and Systems IV. p. 433 (arXiv:astro-ph/0612759)

Segreto A., Cusumano G., Ferrigno C., La Parola V., Mangano V., Mineo T., Romano P., 2010, A&A, 510, A47

Shakura N. I., Sunyaev R. A., 1973, A&A, 24, 337

Shimura T., Takahara F., 1995, ApJ, 445, 780

Sobolewska M. A., Papadakis I. E., Done C., Malzac J., 2011, MNRAS, 417, 280

Soleri P., et al., 2013, MNRAS, 429, 1244

Stetson P. B., 1994, in Blades J. C., Osmer S. J., eds, Calibrating Hubble Space Telescope. p. 89

Stetson P. B., Vandenberg D. A., Bolte M., Hesser J. E., Smith G. H., 1989, AJ, 97, 1360

Stirling A. M., Spencer R. E., de la Force C. J., Garrett M. A., Fender R. P., Ogley R. N., 2001, MNRAS, 327, 1273

Tao L., Tomsick J. A., Qu J., Zhang S., Zhang S., Bu Q., 2019, arXiv e-prints, p. arXiv:1910.11979

Tetarenko B. E., Sivakoff G. R., Heinke C. O., Gladstone J. C., 2016, ApJS, 222, 15

Tetarenko A. J., Casella P., Miller-Jones J. C. A., Sivakoff G. R., Tetarenko B. E., Maccarone T. J., Gand hi P., Eikenberry S., 2019, MNRAS, 484, 2987

Ubertini P., et al., 2003, A&A, 411, L131

Vedrenne G., et al., 2003, A&A, 411, L63

Verner D. A., Ferland G. J., Korista K. T., Yakovlev D. G., 1996, ApJ, 465, 487

Vitali F., et al., 2003, in Iye M., Moorwood A. F. M., eds, Proceedings of the SPIEVol. 4841, Instrument Design and Performance for Optical/Infrared Ground-based Telescopes. pp 627–638, doi:10.1117/12.459999

Wardziński G., Zdziarski A. A., Gierliński M., Grove J. E., Jahoda K., Johnson W. N., 2002, MNRAS, 337, 829

White N. E., Fabian A. C., Mushotzky R. F., 1984, A&A, 133, L9

Wilms J., Allen A., McCray R., 2000, ApJ, 542, 914

Winkler C., et al., 2003, A&A, 411, L1

Yuan F., 2001, MNRAS, 324, 119

Zdziarski A. A., 2000, in Martens P. C. H., Tsuruta S., Weber M. A., eds, IAU Symposium Vol. 195, Highly Energetic Physical Processes and Mechanisms for Emission from Astrophysical Plasmas. p. 153 (arXiv:astro-ph/0001078)

Zdziarski A. A., Gierliński M., 2004, Progress of Theoretical Physics Supplement, 155, 99

Zdziarski A. A., Johnson W. N., Magdziarz P., 1996, MNRAS, 283, 193

Zdziarski A. A., Stawarz Ł., Pjanka P., Sikora M., 2014a, MNRAS, 440, 2238

Zdziarski A. A., Pjanka P., Sikora M., Stawarz Ł., 2014b, MNRAS, 442, 3243

Zdziarski A. A., Malyshev D., Chernyakova M., Pooley G. G., 2017, MNRAS, 471, 3657

Życki P. T., Done C., Smith D. A., 1999, MNRAS, 309, 561

della Valle M., Mirabel I. F., Cordier B., Bonibaker J., Stirpe G., Rodriguez L. F., 1993, IAU Circulars, 5876

della Valle M., Mirabel I. F., Rodriguez L. F., 1994, A&A, 290, 803